

Scaling and Manipulation of Turbulent Structures in the Torsatron TJ-K

Dissertation
zur Erlangung des Doktorgrades
der Mathematisch-Naturwissenschaftlichen Fakultät
der Christian-Albrechts-Universität
zu Kiel

vorgelegt von
Mirko Ramisch

Kiel
März 2005

Referent/in:
Korreferent/in:
Tag der mündlichen Prüfung:
Zum Druck genehmigt: Kiel,

Der Dekan

Zusammenfassung

Turbulente Fluktuationen tauchen in vielen Bereichen der Natur auf. Insbesondere verursachen sie Transportprozesse in Gasen, Flüssigkeiten aber auch in Plasmen. In magnetisch eingeschlossenen Fusionsplasmen führt turbulenter Transport zu Verlusten von Teilchen und Energie aus dem Einschlussbereich heraus und verringert somit die Einschlussqualität. Dies stellt für den ökonomischen Betrieb eines Fusionskraftwerks ein wesentliches Problem dar. Kohärente Strukturen verdienen dabei eine besondere Aufmerksamkeit. Sie können Teilchen und Energie über große Distanzen quer zum Magnetfeld transportieren. Skalierungsuntersuchungen der raumzeitlichen Eigenschaften dieser Strukturen erlauben Vorhersagen über die Leistung zukünftiger Fusionsreaktoren. Die Skalierung von Korrelationslängen (L) und -zeiten (τ) mit charakteristischen Skalen hängt aber auch vom Antriebsmechanismus der Turbulenz ab. Zusätzlich können im Plasma Scherströmungen die Strukturen beeinflussen. Dieser Mechanismus ist ein Weg zur Unterdrückung von Turbulenz und dient zur Reduktion des turbulenten Transports. Vom System selbstkonsistent erzeugte Scherströmungen können spontane Übergänge in ein Regime mit verbessertem Einschluss (sogenannte L-H Übergänge) einleiten. Darüber hinaus besteht die Möglichkeit, diese Übergänge durch Induktion von elektrischen Feldern herbeizuführen.

In dieser Arbeit wurde zum ersten Mal das Skalierungsverhalten von L und τ direkt studiert. Dafür wurden Analysen an Daten durchgeführt, die simultan mit hoher zeitlicher Auflösung von einer 8×8 Matrix von Langmuirsonden aufgenommen wurden. Diese Analysen machten die raumzeitliche Entwicklung von propagierenden Dichtestrukturen in unterschiedlichen Gasen sichtbar. Für Gase mit kleinen Massenzahlen (H, D) erwiesen sich die Skalierungseigenschaften der charakteristischen Strukturen als konsistent mit der Vorhersage für die – im TJ-K erwiesenermaßen dominante – Driftwellenturbulenz. Schwerere Ionen dagegen tendieren zu einer globaleren Skalierung. Der Einfluss von Scherströmungen auf die Turbulenz wurde in Simulationen und im Experiment nachgewiesen. Um den Mechanismus der Transportreduktion durch Scherströmungen zu studieren wurden elektrische Felder induziert. Es wurde gezeigt, dass nicht, wie bisher angenommen, L sondern τ und die Kreuzphase zwischen Fluktuationen im poloidalen elektrischen Feld und der Dichte durch Scherströmungen verändert werden.

Abstract

Turbulent fluctuations occur in many different areas of nature. They are responsible for transport processes in gases, fluids and also in plasmas. In magnetically confined fusion plasmas, turbulent transport leads to a particle and heat loss out of the confinement region and, therefore, reduces the confinement quality. This is an essential problem for an economic operation of a fusion power plant. Of special interest are coherent structures in the fluctuations. They can carry particles and heat over large distances across the magnetic field. Scaling studies on the spatio-temporal properties of these structures allow for the prediction of the performance of future fusion devices. The scaling of correlation lengths (L) and times (τ) with characteristic scales, however, also depends on the mechanism driving the turbulence. In addition, sheared plasma flows can affect the structures. This mechanism serves as a paradigm for the suppression of turbulence and reduction of turbulent transport. Shear flows selfconsistently generated by the system can trigger spontaneous transitions (so-called L-H transitions) into an improved confinement regime. Furthermore, these transitions can be effected by the induction of electric fields.

In this work, for the first time the scaling properties of L and τ were studied in detail. Therefore, analyses were carried out on data with high temporal resolution, which were acquired simultaneously from an 8×8 Langmuir probe array. For different gases, the analyses reveal the spatio-temporal evolution of propagating density structures. For gases with small ion masses (H, D), the scaling properties of these characteristic structures turned out to be consistent with the prediction for drift-wave turbulence, which previously has been shown to be dominant in TJ-K. Heavier ions tend to a more global scaling. The influence of shear flows on turbulence was demonstrated in simulations and in the experiment. In order to study the mechanism of the transport reduction due to shear flows, electric fields were induced. It was shown that shear flows change the correlation time and the cross-phase between poloidal electric field and density fluctuations rather than the correlation length as it is usually assumed.

Contents

Contents	i
1 Introduction	1
2 Plasma confinement and transport	5
2.1 Toroidal magnetic confinement	5
2.1.1 Particle and fluid drifts	6
2.1.2 Basic magnetic confinement concepts	7
2.1.3 Radial transport in magnetised plasmas	9
2.2 Fluid models for plasma turbulence	10
2.2.1 Two-fluid model	11
2.2.2 The turbulence simulation code DALF3	11
2.3 Plasma turbulence	13
2.3.1 Neutral fluids	13
2.3.2 Characteristics of plasma turbulence	14
2.3.3 Interchange instability	15
2.3.4 Drift-wave instability	16
2.3.5 Turbulent transport	17
2.4 Energy confinement scaling	19
2.4.1 Global energy confinement	19
2.4.2 Microscopic scaling	20
2.5 Turbulence suppression	21
2.5.1 The L-H transition	21
2.5.2 Shear decorrelation mechanism	22
2.5.3 Zonal flows	23
2.5.4 The geodesic acoustic mode	24

Contents

2.5.5	External plasma biasing	25
3	The experiment TJ-K	27
3.1	Experimental setup	27
3.1.1	Specifications of the torsatron TJ-K	27
3.1.2	Plasma source	30
3.1.3	Plasma parameters	30
3.2	Diagnostics	30
3.2.1	Microwave interferometry	31
3.2.2	Langmuir probes	32
3.3	Equilibrium properties	37
3.3.1	Profiles of the main plasma parameters	37
3.3.2	Profiles of the poloidal flow velocity	38
4	Data analysis	39
4.1	Statistical data analysis	39
4.1.1	Probability density function	39
4.1.2	Correlation functions	40
4.2	Spectral analysis	41
4.2.1	Cross-power spectrum	41
4.2.2	Auto-power spectrum	42
4.2.3	The average cross-phase	43
4.2.4	Bispectral analysis	44
4.3	Detection of quasi-coherent structures	45
4.3.1	Correlation analyses	45
4.3.2	Evaluation of space-time characteristics	46
4.3.3	Comparison with the conditional average technique	48
5	Characteristics and scaling properties of turbulent structures	51
5.1	Experimental details	51
5.2	Space-time structure	53
5.3	Scaling of characteristic turbulence properties	54
5.3.1	Scaling of correlation lengths	54
5.3.2	Scaling of structure lifetimes	55

5.3.3	Scaling of the Turbulent diffusivity	56
5.4	Discussion and conclusions	58
6	Natural shear flows in TJ-K	63
6.1	Effect and drive of zonal flows	63
6.1.1	Analysis of zonal flows	64
6.1.2	Relation of zonal flows with Reynolds stress	66
6.2	Shear flows in TJ-K	70
6.2.1	Zonal flows in TJ-K	70
6.2.2	Natural shear layer	71
6.3	Summary and conclusions	73
7	Plasma biasing	75
7.1	Applied biasing schemes	75
7.1.1	The standard biasing scheme	75
7.1.2	Extended biasing probes	76
7.2	Ring biasing at the separatrix	78
7.2.1	Influence on the equilibrium profiles	78
7.2.2	Influence on the poloidal flow	79
7.2.3	Influence on the fluctuations	81
7.2.4	Influence on propagating density structures	83
7.2.5	Experiments with small ion masses	86
7.3	Ring biasing inside the separatrix	88
7.3.1	Comparison with separatrix biasing	88
7.3.2	Influence on turbulent structures	90
7.4	Summary	93
8	Summary and Conclusions	97
	References	101
	Acknowledgement	107

Contents

Introduction

High-temperature plasmas are intensively investigated with the objective to achieve a controlled nuclear fusion process for future energy production. The common confinement concept is based on toroidal magnetic field geometries, in which a magneto-hydrodynamic equilibrium can be established [1]. A major unresolved problem of nuclear fusion research is the description of the transport processes perpendicular to the magnetic field. Various mechanisms lead to a radial loss of particles and heat out of the plasma column. The major contribution to this loss is due to turbulent fluctuations in the plasma parameters. For a detailed understanding of turbulent transport, the knowledge of the mechanisms driving plasma turbulence is needed.

In neutral fluids, turbulence is observed as a non-laminar flow, which stochastically forms vortices in a broad range of spatial scales. This dynamics is described by the Navier-Stokes equation. When non-linearities become dominant, the flow field switches over from the laminar to the turbulent state [2]. However, the turbulent dynamics cannot be derived analytically from the Navier-Stokes equation. A breakthrough in the understanding of fluid turbulence has been reached in 1941 by Kolmogorov, who developed a theory based on postulated assumptions. This theory predicts an universal spectral energy transfer between vortices of different spatial scales [3, 2].

The applicability of fluid-turbulence theory to plasma turbulence is limited. Although a plasma can be described by hydrodynamic equations, the dynamics is more complicated than in neutral fluids, since additionally electro-magnetic forces are involved and turbulent fluctuations appear in plasma density, electrostatic potential, temperature and magnetic field. The latter can be neglected in low- β plasmas, where the plasma pressure is much smaller than the magnetic field pressure and the dynamics is governed by electrostatic turbulence. In this case, perturbations in density and electric field can cause local $E \times B$ advection of the plasma perpendicular to the magnetic field.

In this context, large-scale coherent structures in the fluctuations of the plasma potential and the density are of special interest [4, 5, 6]. Depending on the phase relation between these perturbations, they can cause radial $E \times B$ advection of particles over large distances. In terms of diffusive random walk processes, the spatial and the temporal properties of characteristic turbulent structures determine a diffusion coefficient, which describes

1. Introduction

the confinement quality. Under the constraint of dimensionally similar discharges [7, 8, 9, 10, 11], the scaling of this diffusion coefficient with characteristic spatial and temporal scales allows for the prediction of the confinement quality of future fusion reactors without having a detailed understanding of the driving mechanisms behind the transport. Depending on whether the transport is due to macroscopic or microscopic turbulence, the scaling is classified a Bohm- or gyro-Bohm-like, respectively. This scaling actually relies on the single scalings of correlation lengths and times of turbulent structures. However, most scaling studies are carried out on deduced diffusivities or global confinement times. In this work, the scaling of the original fluctuations has been studied for the first time. The detailed investigation is presented in chapter 5.

Plasma confinement can be strongly improved by transport barriers. First in the ASDEX tokamak, spontaneous transitions from a low-confinement (L-mode) into a high-confinement regime (H-mode) have been observed [12]. L-H transitions are accompanied by the formation of a transport barrier at the plasma edge [13]. $E \times B$ shear flows have been considered as a candidate for triggering the transport barrier. They are assumed to limit the radial correlation length of turbulent structures [14] and, thus, reduce radial turbulent transport. This shear decorrelation mechanism is investigated in chapters 6 and 7. One type of such flows are spontaneously excited, poloidally and toroidally symmetric, long lived $E \times B$ structures [15], called zonal flows (ZF). ZFs are supposed to be driven by turbulent Reynolds stress [16], which couples small-scale drift-waves non-linearly into the large-scale ZF [17]. Cross-bispectral analysis as a measure of coherent three-wave coupling has been proposed for the experimental investigation of the ZF drive. Expensive multipoint measurements in space and time are necessary for this analysis. Therefore, reduced bispectral quantities based on single-point measurements of fluctuations in the plasma potential or density have been suggested [17, 18]. The physics of the ZF drive, the effect of the ZF on turbulence and the applicability of the bispectral analysis techniques are investigated in Sec 6.1.

Besides spontaneous L-H transitions, improved confinement regimes can also be achieved by externally induced electric fields [19, 20, 21, 22, 23]. In the concept of plasma biasing, the plasma potential is locally modified by inserted electrode. In chapter 7, biasing is applied in order to study the mechanism of transport reduction due to shear flows.

The experiments reported here became possible due to the unique features of TJ-K plasmas. While in fusion plasmas the use of intrusive probe diagnostics, which feature a high spatial and temporal resolution, are restricted to the edge region, the low-temperature plasmas in the torsatron TJ-K are throughout accessible for these diagnostics. A high spatial and temporal resolution is required for resolving characteristics of plasma turbulence. In TJ-K, these characteristics can be measured at the edge as well as inside the confinement region. In particular, transitions in turbulence characteristics from regions with open field lines to regions with closed field lines can be studied

with high precision. The physical relevance for fusion research relies on the fact that the discharges in TJ-K are dimensionally similar to the edge region of fusion plasmas [24]. Hence, besides the issue of plasma production processes, TJ-K is predestinated for detailed edge turbulence studies. The experiments carried out in this work mainly focus on the confinement region with closed field lines, where the turbulence has turned out to be governed by drift-wave dynamics [25]. For the investigation of scaling properties of characteristic turbulent structures and the influence of $E \times B$ shear flows a special diagnostics consisting of an array of 8×8 probes has been built. Experimental results are compared to one from the drift-Alfvén-turbulence-simulation code DALF3 [26].

This work is organised as follows: Chapter 2 provides the basic details. The turbulence simulation code DALF3 is introduced. Fundamental instabilities are described. Transport is related to turbulent fluctuations and expected scalings are given. The mechanism of shear decorrelation and possible sources of flow shear are introduced. In chapter 3, the experiment TJ-K and the diagnostics used are introduced and a characterisation of the equilibrium is given. Chapter 4 outlines analysis tools, in particular, for the detection and evaluation of characteristic properties of quasi-coherent structures. The results are presented and discussed in the chapters 5 to 7 and summarised in chapter 8.

1. Introduction

Plasma confinement and transport

This chapter provides some basic principles for the magnetic confinement of fusion plasmas. Drifts – essential for the understanding of plasma dynamics – are introduced. Basic confinement concepts are outlined and the problem of radial particle transport is addressed. The major contribution to radial transport in fusion plasmas is due to turbulent fluctuations in the plasma parameters. For the understanding of turbulence, numerical simulations are necessary. A special fluid model, which has been used for comparisons with experimental investigations in TJ-K, is described. Two relevant mechanisms for driving turbulence in TJ-K are explained and the relation between turbulent transport and potential as well as density fluctuations is discussed. Ways for the characterisation and improvement of confinement quality are highlighted.

2.1 Toroidal magnetic confinement

Plasma is a partly or fully ionised gas consisting of charged particles, which can be bound to a magnetic field B due to the Lorentz force. Perpendicular to the magnetic field lines a charged particle of charge q , mass m and temperature T gyrates around its *guiding centre* with the *gyro frequency* (or *cyclotron frequency*) ω_c and an average *gyro radius* (or *Larmor radius*) ρ_L depending on the particle species:

$$\omega_c = \frac{qB}{m}, \quad \rho_L = \frac{\sqrt{2mk_B T}}{|q|B}. \quad (2.1)$$

An external force \mathbf{F} acting on the particle results in a drift motion of the guiding centre with a velocity of

$$\mathbf{V}_D = \frac{\mathbf{F} \times \mathbf{B}}{qB^2}. \quad (2.2)$$

This drift motion is oriented perpendicular to the external force and the magnetic field. Depending on the external force, the drift motion may be in opposite directions for negatively and positively charged particles. In this case

2. Plasma confinement and transport

the drift causes in fluids charge separation and thus electric currents. Drifts are fundamental for the understanding of plasma dynamics. They are crucial in the design and conception of fusion devices and magnetic field geometries. The most important drifts are introduced in the following.

2.1.1 Particle and fluid drifts

One distinguishes between drifts deduced from the picture of single particles and drifts showing up in the fluid description of the plasma. Some drifts can be found in both pictures. In this section, fluid drifts and particle drifts are distinguished by \mathbf{U} and \mathbf{V} , respectively.

Particles moving along magnetic field lines in an inhomogeneous, curved magnetic field experience drifts, which are due to centrifugal forces and gradients in the B-field. The *curvature drift* and the *gradient drift* are given by

$$\mathbf{V}_c = \frac{2W_{\parallel}}{qR_c^2} \frac{\mathbf{R}_c \times \mathbf{B}}{B^2} \quad \text{and} \quad \mathbf{V}_{\nabla B} = -\frac{W_{\perp}}{q} \frac{\nabla B \times \mathbf{B}}{B^3} \quad (2.3)$$

respectively. W_{\parallel} and W_{\perp} are the kinetic particle energy parallel and perpendicular to \mathbf{B} . \mathbf{R}_c is the curvature radius of the field line. Both drifts occur together. In current-free regions, the total drift is simply given by the sum of both. This drift depends on the charge of the particles and thus acts charge separating. Gradient and curvature drifts are not present in the fluid description.

In electric fields, the electrostatic force $\mathbf{F} = q\mathbf{E}$ causes the *E × B drift*

$$\mathbf{V}_{\mathbf{E} \times \mathbf{B}} = \frac{\mathbf{E} \times \mathbf{B}}{B^2}, \quad (2.4)$$

which points into the same direction for negatively and positively charged particles. Hence, no electric current is associated with this drift. Time varying electric fields are additionally accompanied by the *polarisation drift* $\mathbf{V}_p = m\dot{\mathbf{E}}/(qB^2)$ parallel to the electric field. The polarisation drift separates charge and causes a polarisation current $\mathbf{j}_p = (m_i + m_e)n\dot{\mathbf{E}}/B^2$, which – due to the mass dependence – is essentially governed by the ions. Both drifts – *E × B* and polarisation drift – also shows up in the fluid description.

All drifts introduced above can be obtained from the picture of single particles. Another drift only appears in the fluid picture of the plasma and is related to gradients in the plasma pressure $p = nT$: the *diamagnetic drift*

$$\mathbf{U}_{\text{dia}} = -\frac{\nabla p \times \mathbf{B}}{qnB^2}, \quad (2.5)$$

where n is the plasma density. As illustrated in Fig. 2.1, the contributions of particles with a density and/or temperature gradient produce a mean plasma

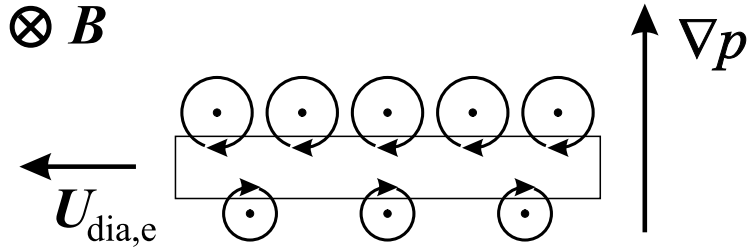


FIG. 2.1: Diamagnetic drift of electrons due to the pressure gradient. An average plasma flow remains if opposite particle motions do not cancel out in the case of an inhomogeneous plasma.

flow according to (2.5), when averaged within a volume element. In a homogeneous plasma, these contributions would cancel out. Contrary to the single particle drifts the diamagnetic drift has no influence on the guiding centres. Nevertheless, these inhomogeneities involve a net current $\mathbf{j}_{\text{dia}} = -\nabla p \times \mathbf{B}/B^2$, where $p = p_e + p_i$ is the total plasma pressure.

2.1.2 Basic magnetic confinement concepts

In order to confine a plasma in linear devices, the magnetic field strength is increased at the ends of the device. The magnetic moment $\mu = mv_{\perp}^2/(2B)$ – which is due to the current associated with the orbital motion of the particles with velocities v_{\perp} – is conserved, i.e., v_{\perp} increases at increasing B . Energy conservation leads to a transfer of energy from parallel motion to the perpendicular motion. Particles are finally reflected, if the magnetic field strength B_{end} at the ends of the device is as large as needed for transferring all energy of the parallel motion. This so called *mirror effect* can become important wherever particles move parallel to magnetic field lines into regions with increasing B .

In a *simple magnetised torus* (SMT) the magnetic field lines are closed in an axisymmetric toroidal geometry. As a consequence curvature and gradient drifts cause a vertical charge separation in the poloidal cross-section. A vertical electric field is generated. The associated $E \times B$ drift is always directed away from the torus centre and results in a continuous radial loss of electrons and ions. In this geometry, no stable magneto-hydrodynamic (MHD) equilibrium is achieved [1].

In fusion devices, the permanent radial loss of plasma due to the $E \times B$ drift is compensated by a *rotational transform*. An additional poloidal magnetic field component winds the field lines helically. Parallel electric currents then suppress the vertical charge separation. The rotational transform t is the poloidal angle displacement of one field line in units of 2π after one toroidal turn. It generally depends on the plasma radius. The field lines trace *magnetic flux surfaces*, on which the plasma pressure can be regarded as constant. A

2. Plasma confinement and transport

magnetic flux surface is also defined by a fixed and finite value of the magnetic flux through an arbitrary area bordered by the flux surface. The last closed flux surface is called *separatrix*, which encloses the confinement area. Outside the separatrix the field lines end on the vacuum vessel or on limiters.

Common fusion devices can be classified into two families: the *tokamak* and the *stellarator* family. Both types differ in the way the magnetic field is produced. In a tokamak, the toroidal component of the magnetic field is produced by planar external coils. A toroidal plasma current is induced by a primary coil in the centre of the torus. The plasma constitutes the secondary circuit of a transformer. The plasma current produces the poloidal component of the magnetic field. Toroidal and poloidal field components add to twisted magnetic field lines. Additional vertical field coils compensate respective field components in order to adjust closed flux surfaces to the dimensions of the vacuum vessel. The magnetic field geometry is axially symmetric. In Fig. 2.2 (left), an example of a fluxsurface in this geometry is shown. The operation is limited to pulses, since a DC plasma current requires a continuous increase of the magnetic flux through the primary coil. Details on tokamaks can be found in Ref. [27].

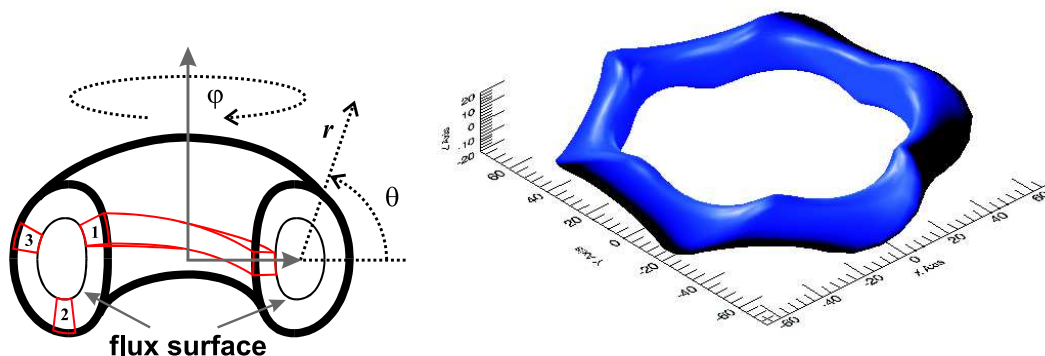


FIG. 2.2: Left: Torus coordinates (r, θ, φ) and flux surface in an axially symmetric tokamak geometry. For $\iota \approx 1/3$, a flux-tube around a field line indicates its trace. Right: Example of a magnetic flux surface of the $l = 1$, $m = 6$ torsatron TJ-K as calculated by means of the Gourdon fieldline-tracing code.

In stellarators, twisted magnetic field lines are produced solely by external field coils. One special configuration is called *torsatron*. Torsatrons possess helically wound field coils, which are operated with parallel currents. Vertical field components have to be compensated similarly to the tokamak. In general the geometry is rather complex and a simple axial symmetry is not given. The number of toroidal and poloidal field periods are m and l , respectively. An example of a magnetic flux surface of the $l = 1$, $m = 6$ torsatron TJ-K as calculated by means of the Gourdon fieldline-tracing code [28] is shown on the right-hand side of Fig. 2.2. The experiment TJ-K is introduced in more detail in chapter 3. In contrast to tokamaks a stellarator can be operated steadily

without a toroidal plasma current, which is an important feature for fusion power plants. Compared to tokamaks stellarators exhibit additional transport phenomena.

2.1.3 Radial transport in magnetised plasmas

In stationary plasmas, the loss of particles perpendicular to the magnetic field bases on continuous transport processes, which are due to background gradients in density, temperature and electrostatic potential as well as to collisions between electrons and ions. The *classical transport* is purely collisional. In the particle picture a diffusion coefficient $D = L^2/(2\tau)$ can be estimated using a random-walk model, where L is the radial step size and $1/\tau$ the step frequency. The displacement at a collision between an electron and an ion can be estimated by the electron Larmor radius (2.1) $L = \rho_{L,e}$. An estimate for the *collision frequency* $\nu_{e,i} = 1/\tau$ is given by

$$\nu_{e,i} = \left(\frac{e^2}{4\pi \epsilon_0} \right)^2 \frac{8\pi \ln \Lambda}{3\sqrt{3}m_e} \frac{n_e}{T_e^{3/2}}, \quad (2.6)$$

where $\ln \Lambda$ is the *Coulomb logarithm*, which can be approximated by [29]

$$\ln \Lambda = 23.4 - 1.15 \log n + 3.45 \log T_e \quad \text{for } T_e < 50 \text{ eV}, \quad (2.7)$$

$$\ln \Lambda = 25.3 - 1.15 \log n + 2.30 \log T_e \quad \text{for } T_e > 50 \text{ eV}. \quad (2.8)$$

Λ is a measure of the ratio of collisions with small and large scattering angles. The Pfirsch-Schlüter correction to the drift coefficient accounts for gradient and curvature drifts in toroidal magnetic field geometries. Particle trajectories follow *drift surfaces* rather than flux surfaces. These drift surfaces have a displacement with respect to the flux surfaces, which yields an additional diffusion term $D_{\text{PS}} = 2q_s^2 D_{\text{classic}}$, where $q_s = 1/t$ is the so called *safety factor*.

Neoclassical transport generally involves transport processes due to deviations of particle trajectories – in particular of trapped particles – from the flux surfaces. The magnetic field strength in a toroidal geometry is typically larger on the inner side of the torus (high-field side) than on the outer side (low-field side). Particles enter on their trajectory parallel to twisted field lines regions with increasing B , where they can be reflected according to the mirror effect. Hence, these trapped particles are prevented from performing a full poloidal turn. Their trajectory, as projected onto the poloidal cross-section, has the form of a banana with a certain width. At low collision frequencies the particles can pass the full banana orbit, which then is the step size in collisions. The banana transport in a tokamak is typically 50 times larger than the classical transport.

Especially in stellarators, the neoclassical transport is of great importance. Compared to the banana transport in tokamaks, the radial transport in stellarators is enhanced by particles, which are helically trapped within magnetic

2. Plasma confinement and transport

ripples of the specific B-field. These particles get lost directly via vertical drifts, if they are not de-trapped by collisions. As a result the so called $1/\nu$ transport increases at decreasing collision frequencies up to a maximum. Towards smaller frequencies, the transport decreases again, because the emerging gap in the Maxwell distribution due to particle losses cannot sufficiently be refilled by collisions. Transport due to helically trapped particles arises from drifts and is not necessarily ambipolar. Self-generated radial electric fields cause poloidal $E \times B$ drifts, which can also reduce $1/\nu$ transport.

A more detailed introduction as well as investigations of neoclassical transport and electric field measurements in TJ-K can be found in Ref. [30]. Although neoclassical transport results in larger transport coefficients, these models do not describe the level of transport observed experimentally. There is overwhelming evidence that fluctuations in the plasma parameters are responsible for most of the transport. The corresponding transport is called *turbulent transport* or *anomalous transport*. Perturbations in the electric field can cause radial $E \times B$ flows and the transport based on this mechanism is called electrostatic, i.e., the contribution of perturbations in the magnetic field is negligible. A detailed description will separately be given in Sec. 2.3.

2.2 Fluid models for plasma turbulence

A plasma represents an N -body problem, where N is too large to be suitable for numerical computations. In many cases it is sufficient to reduce the problem to a macroscopic description, where statistical averages over small volumes of the plasma give representative results for the density, temperature and the mean velocity of the particles. One arrives at a macroscopic fluid-like description of a plasma by adding electro-magnetic forces to hydrodynamic equations, by deriving the fluid equations as a set of conservation laws or by taking hierarchical moments of the kinetic equations. Electrons and ions are treated as separate fluids, which are coupled through electric fields and collisions. This model is capable of describing the dynamic evolution of the plasma self-consistently and covers turbulence driving instabilities as, e.g., drift-waves and MHD-interchange instabilities (see Sec. 2.3). Kinetic effects are neglected. Effects arising from interactions of waves with the distribution function as Landau damping or effects due to a deformation of the distribution function by inhomogeneous magnetic fields are missing. Effects on scales comparable to the gyro-motion are not resolved. This leads to correlations, if the gyro-radius becomes comparable to the dimensions of the volume element regarded (finite-Larmor-radius effects).

2.2.1 Two-fluid model

In the two-fluid model, electrons and a single ion species are involved. Each particle species is described by a set of fluid equations. The first equation is the *continuity equation*

$$\frac{\partial}{\partial t}n + \nabla \cdot (n\mathbf{U}) = 0, \quad (2.9)$$

where $\mathbf{U} = \langle \mathbf{V} \rangle$ is the bulk velocity of particles with velocities \mathbf{V} . Collisions, which create or annihilate particles by ionisation or recombination, are neglected. The second equation is the *momentum equation* (or simply equation of motion)

$$mn \left(\frac{\partial}{\partial t} + \mathbf{U} \cdot \nabla \right) \mathbf{U} = -\nabla p + qn \left(\mathbf{E} + \frac{1}{c} (\mathbf{U} \times \mathbf{B}) \right) + \mathbf{R}. \quad (2.10)$$

The operator within the brackets on the left-hand side is the *convective derivative* and represents temporal changes of the velocity field within a co-moving plasma volume. It is balanced by pressure gradients, electro-magnetic forces and collisional friction. The pressure gradient originates from the diagonal elements of the *pressure tensor* $\mathbf{P} = mn \langle \delta \mathbf{V} \delta \mathbf{V}^T \rangle$ with $\delta \mathbf{V} = \mathbf{V} - \mathbf{U}$. For isotropic velocity distribution functions non-diagonal elements vanish and for a Maxwellian distribution function, as in the case of a thermalised plasma, the term $-\nabla \cdot \mathbf{P}$ reduces to $-\nabla p$ with $nm \langle \delta V^2 \rangle / 2 = 3nT/2$ and $p = nT$. Viscous damping terms can enter the equation in consequence of deviations from the Maxwellian distribution function. \mathbf{R} describes the change of momentum due to collisions between particles of different species. Collisions between particles of the same species do not change the total momentum or energy. The *energy equation*, as the third equation, is omitted here. A detailed derivation of the equations as moments of the kinetic equation can be found in Ref. [31].

The two-fluid model for electrons and singly ionised ions describes the evolution of the ten plasma-dynamical variables n_α , \mathbf{U}_α and T_α ($\alpha = e, i$). The full set of Maxwell equations completes the model. Further assumptions as on magnetic fields, space-time scales, ion inertia, quasi-neutrality, etc., can further reduce the complexity of the model.

2.2.2 The turbulence simulation code DALF3

The drift-Alfvén-turbulence-simulation code *DALF3* [26] solves a two-fluid model in three-dimensional flux-tube geometry. DALF3 has already been used for comparative studies with experimental measurements in TJ-K [32, 24, 33, 34]. In this model, particles, ionisation and recombination are not included and quasi-neutrality is assumed ($\nabla \cdot \mathbf{J} = 0$). Furthermore, ions are regarded as cold ($T_i \ll T_e$). The dynamics splits up in parts perpendicular and parallel to the magnetic field. Only drifts are responsible for flows perpendicular to the

2. Plasma confinement and transport

B -field. Perpendicular electric currents are dominated by the ion-polarisation current and the electron-diamagnetic current (see Sec. 2.1.1). Due to ion-inertia parallel to the magnetic field, the ion response to pressure gradients is neglected compared to the electron response. Thus, the parallel electric current – deduced from the generalised Ohm’s law – is governed by the electrons.

The model equations, which are solved for fluctuations in the electrostatic potential $\tilde{\phi}$, electron density \tilde{n}_e , parallel current \tilde{J}_\parallel and parallel ion flow \tilde{u}_\parallel read:

$$\frac{n_e M_i c^2}{B^2} \frac{d}{dt} \nabla_\perp^2 \tilde{\phi} = \nabla_\parallel \tilde{J}_\parallel - \mathcal{K}(\tilde{p}_e), \quad (2.11)$$

$$\frac{n_e e}{c} \frac{\partial}{\partial t} \tilde{A}_\parallel + \frac{m_e}{e} \frac{d}{dt} \tilde{J}_\parallel = \nabla_\parallel (p_e + \tilde{p}_e) - n_e e \nabla_\parallel \tilde{\phi} - 0.51 \frac{m_e}{e} \nu_e \tilde{J}_\parallel, \quad (2.12)$$

$$\frac{d}{dt} (\tilde{p}_e + p_e) = \frac{T_e}{e} \nabla_\parallel \tilde{J}_\parallel - p_e \nabla_\parallel \tilde{u}_\parallel - \frac{T_e}{e} \mathcal{K}(\tilde{p}_e) + p_e \mathcal{K}(\tilde{\phi}), \quad (2.13)$$

$$n_i M_i \frac{d}{dt} \tilde{u}_\parallel = -\nabla_\parallel (p_e + \tilde{p}_e). \quad (2.14)$$

The parallel component of the magnetic potential \tilde{A}_\parallel is connected to \tilde{J}_\parallel through Ampere’s law. This set of equations reflects the conservation of charge (2.11), parallel electron (2.12) and ion momentum (2.14) and energy (2.13), where

$$\frac{d}{dt} = \frac{\partial}{\partial t} + \frac{c}{B^2} \mathbf{B} \times \nabla \phi \cdot \nabla, \quad \mathcal{K} \equiv -\nabla \cdot \frac{c}{B^2} \mathbf{B} \times \nabla \quad (2.15)$$

include the advection by the $E \times B$ velocity as a first order approximation to the hydrodynamic derivative and effects due to magnetic curvature, respectively. The background electron temperature T_e and density n_e as well as their gradients enter as constants. The first term in Eq. (2.12) describes magnetic induction, the last term electric resistivity due to collisions. ν_e is the Braginskii electron collision frequency [35] (see Eq. (2.6)). Perpendicular and parallel dynamics are coupled through parallel currents in Eq. (2.11), giving rise for drift-waves. Magnetic induction and electric resistivity are responsible for a non-adiabatic electron response to a density perturbation. I.e., density and potential perturbations exhibit a phase-shift, which makes drift-waves unstable in order to cause transport. In toroidal geometry, magnetic curvature enters Eq. (2.11) through the divergency of the electron-diamagnetic current, which disturbs the balance between the divergencies of the ion-polarisation current and the parallel current governed by the electrons.

The temporal evolution of the variables $\tilde{\phi}$, \tilde{n}_e , \tilde{J}_\parallel and \tilde{u}_\parallel is simulated on a three-dimensional grid ($x \times y \times s$) in field aligned coordinates of a flux-tube around a closed field line in TJ-K equivalent tokamak geometry [33], with globally consistent boundary conditions [36] using a ‘shifted metric’ technique to avoid deformation of coordinate cells due to magnetic shear [37]. The coordinates x and y describe the drift plane perpendicular to the magnetic field. x count into in the opposite direction of the pressure gradient and y parallel

to isobars. Hence, the (x, y) plane is similar to the poloidal (r, θ) plane (see Fig. 2.2). The coordinate s projects the position along \mathbf{B} onto the poloidal location θ . It describes the position along the closed field line starting on the high-field side.

In normalised units, the turbulence resulting from the equations is controlled by the dimensionless parameters

$$\mu^* = \frac{m_e}{M_i} \left(\frac{q_s R_0}{L_\perp} \right)^2 \quad \beta^* = \frac{4\pi n_e T_e}{B^2} \left(\frac{q_s R_0}{L_\perp} \right)^2 \quad \nu^* = 0.51 \nu_e \frac{L_\perp}{c_s}, \quad (2.16)$$

where R_0 is the toroidal major radius, q_s the safety factor, $L_\perp = |\nabla \log n_e|^{-1}$ the perpendicular gradient scale length and c_s is the *sound speed* given by $c_s^2 = T_e/M_i$. Spatial scales are given in terms of the *drift-scale* $\rho_s = c_s/\omega_{ci} = \sqrt{M_i T_e}/(eB)$, where ω_{ci} is the ion cyclotron frequency (2.1). The parameters are the mass ratio μ^* normalised to geometrical constants, the normalised plasma beta β^* and the normalised collisionality ν^* . β^* and ν^* control the contribution of interchange and drift-wave instabilities respectively [33]. Detailed parameter studies have shown [33] that the operational regime of TJ-K is in terms of these parameters similar to that in the plasma edge of fusion devices. Comparative investigations with experimental measurements are sensible as long as the drift-ordering constraint $\rho_s \ll L_\perp$ holds.

2.3 Plasma turbulence

Turbulence can be observed in various fields in nature. A familiar example is a barrier in a fluid flow, which creates vortices behind the barrier. These vortices are a fundamental characteristic of turbulence. Turbulent flows possess interesting features for engineering. One example is the fast-mixing property for mixtures of gases in fuel chambers. In fusion plasmas, turbulence affects the confinement quality. Much efforts have been made to understand the driving mechanisms for plasma turbulence in order to reduce or even suppress it and work is still in progress. This section gives a characterisation of turbulence in neutral fluids and plasmas. The relation between turbulent fluctuations and radial transport is discussed.

2.3.1 Neutral fluids

The basic equation describing turbulence in incompressible ($\nabla \cdot \mathbf{U} = 0$), neutral fluids is the *Navier-Stokes equation*

$$\left(\frac{\partial}{\partial t} + \mathbf{U} \cdot \nabla \right) \mathbf{U} = -\nabla p / \rho + \nu \nabla^2 \mathbf{U} + \mathbf{F}, \quad (2.17)$$

2. Plasma confinement and transport

consisting of the convective derivative of the velocity field \mathbf{U} on the left-hand side and the pressure and friction forces per unit volume on the right-hand side. ρ is the mass density and ν the kinematic viscosity. At given geometry, the only parameter, which controls the dynamics, is the *Reynolds number* $Re = LU/\nu$, L and U being a characteristic scale and velocity of the flow, respectively.

The Reynolds number can be regarded as the ratio of the non-linear term to the viscous damping term. When the non-linear term is dominant at high values of Re – characteristic for each physical system and its boundary conditions – the flow changes from the laminar to the turbulent state. The flow field becomes stochastic and forms vortices in a broad range of spatial scales. The randomness necessitates a statistical description of the fluctuations. Fluctuations are usually characterised by their *probability density function* (PDF) and its moments (see Sec. 4.1.1). For stationary turbulence, these statistical properties stay constant.

The fluctuations at any position are a consequence of non-linear interactions between vortices of different spatial scales. Energy is non-linearly transferred between these scales. The dissipative nature of turbulent flows demands for an energy source, which must balance the dissipation in order to maintain turbulence. Based on the theory presented by Kolmogorov in 1941 (*K41-theory*) [3] for homogeneous, isotropic, three-dimensional fluid turbulence, the spectral energy E – injected at large scales (small wavenumbers k) and dissipated at small scales (large wavenumbers) – turned out to be transferred from large to small scales down a cascade according to a power law $E(k) \sim k^{-5/3}$. In the range of the cascade, the so called *inertial range*, the turbulence has been assumed to be self-similar. A detailed discussion of the K41-theory can be found in Ref. [2]. For two-dimensional turbulence, two inertial ranges with different power laws have been predicted [38]. The energy is injected at intermediate scales. Energy is transferred up an inverse cascade to the largest scales available in the system according to $E(k) \sim k^{-5/3}$. In the second inertial range an enstrophy cascade down to small scales shows up as $E(k) \sim k^{-3}$ in the energy spectrum.

2.3.2 Characteristics of plasma turbulence

Plasma turbulence is similar to but considerably more complicated than neutral-fluid turbulence, since in addition to viscous forces, electrostatic and electromagnetic forces are involved. Fluctuations appear in the density (\tilde{n}), in the electrostatic potential ($\tilde{\phi}$), in the temperature (\tilde{T}) and in the magnetic field strength (\tilde{B}). One question concerns the applicability of the K41-theory to plasma turbulence. Deviations from the Kolmogorov scaling would not be surprising, since the assumptions made are obviously violated: (i) The energy source is not restricted to large scales. The background gradients act as energy source for the plasma dynamics on all scales. (ii) In magnetised plasmas,

2. Plasma confinement and transport

are not fully neutralised by electrons coming from low-density regions. A surplus of positive charge develops at the interface. Half a period away, where electrons drift from a high- to a low-density region, a surplus of negative charge develops. This leads to electric fields and corresponding $E \times B$ drifts. The configuration shown in Fig. 2.3 is called bad curvature. In this configuration, the curvature radius \mathbf{R}_c of the magnetic field line is anti-parallel to the pressure gradient. The resulting $E \times B$ drifts amplify the perturbation. The interchange mode becomes unstable. In the good curvature case, \mathbf{R}_c is parallel to the pressure gradient. The curvature drifts for electrons and ions as shown in Fig. 2.3 change the direction. Consequently, electric fields and $E \times B$ drifts change the direction, too. The interchange mode is damped.

In a toroidal geometry, the good curvature region is found on the high-field side and the bad curvature region on the low-field side. Due to the stabilisation on the high-field and the destabilisation on the low-field side, the fluctuation amplitudes differ for both regions. This is one characteristic of interchange modes in toroidal geometry, also called *ballooning*. Another signature is a phase-shift of $\pi/2$ between potential and density perturbation as indicated in Fig. 2.3. The perturbations are homogeneous parallel to the magnetic field ($k_{\parallel} = 0$). Thus, unlike the drift-wave instability, the interchange instability is a purely two-dimensional phenomenon in the perpendicular plane. The hydrodynamic analogy is the Rayleigh-Taylor instability.

2.3.4 Drift-wave instability

In Fig. 2.4, the development of a *drift-wave instability* is illustrated. Essential

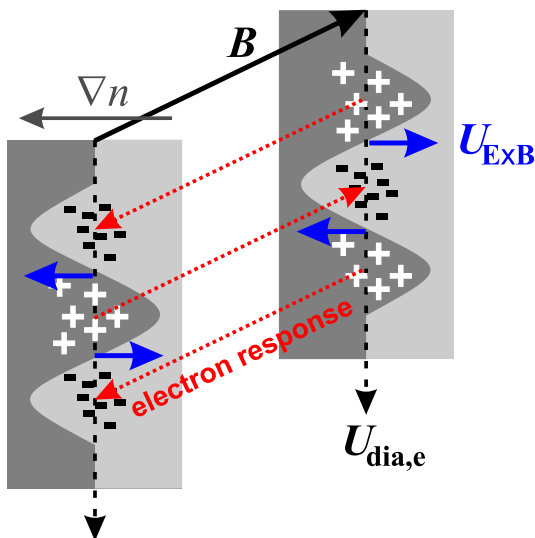


FIG. 2.4: Mechanism for the development of drift-wave instabilities. Electrons respond along the magnetic field (red arrows) to a perturbation in the density, which has a finite wavenumber $k_{\parallel} \neq 0$. For an adiabatic response, the corresponding potential perturbation is in phase with the density perturbation. $E \times B$ drifts (blue arrows) lead to a propagation of the density perturbation into to the electron-diamagnetic-drift direction.

for drift-waves is a background pressure gradient – or, for simplification, a density gradient at constant temperature – and a density perturbation, which

has a finite wavelength parallel to the magnetic field $\lambda_{\parallel} \gg \lambda_{\perp}$. Thus, drift-waves have a three-dimensional structure. The parallel dynamics is governed by the electrons, which respond to the three-dimensional perturbation by moving down the parallel density gradient. Thus, regions with a positive density perturbation are accompanied by a positive potential perturbation. For an adiabatic, i.e., instantaneous response of the electrons, density and potential perturbations are in phase ($\gamma = 0$). The electric field perturbations cause $E \times B$ drifts as shown in Fig. 2.4. Due to the drift, the density perturbation is increased on the one flank and decreased on the other leading to a propagation of the perturbation with the electron-diamagnetic drift velocity (2.5). The drift-mode is stable, if density and potential perturbations are in phase. A phase difference develops, if the parallel electron response is non-adiabatic. This can happen, if the electrons motion is hindered by resistivity or magnetic induction. For a negative phase difference ($\gamma < 0$), the drift-mode becomes unstable and grows. In the case of a positive phase difference ($\gamma > 0$), the drift-mode is stabilised. Characteristic for drift-waves is a phase-shift close to zero ($\gamma \approx 0$) [39] and a scaling of the perpendicular size with the *drift-scale*

$$\rho_s = \sqrt{T_e M_i / e B}, \quad (2.18)$$

which is the ion gyro-radius at electron temperature. It has been confirmed in Refs. [25] that drift-waves are the dominant mechanism for driving the turbulence in TJ-K.

2.3.5 Turbulent transport

In Sec. 2.1.3 the neoclassical transport approach for the description of radial particle losses has been outlined. This approach is not sufficient to describe the particle flux observed in fusion plasmas. However, *turbulent* (or *anomalous*) *transport* due to electrostatic turbulence is capable of accounting for the observed large transport levels [40]. Turbulent transport is produced by $E \times B$ drifts arising from fluctuations in the electric field. It is defined by

$$\Gamma(t) = \langle \tilde{u}_r \tilde{n} \rangle_F = \frac{1}{B} \langle \tilde{E}_{\theta} \tilde{n} \rangle_F, \quad (2.19)$$

where \tilde{u}_r are fluctuations of the radial component of the $E \times B$ drift expressed in terms of poloidal electric field fluctuations \tilde{E}_{θ} on the right-hand side. The subscript F denotes averaging over a flux surface (see Fig. 2.2). Eq. (2.19) describes the net particle flux through a flux surface as a function of time.

Fig. 2.5 (left) demonstrates, how turbulent eddies in a plasma are associated with perturbations $\tilde{\phi}$ in the electrostatic potential, which lead to perturbations of the electric field. Corresponding $E \times B$ drifts cause a vortex-like advection of the background plasma. Radial net transport is obtained only if a perturbation of the density is present. Additionally, the phase between density and potential

2. Plasma confinement and transport

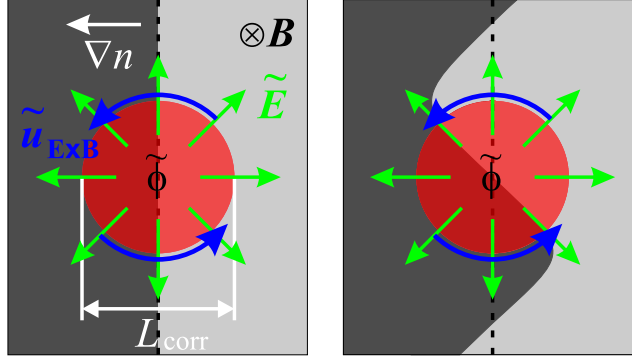


FIG. 2.5: A turbulent eddy of size L_{corr} associated with a potential perturbation $\tilde{\phi}$ (left). Net particle transport is a consequence of a phase difference between density and potential fluctuations (right). The dark area indicates the high-density region, the bright area the low-density region.

fluctuations plays an important role. As indicated on the right-hand side of Fig. 2.5, radial net transport is a consequence of density and potential perturbations being out of phase. Without a phase difference (or a density perturbation), particles would be carried inwards as much as outwards. The radial net transport would be zero.

The local mean transport is provided by regarding fluctuations \tilde{E}_θ , \tilde{n} at a single point in space and replacing the flux surface average in Eq. (2.19) by a temporal average. In the following, a relation between the local mean transport and the cross-phase is derived. To this end, the fluctuating quantities $\tilde{f}(t)$ are represented by the Fourier transforms $\hat{f}(\omega)$:

$$\tilde{f}(t) = \frac{1}{\sqrt{2\pi}} \int d\omega \hat{f}(\omega) \exp(i\omega t), \quad (2.20)$$

where the integration goes from $-\infty$ to ∞ . For simplicity, B is set to 1 and the subscript θ in E_θ is omitted. The derivation reads:

$$\begin{aligned} \Gamma &= \left\langle \tilde{E}(t) \tilde{n}(t) \right\rangle_t \\ &= \int d\omega \hat{E}^*(\omega) \int d\omega' \hat{n}(\omega') \frac{1}{2\pi} \int dt \exp(i(\omega' - \omega)t) \\ &= \int d\omega \hat{E}^*(\omega) \hat{n}(\omega) = \int d\omega \text{Re} \left[\hat{E}^*(\omega) \hat{n}(\omega) \right] \\ &= \int d\omega |\hat{E}^*(\omega)| |\hat{n}(\omega)| \cos(\varphi(\omega)), \end{aligned} \quad (2.21)$$

where $\varphi(\omega) = \varphi_n(\omega) - \varphi_E(\omega)$ is the cross-phase between density and electric-field fluctuations at frequency ω . The asterisk denotes the complex conjugate. In the last step, the symmetry property $\hat{f}^*(\omega) = \hat{f}(-\omega)$ is used. Therefore, the imaginary part vanishes under the integral. For $\varphi(\omega) = \pi/2$, no transport

is obtained at frequency ω . Cross-phases $\varphi(\omega) > \pi/2$ and $\varphi(\omega) < \pi/2$ indicate inward and outward transport, which is maximal for $\varphi(\omega) = 0$ and $\varphi(\omega) = \pi$, respectively. A similar result can be obtained for the relation between density and potential fluctuations by substituting $\widehat{E}(\omega) = ik(\omega)\widehat{\phi}(\omega)$. Then the cosine in Eq. (2.21) turns to the sine of the cross-phase $\gamma(\omega)$ between density and potential fluctuations with $\gamma(\omega) = \varphi(\omega) - \pi/2$.

2.4 Energy confinement scaling

Plasma turbulence is not sufficiently understood in order to make predictions for future fusion reactors via the modelling of turbulent transport. Instead, the global energy confinement time τ_E or heat diffusivity χ of discharges similar to that in future fusion reactors is used in most studies in order to characterise the confinement quality and scale it to ignition. The scalings of these quantities are, however, a consequence of microscopic scalings under the assumption of simple mixing-lengths estimates. In this work, the scaling properties of the microscopic quantities are investigated directly.

2.4.1 Global energy confinement

In order to estimate the transport level, the global energy confinement time τ_E is commonly used. For a stationary plasma, τ_E is given by the ratio of global energy content and heating power input. The heat diffusivity χ is related to τ_E according to [41]

$$\tau_E \approx \frac{3a^2}{4\chi}, \quad (2.22)$$

where the factor $3/4$ is for identical profile shapes and a is the minor plasma radius.

Empirical scaling expressions for τ_E as a function of global plasma parameters can be obtained by regression analysis of multi-machine confinement databases. One example is the *international stellarator scaling* (ISS95) [42]

$$\tau_E^{ISS95} = 0.079 a^{2.21} R_0^{0.65} P_{tot}^{-0.59} n_l^{0.51} B_t^{0.83} t_{2/3}^{0.4}. \quad (2.23)$$

The ISS95 expression characterises the confinement time (in seconds) of stellarator and low-confinement (L-mode) tokamak discharges against minor a and major plasma radius R_0 (in metres), total absorbed heating power P_{tot} (megawatts), line averaged density n_l (10^{19} m^{-3}), toroidal magnetic field strength B_t (tesla) and the rotational transform $t_{2/3}$ at a normalised plasma radius of $\rho = 2/3$. Such scaling expressions can be used to predict the performance of future fusion devices and the requirements for ignition.

2. Plasma confinement and transport

The magnetic field attract a special interest concerning costs. Dimensionally similar discharges [7, 8] provide the possibility to study the dependency of τ_E on B and geometrical parameters only. Therefore, the heat diffusivity χ is written in dimensionally correct form as a function of a normalised gyro-radius $\rho_* = \rho_s/a$ and other dimensionless parameters, such as the collisionality and the plasma beta (2.16), rotational transform, aspect ratio, gradient scale length, etc.,

$$\chi = D_B \rho_*^{\alpha_\rho} F(\nu_*, \beta_*, t, \epsilon, L_\perp/a, \dots), \quad (2.24)$$

where $D_B = \rho_s c_s$ is the Bohm diffusion coefficient, expressed in terms of the drift-scale ρ_s and the sound speed c_s . Discharges with fixed values for all dimensionless parameters except for ρ_* are called dimensionally similar. The exponent α_ρ obtained from a variation of ρ_* determines the B and size scaling, since the remaining parameters, e.g., n and T , can be eliminated due to constraints induced by the constance of $\nu_* \sim an/T^2$ and $\beta_* \sim nT/B^2$. For reactor relevant values of the dimensionless parameters, these discharges can be scaled to ignition if α_ρ is known.

The dependence of τ_E – related to the diffusivity according to (2.22) – on B and geometrical parameters is characteristic for the underlying transport mechanism. Two essential scaling types are distinguished [9]. For $\alpha_\rho = 0$, the scaling is Bohm-like and the fluctuations have a global character. For $\alpha_\rho = 1$ or a gyro-Bohm-like scaling, the transport is attributed to microscopic turbulence. The scaling of confinement times and diffusivities has been investigated with respect to the prediction of ITER performance [9, 10, 43]. These studies base on the scaling of inferred transport coefficients and confinement times. In dimensionally similar discharges, ρ_* has been varied through the magnetic field.

2.4.2 Microscopic scaling

In chapter 5, the transport level is investigated directly on the scaling properties of characteristic turbulent structures. For drift-wave turbulence as present in TJ-K, theory predicts a gyro-Bohm-like scaling of the diffusivity. From a random walk model a rough estimate for the turbulent diffusivity

$$D \approx L_c^2/\tau_c \quad (2.25)$$

is constructed out of typical length and time scales under the assumption that density and poloidal electric field fluctuations are in phase. If the typical length scales linearly with ρ_s and using for the typical time the linear growth rate of drift-waves $1/\tau_c \sim c_s/R_0$ [44] ($R_0 \sim a$), the gyro-Bohm-like nature of drift-wave turbulence is reproduced, namely $D = D_B \rho_s/a$. Thus, the dimensionless parameter $D^* = D/D_B$ is expected to scale linearly with ρ_s .

Furthermore, it could be argued that the simple mixing length expression (2.25) bases on an assumption invalid for drift-waves. The cross-phase

between density and poloidal electric field fluctuations alters the values of the turbulent diffusivity. This is addressed by a modification of Eq. (2.25) using the average cross-phase proposed in Ref. [45] according to

$$D_\varphi = D \cos(\varphi). \quad (2.26)$$

A detailed introduction of the average cross-phase will be given in Sec. 4.2.3.

In Ref. [46] the scaling of L_c , τ_c and D has been investigated on dimensionally similar discharges in the DIII-D tokamak via the variation of ρ_* by the magnetic field. L_c and τ_c have been obtained from cross-correlation analyses carried out on density fluctuations measured with one-dimensionally arranged multi-channel diagnostics. In this work, the diagnostic is extended to two dimensions (see Sec. 3.2) in order to resolve the spatio-temporal evolution of the density perturbations in the poloidal cross-section by means of cross-correlation analysis techniques specifically developed for this purpose (see Sec. 4.3). The drift-scale ρ_s is varied mainly through the ion mass.

2.5 Turbulence suppression

Since the discovery of spontaneous transitions from low-confinement into high-confinement regimes (L-H transition) in the ASDEX tokamak in 1982 [12], great theoretical and experimental efforts have been made in order to understand the transition into the so-called *H-mode*. $E \times B$ shear flows play an important role in the formation of transport barriers. They can be spontaneously self-excited by turbulence or induced externally. In the following, the phenomenology of the L-H transition is outlined and the shear decorrelation mechanism is described. Two agents of self-excited shear flows are introduced as possible candidates for triggering transitions into H-mode transport barriers. This chapter is closed with the concept of inducing shear flows by external plasma biasing.

2.5.1 The L-H transition

The L-H transition is accompanied by a formation of a transport barrier with low transport coefficients in the plasma edge [13], characterised by steep gradients in density n , temperature T and radial electric field E_r . Decreased fluctuation levels and H_α emission, which is a signature for the particle loss rate, are observed in H-mode discharges. Some insight into the sudden transition is provided by *bifurcation* theory [47, 48, 49]. A bifurcation can take place in particle or heat flux (Γ , Q) as well as in the radial electric field (E_r) as functions of the density or the temperature gradients. As illustrated in Fig. 2.6, the radial particle flux increases at increasing heating input power P up to a threshold P_{th} , where the L-H transition takes place and a bifurcation

2. Plasma confinement and transport

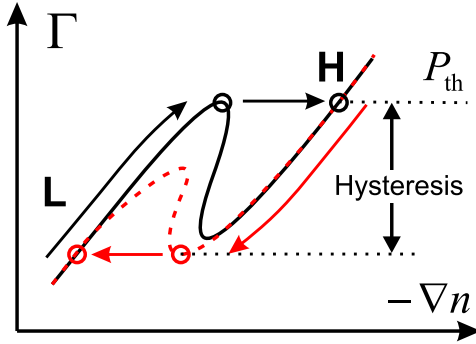


FIG. 2.6: Bifurcation in the density gradient at the L-H transition. H-L and L-H transitions describe a hysteresis in the P - ∇n plane.

of the density gradient is found at constant Γ . According to Fick's law for the particle flux density, $\Gamma = -D\nabla n$, the transition is accompanied by a decrease of the particle diffusivity D . The transition back into the L-mode takes place at values of P lower than P_{th} describing an *hysteresis* in the P - ∇n plane. This suggests that a higher heating power is necessary to reach the H-mode than to stay there. A detailed discussion of L-H transition theories can be found in [44].

2.5.2 Shear decorrelation mechanism

A paradigm for the reduction of turbulent transport in transport barriers bases on sheared radial electric fields [14, 50, 51]. It basically addresses the effect of sheared $E \times B$ flows on growth and radial extent of turbulent eddies. In Fig. 2.7, the effect on turbulent eddies according to the *shear decorrelation mechanism* [14] is sketched. Three situations are opposed. On the left-hand side an eddy without shear of the background flow is depicted (see also Fig. 2.5, left). The advection of fluid elements (squares) can be associated with this eddy as long as they stay in a range, in which the velocity field of the eddy remains correlated and not affected by the flow of adjacent eddies of comparable scale. This defines the *correlation length* L_c and the correlation time or *lifetime* τ_c of the eddy. The latter is often referred to as turbulent decorrelation rate $\omega_t = 1/\tau_c$. Dimensionally, an inhomogeneous, sheared background flow is characterised by a shearing or decorrelation rate ω_s . In the case $\omega_s < \omega_t$ the eddy is distorted and stretched in the flow direction as shown in the middle

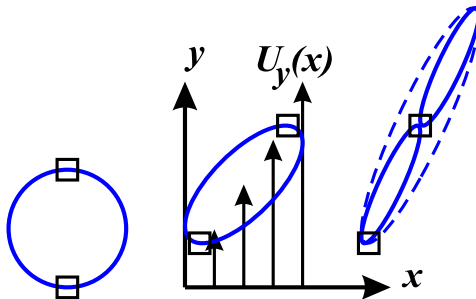


FIG. 2.7: Shear decorrelation mechanism. Left: turbulent eddy without shear in the background flow. Middle: Distortion of the eddy in a sheared flow. Right: breaking of the eddy at strong shear flow.

of Fig. 2.7. For $\omega_s > \omega_t$, the eddy is stretched to its correlation length in a time, which is shorter than τ_c . Thus the eddy is torn apart and the correlation length in shear direction is decreased (Fig. 2.7, right). Accordingly, sheared, poloidal $E \times B$ flows reduce the step size of a random walk process, fluctuation amplitudes and thus radial turbulent transport. More details can be found in, e.g., Ref. [51].

A rough estimate for a critical value of ω_s , at which turbulence is totally suppressed, is the maximum linear growth rate of all unstable modes γ_{\max} [50]. For a number of drift-wave instabilities, a simple stabilisation criterion is given by [52, 44]

$$U'_{\mathbf{E} \times \mathbf{B}} > \gamma_{\max} \approx \frac{c_s}{R_0}, \quad (2.27)$$

where $U'_{\mathbf{E} \times \mathbf{B}}$ denotes the radial derivative of the equilibrium $E \times B$ flow, c_s the sound speed and R_0 the major plasma radius. A more precise evaluation of the shearing rate involves the toroidal geometry of the magnetic field [53]. For the estimation of the maximum linear growth rate, numerical studies on specific models are necessary (see, e.g., Ref. [54]). A further complication arises from temporally varying shear flows, which contribute to the shearing rate but change too fast to efficiently distort eddies and suppress turbulence. The corresponding shearing rate would be overestimated [55].

It has been shown theoretically [56, 57] that turbulent transport can significantly be reduced due to shear flows modifying the cross-phase between poloidal electric field and density fluctuations, even if fluctuation levels are not affected. Experimental [58] and numerical [59] investigations support that the effect of shear flows on the cross-phase can contribute substantially to the reduction of turbulent transport.

2.5.3 Zonal flows

Zonal flows (ZF) are poloidally and toroidally symmetric ($k_\theta = k_\parallel = 0$), radially localised ($k_r \neq 0$) potential structures [15]. They can be described as low frequency $E \times B$ shear flows (see Fig. 2.8) and therefore are important for improving plasma confinement [60]. A detailed understanding of ZFs and their origin is of great interest.

Since $k_\theta = 0$ for the ZF potential, no radial motion is associated (for comparison, see Fig. 2.5). Thus, ZFs cannot tap energy from the background pressure gradient. ZFs are supposed to be driven by turbulent Reynolds stress $R_s = \langle \tilde{u}_r \tilde{u}_\theta \rangle_{\text{zonal}}$ [16]. Similar to the turbulent transport $\Gamma = \langle \tilde{n} \tilde{u}_r \rangle_{\text{zonal}}$ the turbulent Reynolds stress can be understood as a radial transport of poloidal momentum. The Reynolds stress drive of ZFs can be expressed in terms of Fourier components and considered as a mode-coupling problem [17], in which the energy of small-scale drift-waves ($\tilde{u}_r, \tilde{u}_\theta$) is transferred to the large-scale

2. Plasma confinement and transport

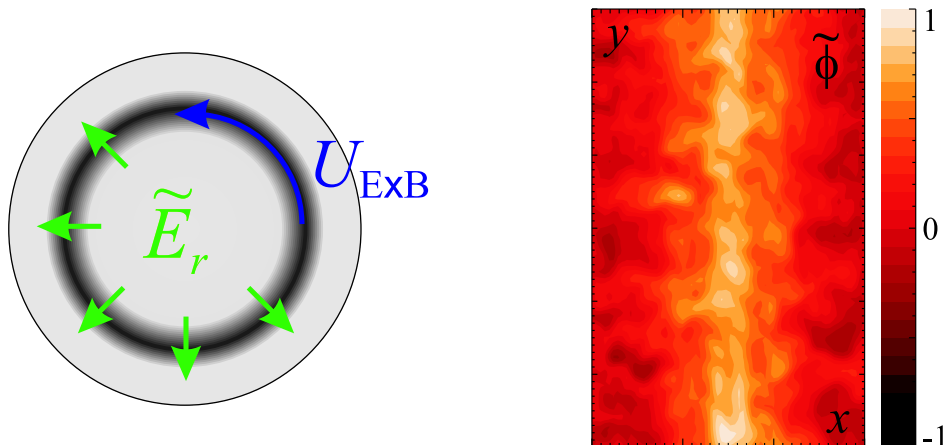


FIG. 2.8: Schematic picture of a zonal flow in the poloidal cross-section (left). A large scale potential perturbation leads to a localised enhancement of the radial electric field and thus to $E \times B$ flow shear. Right: Zonal flow as observed in data simulated by the DALF3 code for a position s on the low-field side. The potential fluctuations have been normalised with the maximum absolute amplitude.

ZF Φ via three-wave interactions associated with the inverse cascade of the turbulent spectra [61]. Cross-bispectral analysis (see Sec. 4.2.4) of these quantities (\tilde{u}_r , \tilde{u}_θ and the ZF potential Φ) is proposed as an experimental tool for the investigation of the ZF drive. Since expensive spatio-temporal multipoint measurements have to be carried out – especially for the zonally averaged ZF potential Φ – an experimental investigation of the driving mechanism is rather difficult. A reduction to auto-bispectral analysis of single fluctuations in density \tilde{n} or plasma potential $\tilde{\phi}$ has been proposed in Refs. [17] and [18], respectively, and an increased degree of three-wave interactions has been observed during the L-H transition as a precursor of $E \times B$ shear flow development in DIII-D [18, 62]. On the other hand it must be stressed that \tilde{n} and $\tilde{\phi}$ have different non-linear properties [63]. In Sec. 6.1, the cross- and auto-bispectral analysis techniques are tested with respect to the Reynolds stress drive on a well defined system – the turbulence simulation code DALF3 – which offers all information needed.

2.5.4 The geodesic acoustic mode

Another candidate for turbulence decorrelation is the *geodesic acoustic mode* (GAM), which should appear together with the pressure side-band $\tilde{p} = \tilde{p}_0 \sin(\theta)$ [64]. The ZF potential together with the inhomogeneous magnetic field causes an asymmetric poloidal $E \times B$ rotation leading to a compression on the top and a decompression on the bottom. The consequence is an up/down asymmetry of the pressure as shown on the left-hand side of Fig. 2.9. This results in a displacement of the pressure contours with respect to the flux surfaces (see Fig. 2.9, right). The dominant restoring force is due to the radial component

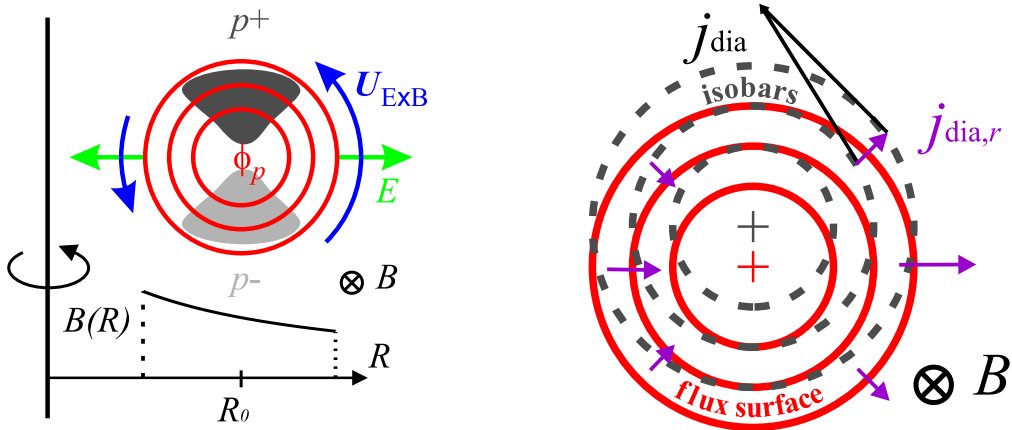


FIG. 2.9: Zonal flow oscillations at the GAM frequency. The zonal flow potential causes pressure asymmetries due to differences in $E \times B$ rotation on the low- and the high-field side (left). The dominant restoring force is due to the radial component of the diamagnetic current and corresponding polarisation current, arising from the displacement between pressure contours and flux surfaces (right).

of the diamagnetic current, which arises from this displacement. These currents change the sign of the radial electric field. As a consequence, the poloidal $E \times B$ rotation velocity starts to oscillate at the GAM frequency, which can roughly be estimated by the propagation velocity of density perturbations parallel to the magnetic field lines, namely the ion sound speed c_s , and the major plasma radius R_0 : $\omega_{\text{GAM}} \sim c_s/R_0$. This is an interesting scaling property for experimental evidence [65, 66]. A detailed expression has been derived in Ref. [67].

GAMs are also referred to as ZFs or ZF oscillation. ZFs and GAMs exhibit similar properties. In wavenumber domain, the properties are the same, but they differ in the frequency. GAMs can be considered as a sink for ZF energy. In toroidal geometry, the ZF energy is depleted into pressure side-bands, which themselves represent a source of free energy for turbulence, transferred via the cascade [68]. This so-called *geodesic transfer effect* is discussed in more detail in Ref. [68]. In Sec. 6.1, it will be studied, whether the oscillating flow contributes to the reduction of turbulent transport. The existence of ZFs/GAMs in TJ-K is discussed in Sec. 6.2.

2.5.5 External plasma biasing

In Fig. 2.10 (left), the biasing scheme as presented in Ref. [19] is shown. A current is drawn by the tip of an insulated probe in order to selectively affect the charge density on a flux surface. This induces electric fields and poloidal $E \times B$ rotation. In a stationary state, the torque associated with a *radial return current* [69] balances friction forces counteracting the poloidal rotation. These friction forces are average forces associated with *magnetic pumping*. Parallel

2. Plasma confinement and transport

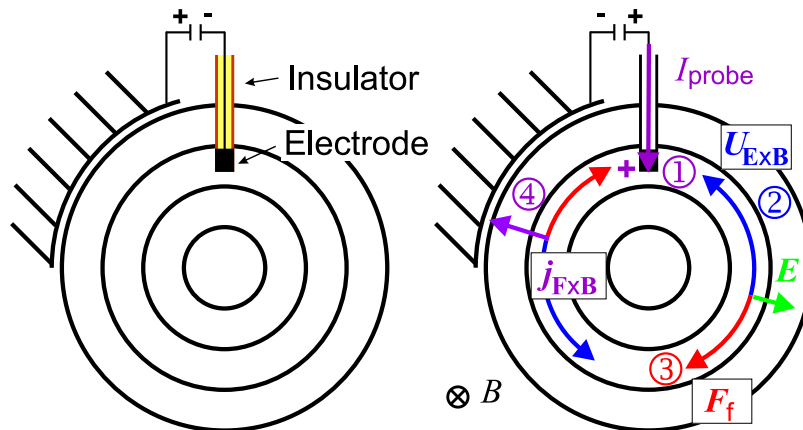


FIG. 2.10: Scheme for plasma biasing on a flux surface according to Ref. [19] (left). Radial electric fields are induced by a current drawn from the probe. Friction forces counteracting the poloidal rotation cause return currents to end up with ambipolarity.

to the magnetic field lines, particles pass regions with low and high magnetic field strength. For particles passing the high-field side, parallel momentum is transferred into perpendicular momentum and redistributed by collisions. Consequently, the redistributed momentum is missing for the transfer into parallel momentum on the low-field side. This corresponds to a friction force entering the equation of motion (2.10) through viscous damping terms, e.g., the parallel viscosity of the poloidal flow [70]. The return current balances the current drawn by the probe, so that global ambipolarity is maintained and the plasma is prevented from charging up indefinitely.

In several experiments – mostly in tokamaks – improved confinement regimes have been achieved by biasing [19, 71, 20, 21]. These and other investigations have supported the importance of radial electric fields in H-mode physics. Bifurcations in the electric field have been found to be due to the destruction of parallel viscosity by strong poloidal plasma rotation [22]. These bifurcations are accompanied by a sudden drop in the current drawn by the probe at increasing bias voltage – a phenomenon, which has been utilised in order to establish the causality between transport reduction and shear in the radial electric field [23]. The shear occurs as a precursor of increased density gradients. Several biasing schemes have been used [72]. Limiter biasing has been found to be less effective than electrode biasing. Positive biasing potential is preferable, since negative biasing is limited by the ion saturation current of the electrode – a drawback, which could be compensated by emissive probes. However, H-mode-like transitions have been induced by both. Very strong shear layers have been induced by separatrix biasing [73]. The applicability of external plasma biasing in TJ-K is investigated in chapter 7.

The experiment TJ-K

The torsatron TJ-K – previously TJ-U1 [74] – is the experiment on which all investigations have been carried out. This chapter describes the experimental setup, and the diagnostics. A characterisation of the equilibrium is given at the end of this chapter.

3.1 Experimental setup

3.1.1 Specifications of the torsatron TJ-K

The torsatron TJ-K [74, 75] is a toroidal plasma device for the investigation of plasma turbulence, waves and heating mechanisms. The geometrical dimensions are listed in Tab. 3.1.

radial dimensions	value
inner radius of torus surface	41.5 cm
outer radius of torus surface	78.5 cm
wall thickness	1.0 cm
centre of poloidal cross-section R_0	60.0 cm
inner radius of poloidal cross-section	17.5 cm

TABLE 3.1: Dimensions of the vacuum vessel of TJ-K.

The geometry is that of a specific stellarator type: Helical magnetic field lines are produced by one ($l = 1$) field coil, which winds helically six times ($m = 6$) around the torus-shaped vacuum vessel. Top and side views of the experiment are shown in Fig. 3.1. Field coils at the top and at the bottom of the vacuum vessel produce a vertical field in order to compensate the vertical component produced by the helical field coil (see Sec. 2.1.2). The smaller vertical field coils shown in Fig. 3.1 are out of use. In the present geometry, magnetic field lines take about three toroidal rotations until they perform one poloidal rotation. Therefore the rotational transform, which in general depends on the plasma radius, is $t \approx 1/3$. Connecting the points, at which one magnetic field line crosses the poloidal cross-section, represents a *magnetic*

3. The experiment TJ-K

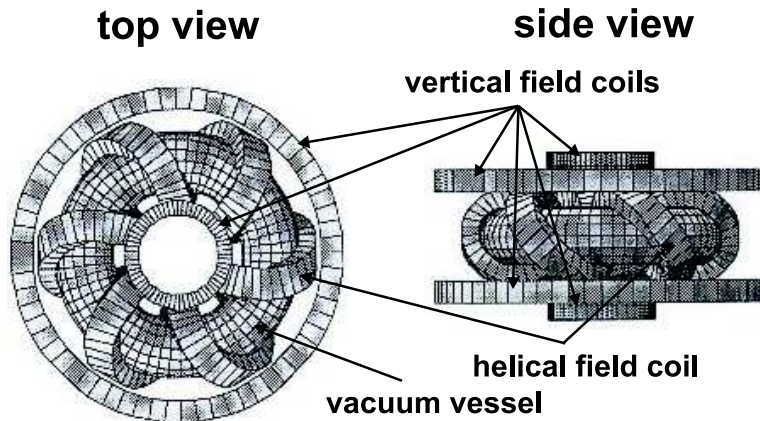


FIG. 3.1: Top view (left) and side view (right) of the vacuum vessel with field coils of the torsatron TJ-K.

flux surface. Due to the six-fold toroidal symmetry of the magnetic field, the shape of the magnetic flux surfaces repeats every 60 degrees in toroidal direction. Varying the ratio $R_{v/h} = I_v/I_h$ of the currents through the vertical and the helical field coils enables horizontal positioning of the flux surfaces. The magnetic flux surfaces have been verified experimentally [76]. They agree rather well with numerical calculations using the Gourdon code [28]. For a ratio of $R_{v/h} = 0.57$, Fig. 3.2 shows an example of the theoretical shape of the flux surfaces at locations of the access ports. With the minor plasma radius $a = 10$ cm determined from an average surface πa^2 of the cross-section inside the separatrix and with a major plasma radius of $R_0 = 60$ cm the inverse *aspect ratio* is $\epsilon = 0.17$.

Each of the six sections is accessible through four ports. These ports are counted clockwise as shown in Fig. 3.2. Bottom, outer and top ports are ISO-KF250 flanges. The inner ports are restricted to smaller ISO-KF63 flanges because of the helical field coil. A turbo molecular pump at port (B2) evacuates the vessel down to a pressure of 2×10^{-7} mbar. As measured with a mass spectrometer at port (T3), water dominates the base pressure. TJ-K is operated with the gases hydrogen, deuterium, helium, neon and argon through a gas feed at port (T3). The working pressure is in the range 10^{-5} to 10^{-4} mbar as measured by a PFEIFFER Compact FullRangetm Gauge at port (T4) and manually controlled with a dosing valve. The gauge consists of a Pirani for the measurement of pressures above 10^{-2} mbar and a Penning for pressures below. Thus, the indicated working pressure in general depends on the type of gas being used. Throughout this work, the reference value for dry air is given. 1D- and 2D-movable manipulator systems are installed at the ports (O5, T5) and (O6), respectively. These systems can be separated from the main vessel by gate valves allowing for an exchange of diagnostics at a minimal impact on the vacuum.

3.1 Experimental setup

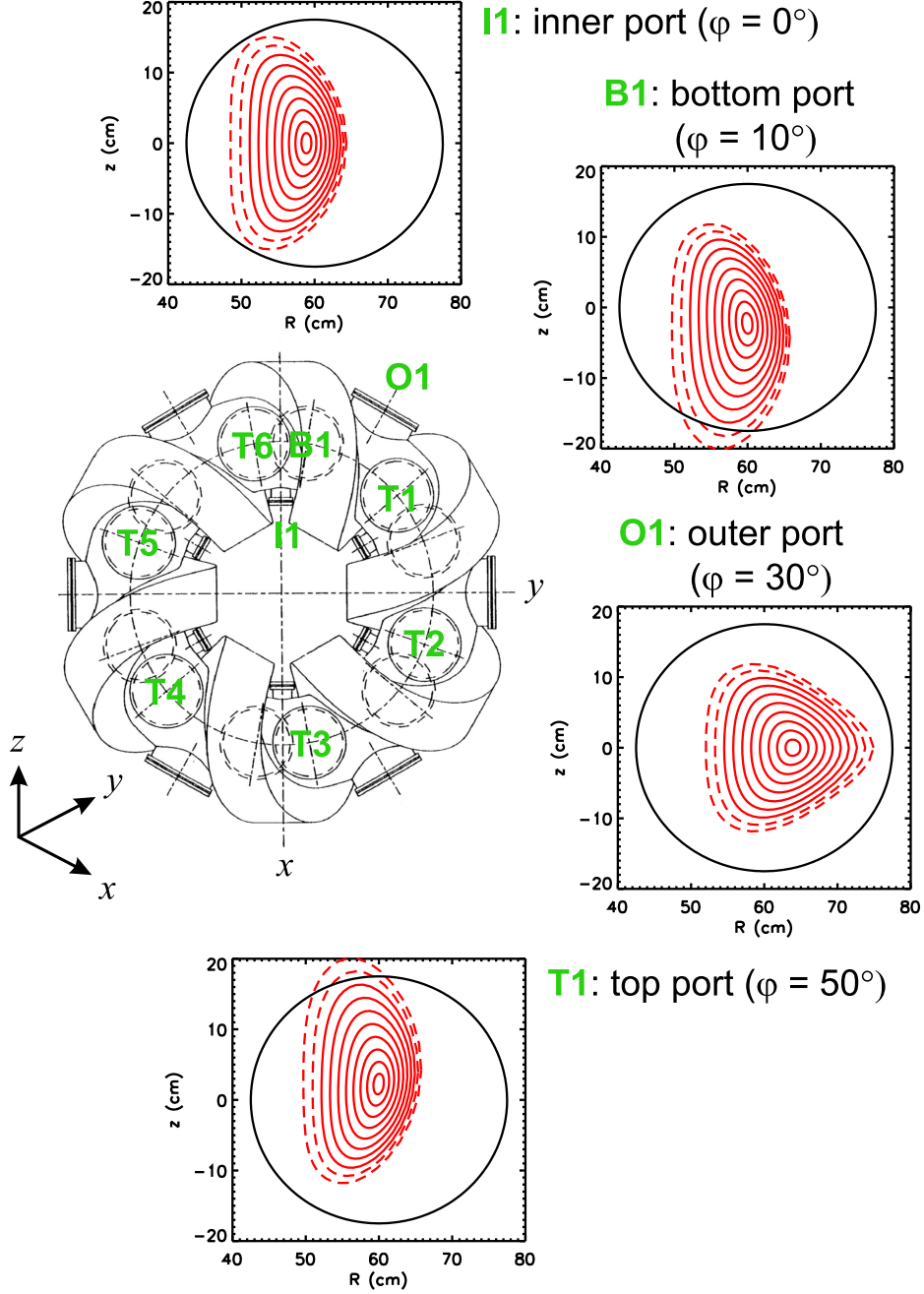


FIG. 3.2: Magnetic flux surfaces in TJ-K for $R_{v/h} = 0.57$ at the inner port (I1), the bottom port (B1), the outer port (O1) and the top port (T1). Flux surfaces inside the separatrix are depicted by solid lines. Dashed lines show flux surfaces outside the separatrix. In the top-view, the ports are counted clockwise as indicated for the other five top ports.

3. The experiment TJ-K

3.1.2 Plasma source

The heating mechanism for producing plasma used in this work is *electron-cyclotron-resonant heating* (ECRH). In previous investigations, helicon waves have been used as a plasma source and plasma properties of ECRH and helicon plasmas have been compared [77, 25]. In ECRH discharges, microwaves are resonantly absorbed by electrons gyrating at the *electron-cyclotron frequency* (2.1) $\omega_{ce} = eB/m_e$ set by the local magnetic field strength. Details on the theory of waves in plasmas can be found in Ref. [78]. Ref. [79] provides an introductory overview.

In TJ-K, a magnetron at 2.45 GHz microwave and 6 kW is used. The microwave passes a waveguide and is injected through a quartz window at port (B4). Matching the injection of the microwave to minimum reflected power is possible through a stub tuner. The electric field is polarised parallel to the confining magnetic field, which is the *O-mode* configuration and for which the cut-off density is $n_{e,c} \approx 7.5 \times 10^{16} \text{ m}^{-3}$ [80]. Due to the resonance condition, ECRH is possible in the range of the nominal field of $70 \text{ mT} < B < 100 \text{ mT}$. The plasma densities achieved in TJ-K are well above the cut-off density. Thus, ECRH should be localised at the edge. Nevertheless, centrally peaked density profiles are obtained. This might be explained by an inward particle pinch. On the other hand, the heating may take place at the core through *O-X-B conversion* [81]. Detailed investigations of the heating mechanism are in progress.

3.1.3 Plasma parameters

For a given helical current I_h , the magnetic field strength on the magnetic axis is $B \approx I_h \times 0.24 \times 10^{-3} \text{ T/A}$. Typical plasma parameters are $n_e \approx 5 \times 10^{17} \text{ m}^{-3}$ and $T_e \approx 10 \text{ eV}$. Ions have been measured to be cold ($T_i \approx 1 \text{ eV}$) by passive spectroscopy [82]. Spectroscopic measurements on argon plasmas showed that the ions are single charged. Magnetic field strengths of up to 0.3 T are possible. The magnetic field points counterclockwise. The coils are passively water cooled, so that the discharge duration is limited to 40 minutes at a typical current of $I_h = 300 \text{ A}$. Other typical plasma parameters are listed in Tab. 3.2. The discharges are dimensionally similar to the edge of fusion plasmas [24]. Since – in contrast to fusion plasmas – the plasma produced in TJ-K is of rather low temperature, its advantage is to be accessible for probes.

3.2 Diagnostics

The principal diagnostics used in this work are electrostatic probes. These probes feature a high spatial and – under some limitations – temporal resolution necessary for turbulence studies. In fusion plasmas, due to the high

3.2 Diagnostics

parameter	formula	typical value
electron plasma frequency	$\omega_{p,e} = \sqrt{\frac{ne^2}{\epsilon_0 m_e}}$	40.0×10^9 rad/s
ion plasma frequency	$\omega_{p,i} = \sqrt{\frac{ne^2}{\epsilon_0 m_i}}$	$0.1 - 1.0 \times 10^9$ rad/s
electron cyclotron frequency	$\omega_{c,e} = \frac{eB}{m_e}$	14.0×10^9 rad/s
ion cyclotron frequency	$\omega_{c,i} = \frac{eB}{m_i}$	$0.2 - 8.0 \times 10^6$ rad/s
thermal electron velocity	$v_{th,e} = \sqrt{\frac{2k_B T_e}{m_e}}$	2.0×10^6 m/s
thermal ion velocity	$v_{th,i} = \sqrt{\frac{2k_B T_i}{m_i}}$	$2.0 - 14.0 \times 10^3$ m/s
electron gyro-radius	$r_{L,e} = \frac{v_{th,e}}{\omega_{c,e}}$	0.1×10^{-3} m
ion gyro-radius	$r_{L,i} = \frac{v_{th,i}}{\omega_{c,i}}$	$2.0 - 11.0 \times 10^{-3}$ m
Debye length	$\lambda_D = \sqrt{\frac{\epsilon_0 k_B T_e}{ne^2}}$	33.0×10^{-6} m

TABLE 3.2: Characteristic frequencies and lengths for typical plasma parameters in TJ-K. These values are $T_e = 10$ eV, $T_i = 1$ eV, $n = 5 \times 10^{17} \text{ m}^{-3}$ and $B = 82$ mT.

heat load, only the edge region is accessible by material probes, whereas in TJ-K probes can be established throughout the plasma. The ease of accessibility makes TJ-K very interesting for turbulence studies. First in this section, a non-intrusive diagnostic for measuring the plasma density is introduced. Subsequently the concept of Langmuir probes is described. Details on electromagnetic wave field measurements by \vec{B} probes and on measurements of the ion temperature by passive spectroscopy in TJ-K can be found in Refs. [77, 82], respectively.

3.2.1 Microwave interferometry

For electro-magnetic waves propagating in an unmagnetised plasma the refraction index of the plasma is given by

$$N_p = \sqrt{1 - \omega_p^2/\omega^2}, \quad (3.1)$$

where $\omega_p = \sqrt{ne^2/\epsilon_0 m_e}$ is the electron plasma frequency. The refraction index essentially depends on the density n_e . At the *cut-off density* $n_{co} = \omega^2 \epsilon_0 m_e / e^2$,

3. The experiment TJ-K

the refraction index becomes imaginary and the wave is reflected. Electromagnetic waves, which have a sufficiently high cut-off density, can be used to measure the plasma density by interferometry. To this end, a microwave is split up into two branches, one branch traversing the plasma and a non-traversing reference branch. The phase shift of that branch, which has traversed the plasma of density $n_e(l)$ along a path l with respect to the reference is given by the integral

$$\Delta\Phi = \int_0^L dl \frac{\omega}{c} (1 - N_p) \approx \frac{e^2}{2c\epsilon_0 m_e \omega} \bar{n}_e L, \quad (3.2)$$

where $\bar{n}_e = \int_L n_e(l) dl/L$ is the line averaged electron density. In magnetised plasmas, this consideration stays valid for the O-mode. The phase shift can be measured by interfering both branches.

In TJ-K, an heterogeneous microwave interferometer is used at a frequency of $f = 64$ GHz. Plasma densities in TJ-K are well below the cut-off density of $n_{co} = 5.1 \times 10^{19} \text{ m}^{-3}$. The microwave is launched through an horn antenna at port (O4) and reflected at a mirror on the inboard side of the vacuum vessel. The reflected wave is received by a second antenna adjacent to the emitting one. The change in the output voltage is related to the phase difference between launched and received wave according to $\Delta\Phi = 2\pi \times 17.52/360 \times \Delta U/V$. Finally, the line averaged density is given by $\bar{n}_e \approx 6.7 \times 10^{16} \text{ m}^{-3} \times \Delta U/V$, where $L \approx 2 \times 0.17 \text{ m}$ is used. For details see Ref. [83].

3.2.2 Langmuir probes

The most commonly used *electrostatic probe* consists of a tungsten wire, which is insulated by a ceramic tube except of a small tip (see Fig. 3.3, left). Once the tip is brought into the plasma at a desired position the tip is biased and a current is drawn in order to analyse the current-voltage characteristic of the probe. From this characteristic the electron temperature T_e , the plasma density n and the plasma potential ϕ_p can be obtained.

The technique was developed by Irving Langmuir and is therefore called the method of *Langmuir probes*. As depicted on the right hand side of Fig. 3.3, characteristics from a Langmuir probe are classified into three regions. For historical reasons, the negative current is plotted against the bias. If the probe is biased sufficiently negative, all electrons are repelled and only ions contribute to the current drawn by the probe. At sufficiently negative bias all ions in the vicinity of the probe are collected and the ion-current saturates (region A in Fig. 3.3).

Reducing the bias, more and more electrons have sufficient kinetic energy to reach the probe. The contribution of the electrons to the current drawn by the probe increases exponentially until the probe bias equals the *plasma potential* ϕ_p (region B in Fig. 3.3). Ambipolarity demands that the net current

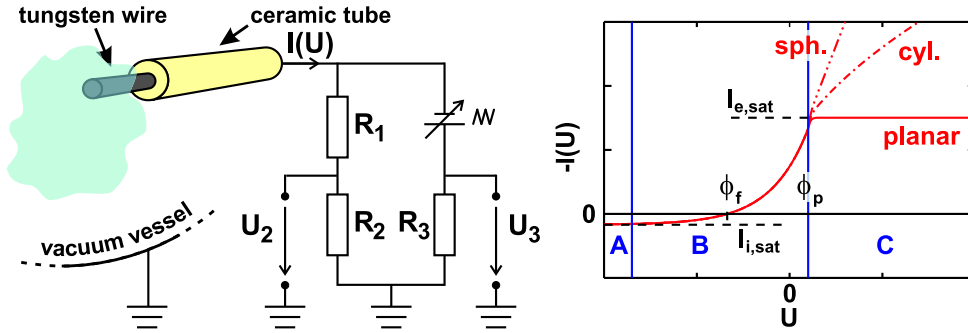


FIG. 3.3: Left: Langmuir probe and electric circuit. Right: Schematic representation of a characteristic of a Langmuir probe. The characteristic is classified into three regions: A) saturation of ion current, B) electron-starting range, C) saturation of electron current. The electron current does not saturate in the case of cylindrical and spherical probes.

to the probe is zero if no bias is applied, i.e., if the probe is floating. Due to the higher mobility of the electrons in comparison with the ions, the probe is charged negatively with respect to the plasma potential. The probe is charged to the so called *floating potential* ϕ_f .

The third region (region C) begins at the plasma potential. Here electrons of arbitrary energy can reach the probe. In the ideal case – the probe is planar and of infinite size – all electrons in the vicinity of the probe are collected and the electron current saturates. In practice, mostly cylindrical probes or sometimes spherical probes are used. They can be regarded as planar, if the *Debye shielding length* $\lambda_D = \sqrt{\epsilon_0 T / e^2 n}$ is much smaller than typical probe dimensions d . In the opposite case, $\lambda_D \gtrsim d$, the current is magnified by geometrical factors due to orbital motions of charged particles around the probe (*orbital motion limit*), which lead to an enlargement of the collection area of the probe at increasing bias.

Analytical expressions for the probe current follow from the simple probe theory, which is valid for sufficiently planar probes in collision-less unmagnetised plasmas, where electrons are Maxwellian and isotropically distributed. Cold ions are assumed. The expressions read

$$(A) \quad I = I_{i,\text{sat}} = 0.61 en S \sqrt{\frac{T_e}{M_i}} \quad (3.3)$$

$$(B) \quad I = I_{i,\text{sat}} + I_{e,\text{sat}} \exp\left(-\frac{e(\phi_p - U)}{T_e}\right) \quad (3.4)$$

$$(C) \quad I = I_{e,\text{sat}} = -en S \sqrt{\frac{T_e}{2\pi m_e}} \quad (3.5)$$

for the region A, B and C respectively, where T_e is the electron temperature, M_i and m_e the ion and the electron mass, e the elementary charge, n the

3. The experiment TJ-K

density and S is the effective probe surface, which in case of $\lambda_D \ll d$ is approximately the actual probe surface. For the opposite case the geometrical factors mentioned above are given in Ref. [84]. For region B, a fit formula is provided by

$$I = 0.61 enS \sqrt{\frac{T_e}{M_i}} \left\{ 1 - \exp\left(-\frac{e(\phi_f - U)}{T_e}\right) \right\}, \quad (3.6)$$

where the plasma potential has been replaced by

$$\phi_p = \phi_f - \frac{T_e}{e} \ln\left(0.61 \sqrt{2\pi \frac{m_e}{M_i}}\right), \quad (3.7)$$

which follows from $I = 0$ at $U = \phi_f$.

Collisions and magnetic field effect the characteristic in such a way as to reduce the current to the probe. In the case of collisions, the current is reduced, because particles get to the probe by diffusion rather than by free flight. Magnetic fields restrict the perpendicular motion. The effect of collisions can be neglected if the mean free path is larger compared to d and the plasma can be regarded as unmagnetised – with respect to the probe dimensions – if the Larmor radii $\rho \gg d$ [85]. These conditions are not necessarily fulfilled. Plasma potential and densities evaluated from probe characteristics have to be interpreted with caution, since the effective probe surface S is often unknown. The exponential behaviour near the floating potential in region B provides an adequate estimate of the electron temperature for a thermal electron population.

A method for the evaluation of the *electron energy distribution* (EED) in non-thermal plasmas is provided by kinetic theory. For details see Refs. [86, 87, 88]. The EED can be used to distinguish between electron populations of different mean energies, which become manifest in contributions of different Maxwellian distributions to the EED. Detailed comparative studies of the simple and the kinetic theory with respect to the detection of fast electron components as indicator of the localisation of ECRH are subject to a separate work. The electrostatic probes used in this work are described in detail in the following.

Swept Langmuir probe

In order to measure radial profiles of the electron temperature, a Langmuir probe is installed on the 1D-movable manipulator unit at port (O5). A cylindrical tungsten tip with a length of 1 mm and a diameter of 200 μm is used. The tungsten wire is connected to the circuit shown in Fig. 3.3 via SMB feed-throughs. The bias voltage is ramped at 10 Hz in the range ± 100 V. After the probe has been positioned, the voltages U_2 and U_3 (see Fig. 3.3) are simultaneously acquired by a National Instruments 16-Bit PCI-6014-DAQ-card.

The data is sampled at 100 kHz over 25 k values. Before acquisition, the signal is amplified through an Tektronix differential amplifier AM502. The actual probe characteristic is evaluated with respect to the circuit with $R_1 = 482 \text{ k}\Omega$, $R_2 = 24 \text{ k}\Omega$ and $R_3 = 1 \text{ k}\Omega$. From several realisations of the characteristic in one data-set, an average characteristic is calculated. A non-linear fit using Eq. (3.6) is performed on the characteristic in a range from ion saturation to approximately T_e/e above the floating potential, yielding estimates of T_e , ϕ_f , n and – together with Eq. (3.7) – ϕ_p . In comparative studies using emissive probes [30], the estimate for ϕ_p has not been proven to be adequate. For absolute plasma densities, the profiles are normalised to the line averaged density obtained by microwave interferometry.

Single bias operation

The shape of the plasma density profile is more easily obtained from the ion saturation current, provided that T_e does not vary much. Therefore, the probe is biased to approximately -90 V using a battery as power supply in the circuit in Fig. 3.3 without the voltage divider. Similarly, the floating potential can be measured without any bias but using a 1:20 voltage divider with a total resistance of 1 M Ω .

Furthermore, electrostatic probes operated this way are capable of following turbulent fluctuations $\tilde{\phi}_f$ and $\tilde{I}_{i,sat}$ of the floating potential and the ion saturation current. Neglecting fluctuations of T_e , these quantities are representative for plasma potential and density fluctuations, respectively. Detailed investigations [89] point to the contribution of temperature fluctuations being negligible in TJ-K. Two special applications are used in this work: the transport probe and the 8×8 probe matrix.

The transport probe

The transport probe consists of three Langmuir probes vertically aligned at a distance of 5 mm. The centre probe measures fluctuations $\tilde{I}_{i,sat}$ of the ion saturation current representing \tilde{n} . Both outer probes measure floating potential fluctuations $\tilde{\phi}_f$, the difference providing a measure of the fluctuating vertical (poloidal) electric field \tilde{E}_θ at the centre probe. The transport probe is installed on the 2D-movable unit at port (O6). All three signals are simultaneously acquired by a National Instruments 12-Bit PCI-6110E-DAQ-card at sampling rates up to 1 MHz. Before acquisition, the signals are driven and AC filtered by AM502s, which are connected to the SMB feed-throughs via shielded RG-174 cables. The lengths of these coaxial cables are kept short (< 1.5 m) in order to avoid low-pass filtering due to their capacity. Data from the transport probe provide information on the local time-dependent turbulent transport (see Sec. 2.3.5).

3. The experiment TJ-K

The 8×8 probe array

For the investigation of turbulence in confined plasmas, multi-probe arrays have been proven as adequate [4]. In this work, a probe array is used, which consists of 8×8 horizontally and vertically arranged Langmuir probes covering a spatial grid on the low-field side of the poloidal cross-section with a resolution of 10 mm in both directions. A picture of the matrix is shown on the left-hand side of Fig. 3.4. Each probe consists of a tungsten wire 200 μm in diameter, insulated against the plasma by a ceramic tube of 0.8 mm diameter. The vertically (poloidally) oriented probe tips have a length of 4 mm. Bundles of eight probes, which are stacked in toroidal direction, are mounted on carriers. The radial position of the matrix centre can be varied in the range $R - R_0 = 9 \text{ cm}$ to 13 cm.

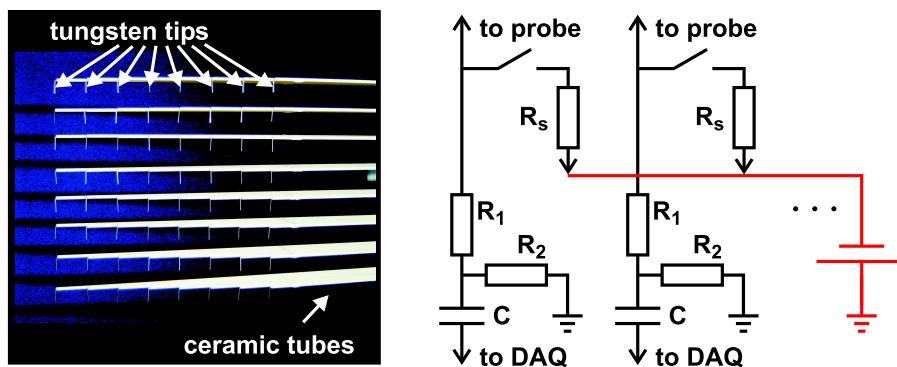


FIG. 3.4: Left: 8×8 -probe matrix. Right: Circuit adapted from Ref. [25]. Only one battery serves as power supply for all 64 probes. The biased operation is optional, also allowing for measurements of the floating potential. The capacitor C together with the input resistor of the data acquisition system forms a high-pass filter.

For the measurement of the ion-saturation currents, all probes are negatively biased over a shunt $R_s = 22 \text{ k}\Omega$ by a single battery as shown in Fig. 3.4 (right). The shunt must be relatively large in order to avoid crosstalk of the channels. The voltage drop over R_s together with the bias voltage is measured over a 61:1 divider with $R_1 = 976 \text{ k}\Omega$ and $R_2 = 16.35 \text{ k}\Omega$. All channels are simultaneously acquired by a 16-Bit 64-channel transient recorder. The DC part is removed by a capacitor, which together with the input resistor $R = 1 \text{ M}\Omega$ of each channel acts as a high-pass filter with a cut-off frequency $\omega_{co} = 10 \text{ Hz}$. On each channel a large number of values (512 k – 1024 k values) is acquired at a rate up to $f = 1.25 \text{ MHz}$. Applying a bias is optional for each probe, so that also fluctuations of the floating potential can be measured. In a previous work [25] this technique has been applied to a multi-probe array, which was poloidally aligned to a flux surface at the density gradient. The 8×8 probe array is an enhanced diagnostic. In particular, the matrix captures the full two-dimensional structure of the turbulence in the poloidal cross-section. It does not suffer from possible artificial effects arising from the one-dimensional

alignment of multi-probe arrays as discussed in Ref. [6].

3.3 Equilibrium properties

Radial equilibrium profiles of the main plasma parameters n , T_e and ϕ_f are presented and essential features are described. Radial profiles of the poloidal flow velocities provide some insight into the dynamics in TJ-K.

3.3.1 Profiles of the main plasma parameters

For typical discharge parameters, an example of radial equilibrium profiles is shown in Fig. 3.5. As a general feature, the density profiles are centrally peaked. For small ion masses up to helium, the profiles are very similar with comparable absolute values and maximum values of $2\text{--}3 \times 10^{17} \text{ m}^{-3}$. Higher densities are found in neon and argon with maximum values of about 10^{18} m^{-3} for neon. Electron temperature profiles are generally hollow with pronounced maxima at the separatrix and values between 4 and 20 eV. The floating potential profiles possess a maximum at the centre of the plasma column and prominent minima near the separatrix, which roughly reflects the shape of the actual plasma potential [30]. This points to ions being better confined inside the separatrix. In Ref. [30], direct electron losses due to the curvature

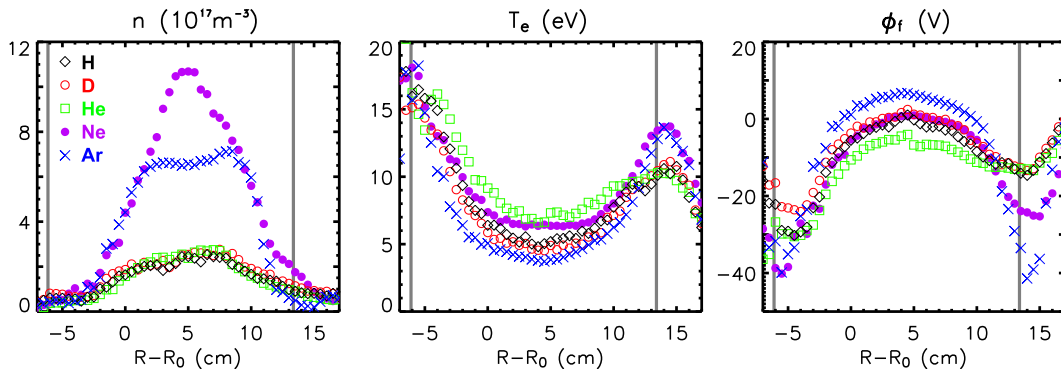


FIG. 3.5: Radial equilibrium profiles of plasma density (left), electron temperature (middle) and floating potential (right) obtained from swept Langmuir probe measurements for the gases hydrogen (#2820), deuterium (#2811), helium (#2815), neon (#2929) and argon (#2805) at discharge parameters $p = 3 \times 10^{-5}$ mbar, $P_{\text{ECRH}} = 1.8$ kW, $I_h = 300$ A and a current ratio of $R_{v/h} = 0.57$. The densities have been normalised to the interferometer. The calculated separatrix is located at $R - R_0 = -6.1$ cm and $R - R_0 = 13.2$ cm as marked by vertical lines.

drift are proposed as a possible explanation of the considerably positive radial electric fields in TJ-K. Outside the separatrix the potential increases again, which could be attributed to the higher mobility of the electrons parallel to

3. The experiment TJ-K

the magnetic field lines ending on the vacuum vessel, where the electrons can flow off. The radial electric field reverses at the separatrix, forming a natural shear layer for the $E \times B$ velocity. The influence of this shear layer on turbulent structures is discussed in Sec. 6.2.

Essential features are still the same for other discharge parameters. Increasing the neutral gas pressure leads to a flattening of the density profiles and a slight trend towards smaller temperatures is observed. Increasing the magnetic field strength has a similar effect on the density as has the neutral gas pressure. In hydrogen and deuterium discharges, hollow density profiles were observed at higher pressures and/or magnetic field strengths. Increasing the heating power basically increases the density.

3.3.2 Profiles of the poloidal flow velocity

In Fig. 3.6, poloidal $E \times B$ and electron-diamagnetic-drift velocities are shown. These drift velocities were calculated from the profiles in Fig. 3.5. The $E \times$

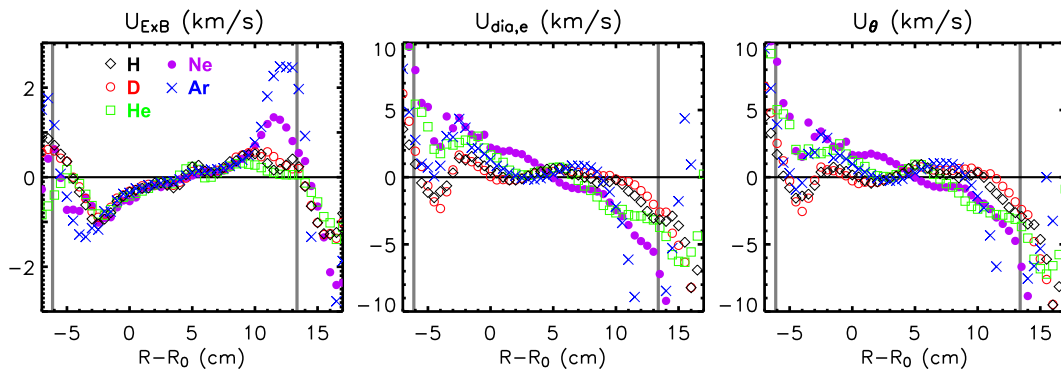


FIG. 3.6: Radial profiles of the poloidal $E \times B$ drift (left), the poloidal electron-diamagnetic drift (middle) and the total poloidal flow $U_{\theta} = U_{E \times B} + U_{dia,e}$ (right) as calculated from the density, temperature and floating potential profiles in Fig. 3.5. The $E \times B$ drift has been corrected by a factor of 1/10 (see text).

B velocity is estimated from the floating potential corrected by a factor of 1/10, since radial electric fields evaluated from floating potential profiles turned out to be overestimated by an order of magnitude [30]. Radial profiles of B have been taken into account using numerical results from the Gourdon code. In terms of a vertical drift pointing upwards, the drifts change sign on the magnetic axis at $R - R_0 = 3.9$ cm. Inside the separatrix, the $E \times B$ flow points counterclockwise. The electron-diamagnetic drift essentially points clockwise. Under the assumption made for the radial electric fields from floating potential profiles, the clockwise electron-diamagnetic drift tends to dominate the total poloidal flow. Hence, for drift-wave turbulence, density perturbations should propagate clockwise in the poloidal cross-section.

Data analysis

In this chapter statistical tools and techniques needed for the analysis and characterisation of fluctuating quantities are introduced. These analysis techniques range from statistical moments of probability density functions over correlation functions to the decomposition into Fourier components. A detailed introduction into the discretisation of time series, the estimation of statistical moments as well as correlation and spectral functions can be found in Ref. [90].

4.1 Statistical data analysis

Turbulent fluctuations are stochastic. Under the assumption that corresponding time series are sufficiently long and stationary, they are adequately characterised by statistical moments of their probability density function. Correlation analysis techniques can be used in order to analyse the temporal behaviour of the fluctuating quantity. In practice, time series $x(t)$ are available in a discrete form $\{x_n\}$, sequentially sampled in constant distances δt in time with N values $x_n = x(t_n)$ and $t_n = n\delta t$ for $n = 0, \dots, N - 1$. For simplification, the time series is assumed to be stationary, i.e., its statistical properties are time independent. *Fluctuations* are mean free ($\langle \tilde{x} \rangle = 0$) and often denoted by a tilde \tilde{x} in literature.

4.1.1 Probability density function

The *probability density function* (PDF) $P(x) dx$ specifies the probability of finding x between x and $x + dx$. Usually, the PDF is represented by a histogram. Normal, i.e., Gaussian PDFs

$$P(x) = \frac{1}{\sigma\sqrt{2\pi}} \exp\left(-\frac{(x - \langle x \rangle)^2}{2\sigma_x^2}\right) \quad (4.1)$$

are fully determined by the *mean value*

$$\langle x \rangle = \int_{-\infty}^{+\infty} dx x P(x) \approx \frac{1}{N} \sum_{i=0}^{N-1} x_i \quad (4.2)$$

4. Data analysis

and the *variance*

$$\begin{aligned}\sigma_x^2 &= \langle (x - \langle x \rangle)^2 \rangle = \int_{-\infty}^{+\infty} dx (x - \langle x \rangle)^2 P(x) \\ &\approx \frac{1}{N-1} \sum_{i=0}^{N-1} (x_i - \langle x \rangle)^2.\end{aligned}\quad (4.3)$$

The estimates for N discretely sampled values are given by the last term in Eqs. (4.2) and (4.3). The *standard deviation* σ_x specifies the $1/e$ -width of the PDF. In plasma physics the standard deviation is commonly used as a measure of the *fluctuation degree* [91].

A measure for the deviation from a Gaussian PDF is provided by normalised versions of the third and fourth moments $m_k \equiv \langle (x - \langle x \rangle)^k \rangle$, $k = 3, 4$. The *skewness*, defined by

$$S \equiv m_3/m_2^{3/2} \approx \frac{1}{N} \sum_{i=0}^{N-1} \left(\frac{x_i - \langle x \rangle}{\sigma_x} \right)^3, \quad (4.4)$$

measures the asymmetry of the PDF. In comparison with a Gaussian PDF ($S = 0$) positive or negative values of the skewness indicate an asymmetric tail in the direction of positive or negative x , respectively. A measure for how flat or peaked the PDF is given by the *kurtosis*

$$K \equiv m_4/m_2^2 - 3 \approx \left\{ \frac{1}{N} \sum_{i=0}^{N-1} \left(\frac{x_i - \langle x \rangle}{\sigma_x} \right)^4 \right\} - 3. \quad (4.5)$$

With respect to a Gaussian PDF ($K = 0$) a positive kurtosis indicates a more peaked maximum with the tails having a weaker slope. Negative values indicate a comparatively flat maximum and a stronger slope of the tails.

4.1.2 Correlation functions

A normalised version of the *covariance* $\text{cov}(x, y) \equiv \langle (x - \langle x \rangle)(y - \langle y \rangle) \rangle$ defines the *cross-correlation* of two time series $x(t)$ and $y(t)$ with $\langle x \rangle = \langle y \rangle = 0$ as a function of a time lag Δt in the form

$$C_{x,y}(\Delta t) = \frac{\langle x(t)y(t+\Delta t) \rangle}{\sigma_x \sigma_y} = \int_{-\infty}^{\infty} dt \frac{x(t)y(t+\Delta t)}{\sigma_x \sigma_y}, \quad (4.6)$$

where the *ensemble average* $\langle \cdot \rangle$ is replaced by the time average under the assumption of *ergodicity*. Note that in the most common definition for complex valued functions, x is replaced by its complex conjugate. $C_{x,y}$ is limited to $[-1, 1]$ due to the normalisation by the respective standard deviations $\sigma_{x,y}$. The cross-correlation function measures the degree of agreement of two time

series. Values of 1 at a certain time lag indicate a total agreement except of a factor. Both time series are totally correlated. For values of -1 , they are totally anti-correlated, which means $x(t) \sim -y(t + \Delta t)$. No correlation at all is indicated by values of zero. In particular, the *auto-correlation* $C_{x,x}$ provides information on the time scale the time series stays self-correlated. It is $C_{x,x}(0) = 1$. In Sec. 4.3, a special analysis technique is developed for the investigation of scaling properties of turbulent structures using the cross-correlation function.

4.2 Spectral analysis

Spatio-temporal wave phenomena occurring in the dynamics of plasma parameters in terms of interactions and coupling are investigated by means of decomposition of time series into Fourier components. In order to obtain significant estimates for spectral functions, the random nature of fluctuating quantities in Fourier space must be taken into account.

4.2.1 Cross-power spectrum

The discrete forward and inverse Fourier transforms of a function $x(t)$ read

$$\hat{x}(\omega_j) = \frac{1}{N} \sum_n x(t_n) \exp(-i\omega_j t_n) \quad \text{and} \quad x(t_n) = \sum_j \hat{x}(\omega_j) \exp(i\omega_j t_n), \quad (4.7)$$

respectively, where $\omega_j = j\delta\omega$, $j = -N/2, \dots, N/2$ and $\delta\omega = 2\pi/N\delta t$. According to the *sampling theorem*, $x_n = x(t_n)$ can be reproduced from $\hat{x} = \hat{x}(\omega_j)$, if the sampling frequency $\omega = 2\pi/\delta t$ is at least twice as large as the maximum frequency occurring in the signal. The maximum resolvable frequency in the discrete Fourier spectrum therefore is the *Nyquist-frequency* $\omega_{\text{Ny}} = \pi/\delta t$. From many realisations of the Fourier spectra of two quantities x and y , an estimate for the *cross-power spectrum* is obtained, which – similar to the cross-correlation in the time domain – reveals information on the correlation between two different quantities in the Fourier domain.

The estimate is given by

$$H_{x,y}(\omega_j) = \langle \hat{x}^*(\omega_j) \hat{y}(\omega_j) \rangle \quad (4.8)$$

$$= h_{x,y}(\omega_j) \exp(i\varphi(\omega_j)) \quad (4.9)$$

in two representations, where the asterisk denotes the complex conjugate and the brackets $\langle \cdot \rangle$ ensemble averaging. In practice, the realisations are taken from consecutive sub-series of one large time series. In Eq. (4.9), the cross-power spectrum is decomposed into the *cross-amplitude spectrum* $h_{x,y}(\omega_j)$ and a phase factor including the *cross-phase spectrum* $\varphi(\omega_j)$. For a statistically

4. Data analysis

distributed cross-phase at ω_j , no coherent phase relation is present at this frequency and the contribution to the cross-power vanishes on the average. Finite contributions are only possible, if there is a mean coherent phase relation. A measure of the phase coherence is provided by the *cross-coherence spectrum* defined by

$$\gamma(\omega_j) = \frac{h_{x,y}(\omega_j)}{\sqrt{h_{x,x}(\omega_j) h_{y,y}(\omega_j)}}. \quad (4.10)$$

$\gamma(\omega_j)$ is limited to $[0, 1]$, where 0 and 1 indicate phase incoherence and coherence, respectively. Values between indicate partial phase coherence. More details can be found in Refs. [90, 92, 93]. For practical applications, it is interesting to note that the cross-correlation and the cross-power spectrum are related via the *Wiener-Khintchine theorem*

$$C_{x,y}(\Delta t) = \sum_j \hat{x}^*(\omega_j) \hat{y}(\omega_j) \exp(i\omega_j \Delta t). \quad (4.11)$$

Standard deviations of unity are assumed here. Furthermore, it follows from Eq. (2.21) that the cross-correlation is equal to the inverse Fourier transform of the cross-power spectrum. In Sec. 4.3, relation (4.11) will be used together with the *Fast-Fourier-Transform algorithm* (FFT) (see, e.g., Ref. [94]) in order to reduce computational costs of the rather extensive calculations during this work. In the following, a special case of the cross-power spectrum, the auto-power spectrum will be introduced and the average cross-phase used in Eq. (2.26) will be related to the spectral cross-phases.

4.2.2 Auto-power spectrum

The *auto-power spectrum* as estimated by

$$S_x(\omega_j) = \langle |\hat{x}(\omega_j)|^2 \rangle \quad (4.12)$$

gives a measure of the mean power contribution of harmonic components of x at frequencies in $[\omega_j, \omega_j + \delta\omega]$ to the total signal power. With $S_x(\omega) = H_{x,x}(\omega) = h_{x,x}(\omega)$, the auto-power spectrum is related to the auto-correlation via the Wiener-Khintchine theorem. A consequence is *Parseval's theorem*

$$\sigma_x^2 = \sum_j |\hat{x}(\omega_j)|^2, \quad (4.13)$$

which relates the variance to the total power in the spectrum of fluctuations. In contrast to the cross-power spectrum, the auto-power spectrum does not include any phase information. Background noise will always make a finite contribution.

The power is normally given in decibel (dB)

$$S_{\text{dB}}(f) = 10 \times \log_{10}(S(f)/S_{\text{ref}}) \quad (4.14)$$

and depicted against a logarithmic frequency axis $f = \omega/2\pi$. The reference power S_{ref} often is the maximum power in the spectrum. For the comparison of different spectra, a fixed reference value is chosen. In this double logarithmic presentation, turbulence in plasmas is indicated by a broad spectrum of, e.g., density fluctuations with a decay over a few decades according to a power law $S(f) \sim f^\alpha$. The exponent α is called *spectral index*. Although the actual physics takes place in wavenumber space, often only temporal fluctuations from single-point measurements are available. Results from frequency space can be recasted into wavenumber space under the assumption that the turbulence is frozen in the plasma flow passing a fixed spatial location and temporal fluctuations at this location can be reinterpreted as the spatial structure of the turbulence. This is known as the *Taylor hypothesis*.

4.2.3 The average cross-phase

In Sec. 2.3.5, the turbulent transport Γ is related to the spectral cross-phase between density and poloidal electric field fluctuations through Eq. (2.21). In order to account for varying cross-phases around $\varphi = \pi/2$ for drift-wave turbulence, the turbulent diffusivity is modified in Eq. (2.26) (see Sec. 2.4.2) by an average cross-phase as given in Ref. [45]

$$\cos(\varphi) = \frac{\Gamma}{\sigma_{u_r} \sigma_n} = \frac{\langle \tilde{E}_\theta(t) \tilde{n}(t) \rangle_t}{\sigma_{E_\theta} \sigma_n}, \quad (4.15)$$

where $\langle \cdot \rangle_t$ indicates temporal averaging. The subscript θ will be omitted in the following. Note that expression (4.15) is equivalent to the cross-correlation (4.6) $C_{E,n}(0)$ between electric field and density fluctuations at $\Delta t = 0$ and thus limited to $[-1, 1]$. In order to account for the statistical distribution of amplitudes and phases, the turbulent transport as given by Eq. (2.21) can be estimated in terms of the cross-power (4.9)

$$\cos(\varphi) = \frac{1}{\sigma_E \sigma_n} \sum_j H_{E,n}(\omega_j) = \frac{1}{\sigma_E \sigma_n} \sum_j h_{E,n}(\omega_j) \cos(\varphi(\omega_j)). \quad (4.16)$$

Using the cross-coherence (4.10) finally allows for a decomposition into factors, which determine the contribution to the average cross-phase:

$$\cos(\varphi) = \sum_j \gamma_j \left(\frac{S_{E,j}}{\sigma_E^2} \frac{S_{n,j}}{\sigma_n^2} \right)^{1/2} \cos(\varphi_j). \quad (4.17)$$

For simplicity, the arguments ω_j have been replaced by indices j and $h_{E,E} = S_E$ (see previous section). Recalling Parseval's theorem, this expression shows that major contributions to the cosine of the average cross-phase are due to modes, where the fraction of power in electric field and density fluctuations as well as the cross-coherence is large.

4. Data analysis

4.2.4 Bispectral analysis

The power spectrum does not allow for a distinction between modes, which are independently excited, and modes, which are non-linearly coupled. Bispectral analysis provides a tool for the investigation of non-linear quadratic three-wave interactions. The *bispectrum* of three fluctuating quantities x , y , z as given by

$$B_{x,y,z}(\omega_1, \omega_2) = \langle \hat{x}(\omega_1) \hat{y}(\omega_2) \hat{z}^*(\omega_3) \rangle \quad (4.18)$$

measures the degree of phase coherence between three modes ω_1 , ω_2 and ω_3 under the *resonance condition* $\omega_3 = \omega_1 + \omega_2$. Without a coherent phase relation between these modes, the bispectrum vanishes on the ensemble average $\langle \cdot \rangle$ similar to the cross-spectrum. A normalised version of the bispectrum is the *cross-bicoherence*

$$b_{x,y,z}^2(\omega_1, \omega_2) = \frac{|B_{x,y,z}(\omega_1, \omega_2)|^2}{\langle |\hat{x}(\omega_1) \hat{y}(\omega_2)|^2 \rangle \langle |\hat{z}(\omega_3)|^2 \rangle}. \quad (4.19)$$

It can be shown by means of the Schwarz inequality that the bicoherence is limited to $[0, 1]$. Values of one indicate that the mode at ω_3 is totally due to non-linear coupling of modes at ω_1 and ω_2 . Values of zero indicate that these modes are independently excited modes of the system and a coherent coupling is not present. Special cases of Eqs. (4.18) and (4.19) are the *auto-bispectrum* $B_{x,x,x}(\omega_1, \omega_2)$ and the *auto-bicoherence* $b_{x,x,x}^2(\omega_1, \omega_2)$, which are described in more detail in Refs. [95, 96].

In Sec. 6.1, the bispectral analysis technique is applied to fluctuations obtained from the turbulence simulation code DALF3 in order to investigate the Reynolds stress drive of zonal flows as introduced in Sec. 2.5.3. For the purpose of temporal and spatial comparisons the bicoherence (4.19) has to be simplified. This is done by integration according to

$$b^2(\omega_3) = \sum_{\omega_1, \omega_2} b^2(\omega_1, \omega_2) \delta_{\omega_1 + \omega_2, \omega_3}, \quad (4.20)$$

which gives a measure of the relative contribution of a mode at ω_3 in coherent three-mode coupling, and

$$b^2 = \sum_{\omega_3} b^2(\omega_3) \quad (4.21)$$

as a measure of the total amount of coherent three-mode coupling. A detailed study on these integrated bicoherences has been carried out in Ref. [97]. Comparative studies are carried out on the integrated auto-bicoherences $b_{n,n,n}^2$ and $b_{\phi,\phi,\phi}^2$ of density and potential fluctuations evaluated in frequency space and the integrated cross-bicoherence $b_{u^x, u^y, \Omega}^2$ evaluated in frequency and in wavenumber space. The contravariant components of the $E \times B$ velocity are calculated from

4.3 Detection of quasi-coherent structures

the potential fluctuations according to $\tilde{u}^x = -(\partial\tilde{\phi}/\partial y)$ and $\tilde{u}^y = -(\partial\tilde{\phi}/\partial x)$. In the cross-bicoherences, the zonally averaged vorticity

$$\langle\Omega\rangle_{y,s} = \left\langle \frac{\partial}{\partial x} \tilde{u}^y - \frac{\partial}{\partial y} \tilde{u}^x \right\rangle_{y,s} = \frac{\partial}{\partial x} U^y \quad (4.22)$$

is used instead of the zonally averaged potential Φ , since the energetic drive of the zonal flow is given by the zonally averaged vorticity times the zonally averaged Reynolds stress [64, 68]. Note that the term $\partial\tilde{u}^x/\partial y$ in Eq. (4.22) vanishes on the zonal average due to periodic boundary conditions and, thus, the zonally averaged vorticity is equivalent to the shear of the zonal flow U^y . The zonal-flow drive should ultimately be reflected in $b_{u^x,u^y,\Omega}^2$. The summation in Eq. (4.21) is restricted to low zonal-flow frequencies and – in wavenumber space – to the poloidal wavenumber $k_{ZF,y} = 0$.

4.3 Detection of quasi-coherent structures

In this section, analysis techniques are introduced, which are used for the detection and characterisation of propagating turbulent density structures. These techniques are applied to fluctuations of the ion-saturation current obtained from the 8×8 probe array as described in Sec. 3.2.2.

4.3.1 Correlation analyses

Correlation analyses are used for the estimation of correlation lengths and times in turbulent plasmas. For this purpose, one-dimensionally arranged probe arrays are often used. Measurements with one-dimensional, e.g., poloidal probe arrays are obscured, since the dynamics perpendicular to the probe arrangement is not detected [6]. In order to avoid artificial effects, the cross-correlation analysis technique is enhanced to a probe array arranged on a two-dimensional grid in the poloidal cross-section. For a fixed reference probe within the matrix, the cross-correlation with all 64 probes is calculated according to Eq. (4.11). The method is to calculate the Fourier transforms of the fluctuations first, multiply them in frequency space and apply the inverse Fourier transformation to get the result. Together with the FFT algorithm, the calculation can be reduced from an $O(N^2)$ to an $O(N \log_2 N)$ process, provided that the length N of each time series is a power of 2 (see e.g. [94]). This method is commonly used for the efficient numerical calculation of convolution based functions. In this work, the calculations are done with the implemented FFT algorithm of the `idl` program package.

The results for the time lag $\Delta t = 0$ are mapped onto the matrix area revealing the spatial two-dimensional structure in the poloidal cross-section. At the reference position, the highest degree of correlation will be obtained, since

4. Data analysis

the cross-correlation at this position is equivalent to the auto-correlation. In each direction, the degree of correlation characteristically decreases at increasing distance to the reference, which ultimately determines the extent of the structure. From the examination of different time lags, information on the spatio-temporal evolution of turbulent density structures is obtained. For a better understanding, the cross-correlation (4.6) at position (R_i, z_j) on the grid is written as a function of the reference position (R_k, z_l) and the time lag Δt

$$C_{i,j}(k, l, \Delta t) = \frac{\langle \tilde{n}_{k,l}(t) \tilde{n}_{i,j}(t + \Delta t) \rangle}{\sigma_{k,l} \sigma_{i,j}}. \quad (4.23)$$

The index pairs (i, j) and (k, l) are counted as shown on the left-hand side of Fig. 4.1.

4.3.2 Evaluation of space-time characteristics

In order to extract characteristic length scales from the correlation map, an ellipse is fitted to the contour line at a correlation of $C_{i,j} = 0.6$ as shown on the right-hand side of Fig. 4.1. To this end, the contour line is regarded as

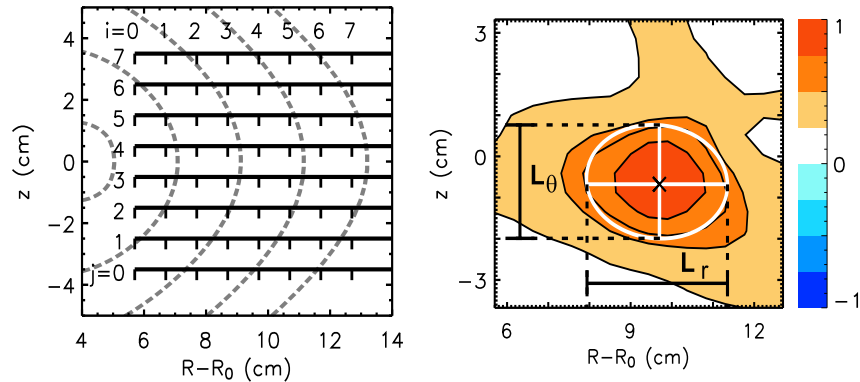


FIG. 4.1: Left: Radial and vertical probe positions in the poloidal cross-section are counted by the indices i and j , respectively. Dashed curves indicate flux surfaces up to the separatrix. Right: Correlation lengths of a density blob from $C_{i,j}$ at $\Delta t = 0$ and fixed reference position (R_k, z_l) marked by the cross (#2518). An ellipse is fitted to the contour line at $C_{i,j} = 0.6$. Correlation lengths are given by extensions of the ellipse along the vertical and horizontal lines through the reference.

the border of a homogeneous mass distribution in the (R, z) plane. Let \mathbf{T} be a 2×2 matrix similar to the inertia tensor of this mass distribution with the

4.3 Detection of quasi-coherent structures

centre of mass being at the origin:

$$T_{11} = \sum_{i,j} R_i'^2 \rho_{ij} \quad (4.24)$$

$$T_{22} = \sum_{i,j} z_j'^2 \rho_{ij} \quad (4.25)$$

$$T_{12} = T_{21} = - \sum_{i,j} R_i' z_j' \rho_{ij}, \quad (4.26)$$

where

$$\rho_{ij} = \begin{cases} 1/M, & C_{i,j} \geq 0.6 \\ 0, & C_{i,j} < 0.6. \end{cases} \quad (4.27)$$

M is the related total mass or, practically, the total number of pixels in the area with $C_{i,j} \geq 0.6$. $C_{i,j}$ is assumed to be concave in this area. Primes indicate that the coordinates have already been transformed into the centre of mass system. The sum is performed over all columns ($i = 0, \dots, 7$) and all rows ($j = 0, \dots, 7$) of the two-dimensional set of data.

The main moments of inertia and main axes are the eigenvalues and the eigenvectors of the inertia tensor, respectively. The actual moments of inertia of an elliptic disc described by

$$(x/a)^2 + (y/b)^2 = 1 \quad (4.28)$$

with given radii a and b are

$$I_x = M b^2/4 \quad \text{and} \quad I_y = M a^2/4 \quad (4.29)$$

with respect to the main axes x and y , respectively. Note that due to the definition of \mathbf{T} the moments of inertia with respect to the main axes of inertia are exchanged, so that the larger moment of inertia is automatically linked to the larger radius of the ellipse. Since in the definition of \mathbf{T} the total mass M is normalised to unity, the radii of the ellipse related to the contour line can directly be computed from the eigenvalues λ according to $r = 2\sqrt{\lambda}$. Together with the normalised eigenvectors, the ellipse is fully determined. Radial and poloidal correlation lengths L_r and L_θ are then defined by the extensions of the ellipse along horizontal and vertical lines through the reference, respectively.

For the evaluation of correlation times, the maximum correlation of the density blob is traced as a function of the time lag Δt . On the left-hand side of Fig. 4.2, the trace of the barycentre and contours of the density blob for $C_{i,j} = 0.4$ at three time lags around $\Delta t = 0$ are shown. Here, the threshold of 0.4 has been chosen for a larger temporal and thus better visual separation. For negative time lags, the structure grows on its path to $\Delta t = 0$. Here, the structure reaches its maximum size and decays again for positive Δt . The duration, in which the maximum correlation stays above a threshold of $C_{\text{th}} = 0.8$ is attributed to the correlation time τ_c as shown on the right-hand side of Fig. 4.2. Further details can be found in Sec. 5.1.

4. Data analysis

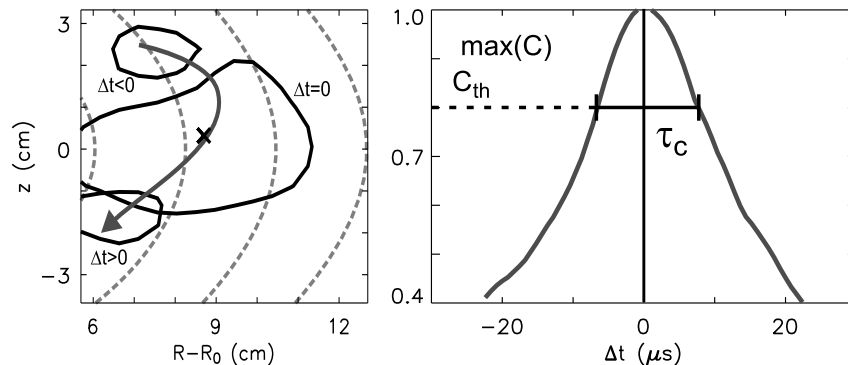


FIG. 4.2: Left: Trace of a density structure and contours of $C_{i,j} = 0.4$ for three time lags around $\Delta t = 0$ (#2535). Dashed curves indicate flux surfaces up to the separatrix. Right: The correlation time τ_c of the structure is evaluated from the temporal evolution of the maximum correlation with $\max(C) \geq C_{\text{th}}$.

4.3.3 Comparison with the conditional average technique

An alternative method for the detection of coherent structures is the *conditional averaging technique* [98, 99]. The conditional average of fluctuations \tilde{n} at the position (R_i, z_j) as a function of the reference position (R_k, z_l) and a time lag Δt is calculated according to

$$n_{i,j}^{\text{cond}}(k, l, \Delta t) = \frac{1}{N} \sum_{p=0}^{N-1} [\tilde{n}_{i,j}(t_p + \Delta t) | (\tilde{n}_{k,l}(t_p) = n_c) \wedge \tilde{n}'_{k,l}(t_p) > 0]. \quad (4.30)$$

In other words, n^{cond} is an average over N sub-series of length τ collected from time series in $[t_p - \tau/2, t_p + \tau/2]$ around a point in time t_p , where in the reference signal a condition is met. As a result, the function n^{cond} reflects the coherent part of the signal, whereas the incoherent part, i.e., the ambient turbulence, vanishes with increasing number of averages. In Ref. [25], this technique has been used for the detection of quasi-coherent structures in TJ-K. As discussed in Ref. [100], correlation functions systematically overestimate the temporal width of fluctuations, whereas deviations of the shapes of fluctuations in the sub-series might non-systematically lead to a smearing-out effect of the conditional averaging result (see also Ref. [99]).

For large-scale coherent structures, both methods are expected to give the same results. This is not necessarily always the case. In general, it is recommended to apply both methods and decide, which one is more reliable. For this purpose, the conditional averaging technique is applied to the data similar to the cross-correlation technique. The trigger condition is $n_c = 2\sigma$ at a rising flank. For best comparability, each time series is normalised according to $\tilde{n} = \tilde{n}_0/\sigma$. Due to the trigger condition at the rising flank, the maximum value of the conditional average at the reference possess a systematic offset in Δt with respect to $\Delta t = 0$. Hence, all calculated conditional averages on the

4.3 Detection of quasi-coherent structures

grid are corrected by this offset and normalised with the maximum value at the reference.

For both methods, the correlation lengths and correlation times are compared in Figs. 4.3 and 4.4, respectively. The results are shown for the same

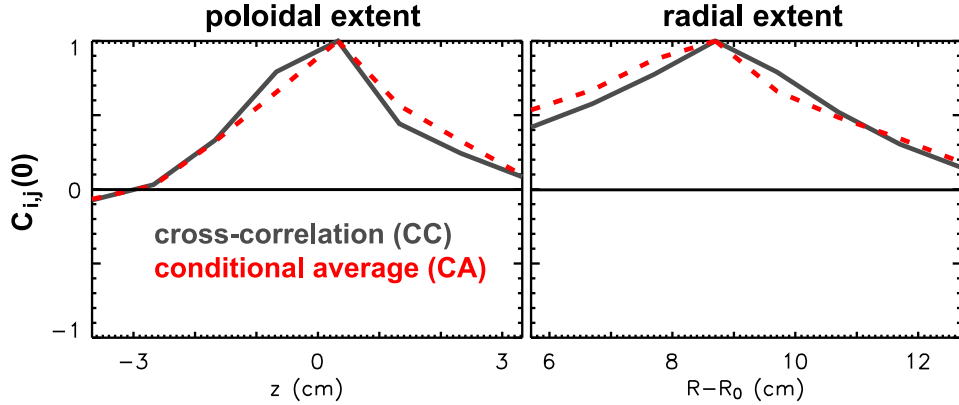


FIG. 4.3: Comparison of poloidal (left) and radial (right) extents of the structure shown in Fig. 4.2 as calculated with the cross-correlation technique (solid line) and the conditional averaging technique (dashed line). For both techniques, the extents are in good agreement.

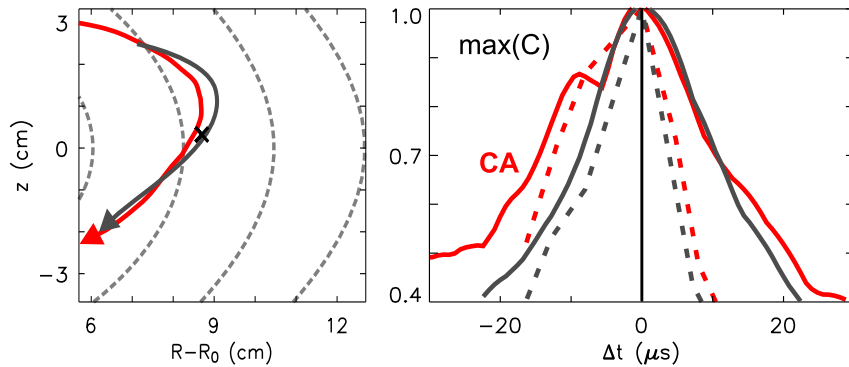


FIG. 4.4: Trace (left) and correlation time (right) as depicted in Fig. 4.2. Results from the conditional averaging (red curves) and the cross-correlation (gray curves) are compared. Dashed curves show the results from the methods applied to a single (one-dimensional) probe column through the reference. For both methods, the traces are similar. In detail, the temporal evolutions of the maximum values deviate from each other. Correlation times are underestimated, when one-dimensional probe arrays are used.

data as in Fig. 4.2. In comparison, the spatial dimensions obtained by both methods are in good agreement. The traces of the density blob are rather similar. Differences occur for the correlation times. As can be seen on the right-hand side of Fig. 4.4, the maximum value of the conditional average as a function of the time lag is broader than that of the cross-correlation. For

4. Data analysis

negative time lags between $-20 \mu\text{s}$ and $-10 \mu\text{s}$, the conditional average looks like a part of the cross-correlation shifted towards more negative Δt giving the impression of a separated structure of the same shape running after. It is reasonable to assume that the separated flanks belong to the same structure and that in many (but not most) cases, when the trigger condition is met at the reference, the actual velocity of the structure is smaller than in most cases. This would be a prime example for the smearing-out effect due to a varying propagation velocity of the structure as discussed in Ref. [99].

These findings have been compared to a couple of other discharges, which are not shown here. For both methods, the structure sizes are generally in good agreement. The qualitative traces of the structure are equally well described by both methods. Quantitatively, the temporal evolution of the maximum value of the conditional average has been found to deviate irregularly from that of the maximum cross-correlation. This could be attributed to the irregularity of the smearing-out effect of the conditional average. Hence, it is reasonable to assume that the cross-correlation technique yields a more robust estimate of correlation times.

In order to demonstrate the artificial effects arising from one-dimensional probe arrays, the correlation time as evaluated from a single probe column through the reference is shown on the right-hand side of Fig. 4.4 (dashed curves). Here, the correlation times are underestimated, since the density blob has a radial velocity component and does not stay in the range of the single probe column.

Characteristics and scaling properties of turbulent structures

The energy confinement time τ_E is a key parameter in nuclear fusion research. Long confinement times are required for an economic power production. In order to predict the confinement times of future devices, the scaling properties of τ_E is investigated. The most important scaling parameter is $\rho_s = \sqrt{M_i T_e}/(eB)$. Due to the high magnetic field in a fusion reactor, it will be much smaller than in present-day devices. The scaling can be regarded as a consequence of the single scaling properties of correlation lengths (L_c) and correlation times (τ_c) of turbulent structures. Both parameters determine a diffusion coefficient ($D \sim L_c^2/\tau_c$), which describes the confinement quality in terms of microscopic diffusive random walk processes of particles. However, most scaling studies are carried out on global energy confinement times τ_E or deduced diffusivities $\chi \sim 1/\tau_E$. In the following, scaling properties are investigated directly on spatial and temporal characteristics of turbulent structures, which are measured with an 8×8 array of Langmuir probes introduced in Sec. 3.2.2. Correlation lengths and times are gained from correlation analyses carried out on the data obtained from the probe array as explained in Sec. 4.3. The results have been published in Refs. [101, 102].

5.1 Experimental details

The probe matrix introduced in Sec. 3.2.2 is centred on a variable radial position ranging from $R - R_0 = 9$ to 13 cm in the region of steepest density gradients and highest fluctuation levels. The signal at each probe of the matrix consists of 512k values sampled at a frequency of $f = 1.25$ MHz. For the cross-correlation analyses the signals are digitally bandpass filtered in a range $3 \text{ kHz} \leq f \leq 300 \text{ kHz}$. Reliable results are obtained only if the structure dimensions are covered by the matrix.

The trajectory, the correlation lengths as well as the correlation times depend on the position of the reference probe. Therefore these quantities have been calculated for all reference positions (k, l) within the matrix (see Fig. 4.1).

5. Characteristics and scaling properties of turbulent structures

The objective was to compare these quantities to the local values of the drift-scale ρ_s , the perpendicular gradient length $L_n = n_e/\nabla_r n_e$ and the dimensionless plasma- β $\beta^* \sim n_e T_e / (L_n B)^2$ and collisionality $\nu^* \sim \nu_{ei} L_n / c_s$. These data were all derived as radial profiles at $z = 0$ from swept Langmuir probe data. In order to obtain radial profiles of the correlation parameters, results from the adjacent reference points in z direction ($l = 2-5$) have been averaged. For L_θ and L_r this could be reasonably done for the radial positions $k = 2-5$. This results in averaged quantities of the form $L(k) = \sum_{l=2}^5 L(k, l)$. The correlation times have been averaged between $l = 3, 4$. The choice of the reference position was such that the structure fits into the matrix. Additionally, by an adequate choice of the correlation threshold it is guaranteed that (i) only one structure is detected in the matrix area at a time, (ii) the contours fit inside the matrix and (iii) that they appear and vanish within the matrix area.

For the investigation of the scaling, the radial dependence of all quantities are taken into account. The drift-scale ρ_s is derived from radial T_e profiles and the local magnetic field strength B . Since B is rather limited due to the resonance condition of ECRH, ρ_s is mainly varied through the ion mass number of the working gases ranging from 1 to 40. For each gas, data were taken from discharges at two values of the neutral gas pressure (2 and 5×10^{-5} mbar), two of the effective heating powers (0.9 and 1.8 kW) and two of the magnetic field strengths (72 and 89 mT). Additionally, the matrix was set up on two radial positions, such that turbulent structures could be detected in a radial range of $R - R_0 = 7-14$ cm. Altogether, 220 sets of data have been collected in a data base.

It has been checked that the matrix does not substantially alter the plasma conditions. For an hydrogen discharge, this is shown in Fig. 5.1, where density profiles are compared for the cases without the matrix (circles) and with the matrix (dots) set up as shown on the left-hand side of Fig. 4.1. The comparison shows a good agreement, and a perturbation due to the probe array is not observed.

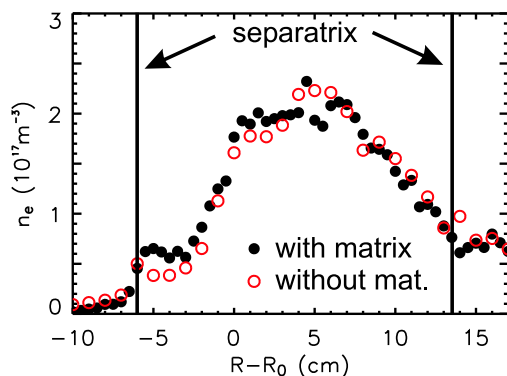


FIG. 5.1: Density profile for hydrogen discharges with matrix (dots, #2786) and without matrix (circles, #2751).

5.2 Space-time structure

All discharges feature a turbulent, i.e., broad power spectrum decaying over several decades above 10 kHz according to a power law. The spectra shown in Fig. 5.2 were measured with a tip of the probe array corresponding to $i = j = 4$ in Fig. 4.1. Except for helium, the spectra shift to lower frequencies

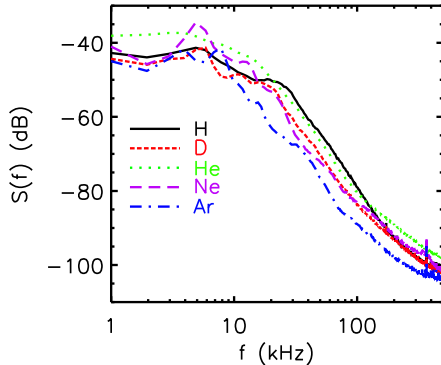


FIG. 5.2: Power spectra of fluctuations in the ion-saturation current for each gas calculated from data obtained by the probe array.

with increasing ion mass, which is consistent with an increasing structure size as indicated in Fig. 7 of Ref. [103]. Furthermore, quasi-coherent modes are indicated by peaks below 10 kHz. Especially for neon, a large mode is present. The helium spectrum, on the other hand, is very smooth.

In all discharges, radially and poloidally localised density structures have been detected with radial and poloidal correlation lengths L_r and L_θ ranging from 2 to 8 cm. The comparison of both correlation lengths in Fig. 5.3 shows

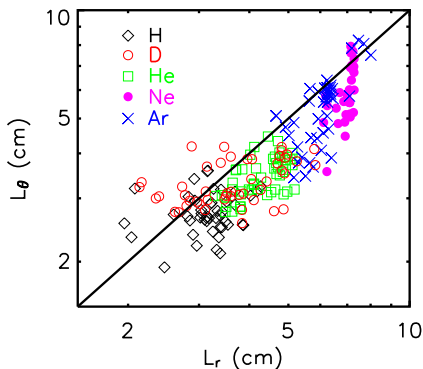


FIG. 5.3: Correlation lengths L_θ (L_r) for the gases hydrogen, deuterium, helium, neon and argon in a log-log plot. The straight line depicts $L_\theta = L_r$.

that the radial and the poloidal structure sizes are approximately equal and both increase with ion mass. With the exception of deuterium the different gases are well separated. Deuterium is localised between hydrogen and helium, but the scatter is large. The radial correlation lengths in neon discharges are found to be larger than in argon and they partly exceed the matrix. Spectroscopic measurements on argon plasmas, however, showed that the ions are single charged [82]. The poloidal correlation lengths are in a similar range.

5. Characteristics and scaling properties of turbulent structures

The structures are slightly elongated with $L_r \gtrsim L_\theta$. Only at the largest scales, where L_r is limited by the plasma radius, the structures become symmetric.

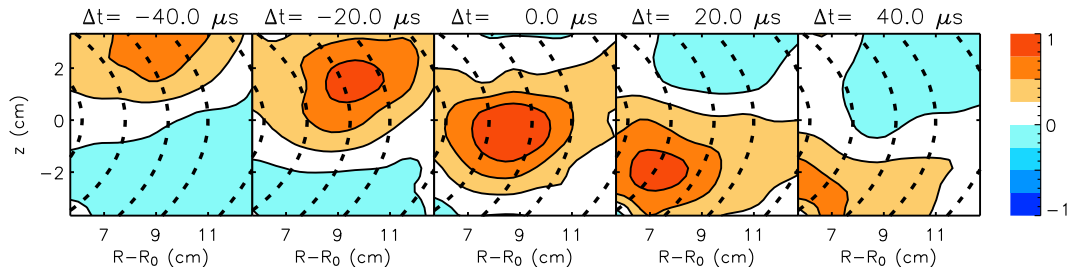


FIG. 5.4: Spatio-temporal evolution of a density blob in a helium discharge (#2532) as a result of correlation analyses of ion-saturation-current fluctuations within the probe matrix. The reference probe was at $(i, j) = (3, 3)$. From left to right the time delay Δt between the probes and the reference was varied from -40 to $40 \mu\text{s}$. Flux surfaces up to the separatrix are depicted as dashed lines.

The spatio-temporal evolution of a density structure in a helium discharge is illustrated in Fig. 5.4. In general, the density structures propagate poloidally in the direction of the electron-diamagnetic drift as it is consistent with drift-wave turbulence. In special cases, structures were observed, which do not propagate or propagate in the opposite direction. This is a consequence of flat pressure profiles, where the $E \times B$ drift compensates the electron-diamagnetic drift or dominates the poloidal flow (see Fig. 3.6). In particular, this is the case, when the neutral gas pressure in TJ-K is high.

5.3 Scaling of characteristic turbulence properties

For the investigation of the theoretically motivated scaling properties of L_r and L_θ with ρ_s and τ_c with a/c_s , all data points, for which the drift-ordering constraint (see Sec. 2.2.2) does not hold – i.e. all points with $\rho_s \gtrsim L_n$ – have been omitted. Thus the contribution of argon, which has relatively large drift-scales in comparison to the gradient length, is reduced drastically. In the following, the analyses are carried out for three datasets: (i) hydrogen and deuterium only, (ii) also helium included and (iii) all gases.

5.3.1 Scaling of correlation lengths

In Fig. 5.5, the ρ_s scaling of L_r and L_θ is studied in a log-log plot. For the radial correlation length a power law according to $L_r \sim \rho_s^{b_r}$ with $b_r^{\text{all}} = 0.42 \pm 0.04$ is obtained from a regression of all gases. The correlation between L_r and ρ_s is 82%. For the reduced datasets, the coefficients are $b_r^{\text{HDHe}} = 0.44 \pm 0.08$ at 77% and $b_r^{\text{HD}} = 0.78 \pm 0.14$ at a correlation of 84%.

5.3 Scaling of characteristic turbulence properties

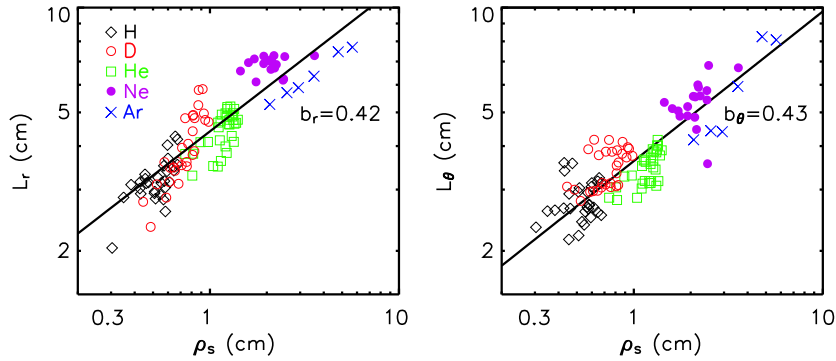


FIG. 5.5: Scalings of the radial (left) and poloidal (right) correlation length with ρ_s . $L_{r,\theta} \sim \rho_s^{b_{r,\theta}}$ with $b_r = 0.42$ and $b_\theta = 0.43$ has been fitted to the data (solid line).

The scaling of the poloidal correlation length is comparable to that of L_r if all gases are included in the analysis. A regression yields a scaling with $b_\theta^{\text{all}} = 0.43 \pm 0.04$ (at 88% correlation) as shown on the right-hand side of Fig. 5.5. This result agrees well with the result of a previous study, where the poloidal correlation length has been evaluated from measurements with a poloidal probe array and a scaling in the range $L_\theta \sim \rho_s^{1/3-1/2}$ was found. These experiments also included data from helicon-heated discharges, which are at higher B and n . For details see Ref. [25]. Without neon and argon, the correlation between L_θ and ρ_s decreases to 57% and the dependence on ρ_s becomes weaker ($b_\theta^{\text{HDHe}} = 0.24 \pm 0.07$). Without helium, the correlation increases again to 62%. A scaling with $b_\theta^{\text{HD}} = 0.42 \pm 0.15$ is obtained.

Under the similarity constraint (see Sec. 2.4.1) the parameters β^* , ν^* and L_n should have been constant for this kind of investigation. Actually for the present data, they widely scatter around $\beta^* \approx 0.1$, $\nu^* \approx 1$ and $L_n \approx 6$ cm. This spreading is mainly due to the neon and the argon data. Without these gases, the deviations could be reduced to approximately 60%. A regression analysis, however, did not reveal a significant dependence of the correlation lengths on these parameters. For the sub-sets the correlation of L_r and L_θ with these parameters is less than 30%. For the dataset including all gases a stronger correlation of up to 60% is obtained. This is relatively large, but on the other hand, a significant correlation of ρ_s with β^* , ν^* and L_n is not found. Hence, hidden dependencies on these parameters should not alter the dependencies of the correlation lengths on ρ_s .

5.3.2 Scaling of structure lifetimes

Fig. 5.6 depicts the dependence of the correlation time τ_c on a/c_s for the data restricted to the drift-ordering constraint. A systematic dependence of τ_c on the radially resolved electron temperature is not observed. τ_c rather shows a large scatter for each ion mass with the exception of helium. For helium,

5. Characteristics and scaling properties of turbulent structures

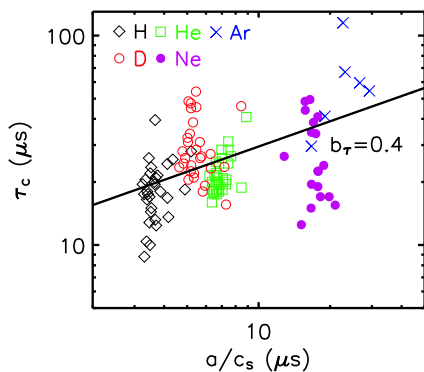


FIG. 5.6: Scaling of τ_c with a/c_s . A scaling according to $\tau_c \sim (a/c_s)^{b_\tau}$ is evaluated with $b_\tau = 0.4$ for all gases (solid line).

the correlation times are apparently smaller than for deuterium. Also for neon, comparably small correlation times are observed. Nevertheless, there is a general trend with the ion mass towards longer correlation times. They range from $10 \mu\text{s}$ in hydrogen to $100 \mu\text{s}$ in argon. Due to the large scatter, the correlation between τ_c and a/c_s is in general low ($<50\%$). With $\tau_c \sim (a/c_s)^{b_\tau}$ a scaling according to $b_\tau^{\text{all}} = 0.4 \pm 0.14$ is found for all gases (solid line in Fig. 5.6). Without neon and argon the scaling is $b_\tau^{\text{HDHe}} = 0.33 \pm 0.27$ and for hydrogen and deuterium only, it is close to linear with $b_\tau^{\text{HD}} = 0.8 \pm 0.36$. A significant dependence of τ_c on the parameters β^* , ν^* and L_n is not observed. The correlation with these parameters is less than 40% .

5.3.3 Scaling of the Turbulent diffusivity

A simple expression for the turbulent diffusivity is constructed out of the random walk model according to $D = L_r^2/\tau_c$ (see Sec. 2.4.2). Theory predicts that for drift-wave turbulence the normalised diffusivity $D^* = D/D_B$ – where $D_B = \rho_s c_s$ is the Bohm diffusion coefficient – should scale linear with ρ_s (see Sec. 2.4.2). Since the scalings of $L_r \sim \rho_s^{b_r}$ and $\tau_c \sim c_s^{-b_\tau}$ are known, the scaling of D^* can be calculated as $\rho_s^{2b_r-1} c_s^{b_\tau-1}$. If the c_s dependence is disregarded, the scaling with ρ_s only can be determined as done in Fig. 5.7. Depicted are mean values and error bars for each ion mass as deduced from the data for L_r and τ_c shown in Fig. 5.5 and 5.6, respectively. With the exception of argon, D^* increases with the ion mass. For the present data, D^* turns out to scale as $D^* \sim \rho_s^{b_D^*}$ with $b_D^{\text{all}} = 0.49 \pm 0.2$, i.e., weaker than gyro-Bohm-like (see Sec. 2.4.1) as could have been expected from the scalings of L_r and τ_c alone. The reduced data reveals a scaling with $b_D^{\text{HDHe}} = 0.38 \pm 0.13$. The results $b_\tau^{\text{HD}} = 0.78 \pm 0.14$ and $b_\tau^{\text{HD}} = 0.8 \pm 0.36$ suggest that hydrogen and deuterium favour a gyro-Bohm-like scaling. However, these results are not supported by Fig. 5.7 (left), which shows that the difference in D^* between hydrogen and deuterium is marginal. A regression yields $b_D^{\text{HD}} = 0.16 \pm 0.25$.

The absolute values of the diffusivity turn out to be rather large with respect to values for the edge of fusion plasmas, which are typically in the range

5.3 Scaling of characteristic turbulence properties

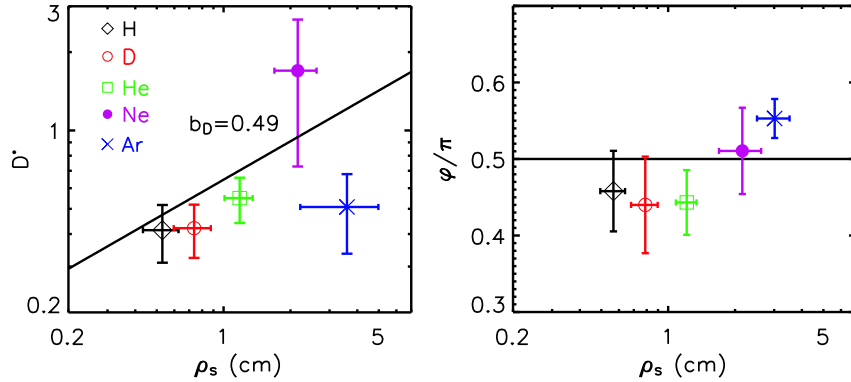


FIG. 5.7: Scaling of the ratio $D^* = D/D_B$ with ρ_s (left). The scaling according to $D^* \sim \rho_s^{b_D}$ with $b_D = 0.49$ is depicted by the solid line. Right: Cross-phase between poloidal electrical field and density fluctuations.

0.1–1 m²/s [104, 105]. For all ion masses except for neon it is $D^* \approx 0.4$ and the values of D are in the range 20–200 m²/s. For neon, D^* is a factor of 5 higher, which is due to larger L_r and smaller τ_c . In order to compare the absolute values with those of a fusion plasma, the diffusivity can be rescaled using, e.g., the ISS95 scaling expression (2.23) and the relation $\tau \approx a^2/4D$. Although the ISS95 expression is for the energy confinement time, it can be assumed that particle confinement times τ scale similarly. The ratio of the ISS95 confinement times between discharges at typical parameters for TJ-K and, e.g., W7-AS discharges is $\tau^{\text{TJK}}/\tau^{\text{W7AS}} \approx 1/35$. Since the minor radius of W7-AS is twice that of TJ-K, the equivalent diffusivity would be $D^{\text{W7AS}} \approx 0.1 D^{\text{TJK}} \approx 2$ –20 m²/s. This is still a large number.

In this context, the cross-phase φ between density fluctuations (\tilde{n}) and poloidal electric field fluctuations (\tilde{E}_θ) is examined. As discussed in Sec. 2.3.5, the cross-phase is an important quantity for turbulent transport. For drift-waves, $\varphi \approx \pi/2$ is expected as it has already been confirmed for TJ-K [25]. The cross-phase modifies the diffusivity drastically; for $\varphi = \pi/2$ the diffusivity would be zero. In addition, the cross-phase can also depend on ρ_s . While Eq. (2.25) is only valid for constant φ , Eq. (2.26) has to be used if φ changes. This also alters the scaling of the resulting diffusivity. For some of the data, radial profiles of the fluctuations are available from measurements with the transport probe (see Sec. 3.2.2). In Fig. 5.7 (right) the cross-phases calculated from Eq. (4.15) are depicted versus ρ_s . All phases reside near $\pi/2$ as it is characteristic for drift-waves. For small ion masses, the phases are smaller than $\pi/2$, which leads to transport down the density gradient. Deuterium and helium show similar phases, whereas that of hydrogen is slightly closer to $\pi/2$. For large ion masses, the phases are $\pi/2$ (neon) or greater than $\pi/2$ (argon). The phases for neon could indicate the presence of a linear stable drift-mode and explain the dominant mode found in the power spectra shown in Fig. 5.2. For argon, the phases are clearly larger than $\pi/2$, which points to the stabilisation of dominant drift-modes.

5. Characteristics and scaling properties of turbulent structures

Including the cross-phases according to $D_\varphi = D \cos(\varphi)$ (Eq. (2.26)) in the scaling for the lightest ions, the dependence on ρ_s becomes stronger with $b_D^{\text{HDHe}} = 0.63 \pm 0.13$. For hydrogen and deuterium alone, a close to gyro-Bohm scaling is found: $b_D^{\text{HD}} = 0.7 \pm 0.3$. Interestingly, a Bohm-like scaling of $|D_\varphi^*|$ with $b_D^{\text{all}} \approx 0.1$ is obtained, if large ion masses are included, for which the structure sizes are comparable to the system size.

A more important change occurs to the absolute value of the diffusion coefficient. Including the cross-phase correction according to Eq. (2.26) reduces the diffusivity by another factor of about 10. Together with the rescaling to fusion plasma dimensions, the equivalent diffusivity is now in the range 0.2–2 m²/s. Taking into account that all data have been measured in the low-field region of the plasma, where the largest amplitudes are observed, one could argue that a flux-surface averaged diffusivity would be still smaller. Hence, the value of the diffusivity is in reasonable agreement with values found in the edge of fusion plasmas.

5.4 Discussion and conclusions

Radial and poloidal correlation lengths and correlation times of propagating density structures have been measured in a toroidal low-temperature plasma by means of a 8×8 Langmuir probe matrix, which was shown not to perturb the plasma. In hydrogen, deuterium, helium, neon and argon discharges, the density structures show correlation lengths in the range 2 to 8 cm and correlation times in the range 10 to 100 μ s in tendentially increasing order with the ion mass. For neon and argon, the structure sizes approach the system size given by the minor plasma radius and the radial correlation length for neon is even somewhat larger than that for argon. Except for helium, the turbulent spectra also exhibit signatures of quasi-coherent modes in a range below 10 kHz. These modes, which are most distinctive for neon, have been analysed in the correlation study.

The scaling properties of the characteristic length and time scales L_r and τ_c have been studied. Drift-wave turbulence predicts linear scalings of L_r with the drift-scale ρ_s and of τ_c with a/c_s , which results in a gyro-Bohm scaling of the diffusivity D . Most studies of the confinement scaling with ρ_s are carried out on confinement times or the diffusivities. The scalings of these quantities are, however, a consequence of the microscopic scalings under the assumption of simple mixing-length estimates. Regression analyses of a large database showed different scalings for different regions of ρ_s . The variation of ρ_s by a factor of 10 is mainly due to the ion mass. The smaller part of the variation is due to the fact that correlation parameters have been evaluated at different radial positions and that the local electron temperature was used to calculate ρ_s . The results are summarised in Tab. 5.1. As a general trend, the correlation lengths L_r and L_θ show a power law scaling ρ_s^b in the range $b = 0.3$ – 0.5 . This is

5.4 Discussion and conclusions

	all	H, D, He	H, D
L_r	0.42 ± 0.04	0.44 ± 0.08	0.78 ± 0.14
L_θ	0.43 ± 0.04	0.24 ± 0.07	0.42 ± 0.15
τ_c	0.40 ± 0.14	0.33 ± 0.27	0.80 ± 0.36
D^*	0.49 ± 0.20	0.38 ± 0.13	0.16 ± 0.25

TABLE 5.1: Scalings of L_r , L_θ and D^* with ρ_s and of τ_c with a/c_s for different regions of the ion mass.

consistent with previous studies, in which the scaling of L_θ has been evaluated from measurements with a poloidal probe array [25]. The correlation time τ_c scales as $(a/c_s)^{0.4}$. In order to classify the present scaling type, a dimensionless turbulent diffusion parameter $D^* = D/D_B$ has been calculated, for which theory predicts a gyro-Bohm-like scaling, i.e., $D^* \sim \rho_s/a$. As expected from the scalings of L_r and τ_c , a weaker than gyro-Bohm-like scaling of $D^* \sim \sqrt{\rho_s}$ is found.

For small ρ_s , represented by hydrogen and deuterium plasmas, scalings of $L_r \sim \rho_s^{0.8}$ and $\tau_c \sim (a/c_s)^{0.8}$ are close to the predicted linear ones. Nevertheless, the scaling of the dimensionless diffusivity turns out to be in-between Bohm- and gyro-Bohm. This is due to a residual c_s dependence of D^* , which modifies the scaling due to a correlation between c_s and ρ_s . Including larger ions in the analysis leads to successively weaker scalings. It might be argued that the weaker scaling is a consequence of the structure sizes of density blobs in neon and argon discharges being comparable to the system size, i.e., a contribution of macroscopic turbulence shifts the scaling to near Bohm-like. Helium is somewhat different from hydrogen and deuterium since it does not show signs of quasi-coherent modes. The discharges are not dimensionally similar, since the other relevant parameters ν^* , β^* and L_n are not constant. Scaling studies, did, however, not reveal a significant dependence of the correlation lengths and times on these parameters. The sensitivity of D^* to other parameters than ρ_s demonstrates that the scaling studies carried out on diffusivities have to be interpreted with caution and the scalings of the microscopic parameters should be preferred. It must be stressed that in the present case τ_c shows a large scatter and should also be interpreted with caution. A significant dependence of τ_c on the local electron temperature is not found. Thus, the results related to the variation of the ion mass are regarded as more meaningful.

It was also shown that the cross-phase between poloidal electric field and density fluctuations strongly modifies the simple mixing length expression (2.25) with respect to scaling and absolute values. This is at least the case, if drift-waves with $\varphi \approx \pi/2$ dominate the turbulence and the cross-phase varies with ρ_s as found in the present experiment. The cross-phases are consistent with results of previous studies [25]. From theory, there is no clear prediction of the scaling of the cross-phase with ρ_s . For light ions, the experimental phases

5. Characteristics and scaling properties of turbulent structures

were found to be smaller than $\pi/2$ resulting in outward-directed transport. For neon, the phase was $\pi/2$, which suggests that a linear stable drift-mode can exist and might be the cause for the prominent peak in the neon spectrum. For argon, the phase was larger than $\pi/2$. This indicates a stabilisation of dominant drift-modes, which could be a possible explanation for the observation that the radial correlation length in argon is smaller than that in neon although ρ_s is larger.

In all gases, the cross-phases are drift-wave-like with $\varphi \approx \pi/2$. Hence, a gyro-Bohm-like scaling would have been expected. However, the scaling is rather Bohm-like if heavier ions are included in the analyses. In first instance, this might not be surprising, since the contribution of large-scale structures, whose size are comparable to the system size, could shift the scaling to more Bohm-like. The origin, however, could be due to three-dimensional effects concerning the topology of the magnetic field. As typical for devices of the stellarator family, the topology in TJ-K is rather complex. Compared to the geometry in tokamak devices, TJ-K possess a six-fold symmetry of the magnetic field in toroidal direction. Particles can be trapped within the magnetic ripple and directly lost. As discussed in Ref. [30], especially direct losses of electrons could be an explanation for the positive radial electric field observed in the confinement region of TJ-K. The electric field reverses beyond the separatrix, where field lines end on the vacuum vessel and the electrons, which possess a higher parallel mobility than the ions, can flow off. The reversal of the radial electric field describes a pronounced $E \times B$ shear layer at the separatrix with increasing shearing rates at increasing ion mass (see also Fig. 3.6). It might be possible that for higher ion masses like in neon and argon these poloidal $E \times B$ shear flows could affect the shape of the structures or even the cross-phases and, hence, corresponding scalings. Strong shear flows are expected to result in a decorrelation of large scales, which would be an explanation of the structures in argon being smaller than in neon. This will not be confirmed in the next chapter, where the influence of natural static and spontaneously excited shear flows on turbulence characteristics in TJ-K is addressed.

A decrease of the cross-phase is observed from hydrogen to deuterium, which turns the Bohm-like scaling of D^* to a gyro-Bohm-like one of the cross-phase corrected dimensionless diffusivity D_φ^* . For all ions included, the scaling of D_φ^* remains Bohm-like. Absolute values of the turbulent diffusivity are consistent with those measured in the edge of fusion plasmas. If the cross-phase is included according to Eq. (2.26) and the result is re-scaled to fusion parameters using a scaling for global confinement times, equivalent values for the diffusivity in the range of 0.2–2.0 m²/s are found. In the present work, the stellarator device W7-AS has been used as a reference. It must be stressed that equivalent cross-phases between poloidal electric field and density fluctuations in the edge region of W7-AS have been found to tend to be close to $\varphi \approx 0$ [6]. This is a strong contrast to the cross-phases found in TJ-K. It was demonstrated that the comparison of diffusivities in both devices is possible if the cross-phase is

included. This might restrict a general comparability to discharges not only possessing the same dimensionless parameters but also exhibiting a similar dynamics, for which the cross-phase could be a key parameter.

In conclusion, the dimensionless diffusivity based on the simple mixing length expression (2.25) did not turn out to be an adequate quantity for the investigations of scaling properties. It is rather sensitive to residual dependencies on other parameters than ρ_s and should be interpreted with caution. More reliable results are obtained, if the basic turbulent properties L_r and τ_c are regarded. Hydrogen and deuterium, which are practically identical in terms of atomic physics, are consistent with the predicted linear scaling for the turbulent properties L_r and τ_c . Heavier ions tend more to a global Bohm-like scaling. The cross-phase between poloidal electric field and density fluctuations substantially modifies the diffusivity and its scaling. Including the cross-phase, the value of the diffusivity is consistent with results from fusion plasmas.

5. Characteristics and scaling properties of turbulent structures

Natural shear flows in TJ-K

Turbulent structures can be affected by poloidal $E \times B$ shear flows, which are supposed to limit the radial correlation length via the shear decorrelation mechanism and thus reduce turbulent transport (see Sec. 2.5). This process is important for the achievement of transport barriers in fusion plasmas. Spontaneously excited zonal flows and the natural shear layer in TJ-K are discussed as possible candidates for affecting the microscopic turbulent characteristic length and time scales and their scaling properties. In a study on simulated data, the effect of temporally varying shear flows on turbulent transport is investigated. In toroidal geometry, these flows appear in the form of geodesic acoustic modes (GAM), which result from poloidal pressure asymmetries induced by poloidal $E \times B$ rotation, in particular, by zonal flows (ZF). Zonal flows are supposed to be driven by Reynolds stress (RS). On the basis of small-scale drift-waves nonlinearly coupling into the large-scale ZF, different bispectral quantities have been predicted to be related to the RS drive. In the following, the RS drive of ZFs is studied using these quantities. Their applicability as a diagnostic of ZF drive is investigated. At the end of this chapter, natural $E \times B$ shear flows in TJ-K are studied.

6.1 Effect and drive of zonal flows

ZFs are investigated on data obtained from the turbulence simulation code DALF3 (see Sec. 2.2.2) with respect to their effect on turbulent transport and their RS drive (see Sec. 2.5.3). The results are presented in physical units with respect to $L_{\perp} = 5$ cm and geometrical parameters of TJ-K as presented in Refs. [24, 32], offering the possibility of direct comparison with experimental results. Simulated data for various values of β^* and ν^* , which basically belong to the drift wave regime [24], were analysed to detect ZFs. The other parameters entering the code are $\mu^* = 1.1$ and $\epsilon_s = (qR/L_{\perp})^2 = 2025$. With $L_{\perp} = 5$ cm this refers to hydrogen gas. In the following, the results are presented for a simulation run with $\beta^* = 0.7$ and $\nu^* = 4.0$. For the calculation of averages in s direction only two planes were used: one at the magnetic low-field side and one at the high-field side. The results have been published in

6. Natural shear flows in TJ-K

Ref. [106].

6.1.1 Analysis of zonal flows

The mean flow has only a y -component, found from the flux surface averaged (over y and s) potential fluctuations $\Phi = \langle \tilde{\phi} \rangle_{y,s}$ according to $U^y = (\partial\Phi/\partial x)$. The flux surface averaged turbulent transport is $\Gamma^x = \langle \tilde{n}_e \tilde{u}^x \rangle$. Fig. 6.1 shows contour profiles of the average poloidal flow U^y and the radial transport Γ^x calculated from a simulation run with $\beta^* = 0.7$ and $\nu^* = 4.0$.

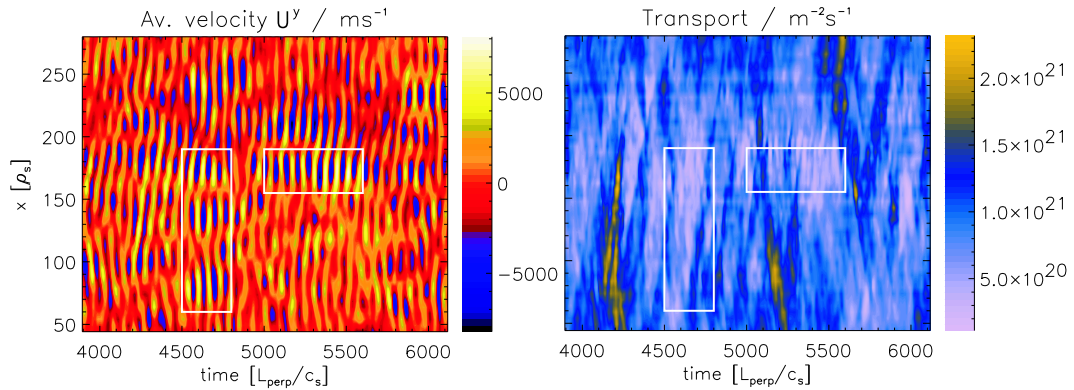


FIG. 6.1: (t, x) -profiles of average poloidal flow (left) and radial transport (right). The dominant flow oscillations are due to GAMs. Regions with highest values of U^y are marked by boxes. They are characterised by highest contrast. Transport minima are found in the vicinity of these flow maxima.

The most apparent feature is a periodic oscillation in the entire radial range. To examine these oscillation, an arbitrary segment of a time trace at a fixed position x is shown in Fig. 6.2 (left). It turns out that the characteristic frequency of the oscillation is approximately consistent with $f \approx 0.015 c_s/L_{\perp}$. It appears as a peak in the frequency spectrum of U^y shown in Fig. 6.2 (right). The spectrum was obtained by averaging the spectra of all time traces in the radial range shown in Fig. 6.1 (left). The frequency agrees rather well with the prediction for GAMs [67] (see also Sec. 2.5.4), which is given by $\omega_{\text{GAM}} = \sqrt{2} c_s/R_0 = \omega_B c_s/(\sqrt{2} L_{\perp})$, where $\omega_B = 2L_{\perp}/R_0$. For the parameters used this yields $f_{\text{GAM}} = 0.0146 c_s/L_{\perp}$. The low frequency ZF appears as a smaller peak in the averaged spectrum. Further simulation runs with $\nu^* = 1.0 - 6.0$ holding $\beta^* = 0.7$ fixed and with $\beta^* = 0.7 - 2.25$ holding $\nu^* = 4.0$ fixed have been analysed as well. In all cases a peak of the mean poloidal flow at the GAM frequency of $f \approx 0.015 c_s/L_{\perp}$ was present. As expected for GAMs, the frequency scales with c_s/R_0 and not with β^* or ν^* . The relative amplitude of the low frequency ZF and the GAM changes with time and location. But in all cases the GAM peak is at least of similar magnitude as the low frequency

6.1 Effect and drive of zonal flows

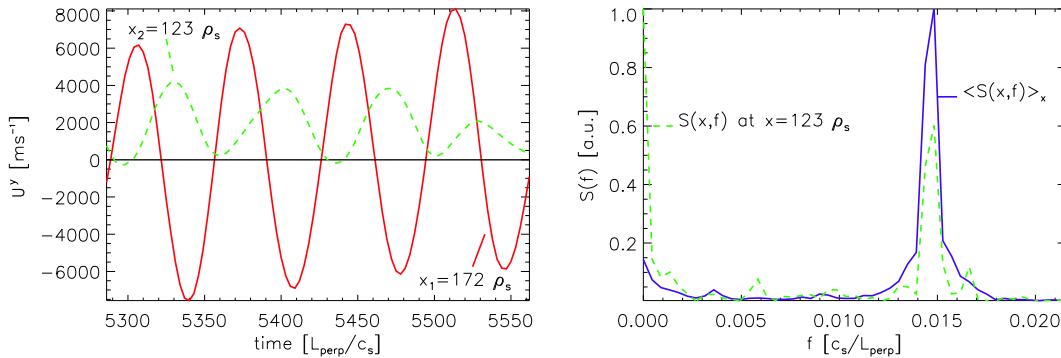


FIG. 6.2: Segment of a time trace of U^y from Fig. 6.1 at fixed positions $x_{1,2}$ (left). The solid line belongs to a region with high values of U^y (x_1) and the dashed to a region with lower values (x_2). The oscillation has a period of $T \approx 70 L_{\perp}/c_s$ reflected in the auto-power spectrum of U^y (right) by a peak at $f \approx 0.015 c_s/L_{\perp}$. Also a smaller peak at zero frequency is visible. For comparison another spectrum at fixed x is shown.

peak. For comparison, another spectrum at a fixed position x is also shown on the right-hand side of Fig. 6.2.

In regard to the shear decorrelation mechanism as introduced in Sec. 2.5.2, it could be supposed that temporally varying shear flows might change too fast to reduce turbulent transport. The search for ZFs has revealed that time-dependent shear flows in the form of GAMs, which can be considered as damping mechanism of the ZF, are the dominant contribution to the average poloidal flow in the entire plasma and the ZFs rather show up as the envelope of the GAM amplitude. The turbulent transport shown on the right-hand side of Fig. 6.1 suggests that the effect of GAMs on radial transport is similar to that of ZFs. Transport events with long radial correlation length are decorrelated when the GAM amplitude is large enough.

In order to examine the correlation of the radial transport with poloidal flow shear more quantitatively, a cross-correlation analysis was carried out. The average degree of correlation as a function of the spatial lag Δx was calculated according to

$$\langle C_{uv} \rangle_t = \frac{1}{\tau} \int \int \frac{(u(x,t) - \langle u(x,t) \rangle_x)(v(x+\Delta x,t) - \langle v(x,t) \rangle_x)}{\sigma_{u,x} \sigma_{v,x}} dx dt, \quad (6.1)$$

where τ denotes the time window used for averaging. Interchanging x and t in (6.1) yields the spatially averaged degree of correlation given by Eq. (4.6) as a function of the time lag Δt . Fig. 6.3 shows the result for the temporally averaged (left) and the spatially averaged (right) cross-correlation between radial transport ($v = \Gamma^x$) and poloidal flow shear ($u = |\partial_x U^y|$). A clear anti-correlation is found in space and time. Regions with strong flow shear are related to regions of reduced radial transport. Furthermore, the reduction in

6. Natural shear flows in TJ-K

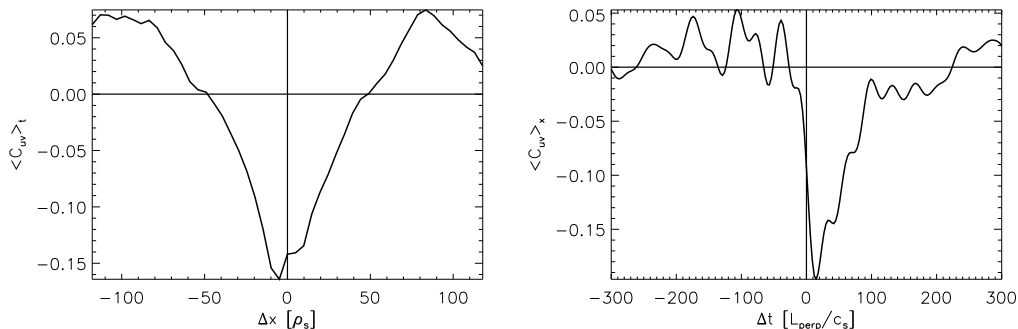


FIG. 6.3: Temporally averaged cross-correlation $\langle C_{u,v} \rangle_t$ (left) and spatially averaged cross-correlation $\langle C_{u,v} \rangle_x$ (right) of radial transport $v = \Gamma^x$ with absolute flow shear $u = |\partial_x U^y|$. The anti-correlation between the flow shear and the radial transport is apparent.

transport is delayed by about $15 L_{\perp}/c_s$ with respect to the maximum in flow shear. This points to the causality that the flow shear suppresses transport. Hence, the GAM has a similar effect on transport as the low frequency ZF.

6.1.2 Relation of zonal flows with Reynolds stress

As introduced in Secs. 2.5.3 and 4.2.4, different bispectral quantities have been proposed for the investigation of the RS drive of ZFs. The basic quantity relies on small-scale drift-waves coupling non-linearly into the large-scale ZF. The small-scale drift-waves are represented by the fluctuations of the radial and poloidal velocity components \tilde{u}^x and \tilde{u}^y , the large-scale ZF by the zonally averaged vorticity $\langle \Omega \rangle_{y,s}$. The RS drive should be reflected in the total integrated cross-bicoherence (4.21) of these quantities decomposed in wavenumber space, where the physical process happens.

The full information to calculate this expression is only available from simulated data. In experiments, a reduced number of data, sometimes even single point measurements have to be used. The objectives are to investigate (i) whether there is a correlation if use can be made of the full data and if so (ii) whether the correlations also show up in a reduced data set as used, e.g., for the auto-bicoherences of density and potential fluctuations. Hence, four different bicoherences are calculated: the full one using the appropriate velocities in k - (rewritten as $b_{u,k}$) and in frequency space ($b_{u,f}$) as well as auto-bicoherences in density (b_n) and potential (b_ϕ), which both are, of course, calculated in frequency space. In Figs. 6.4 and 6.5 the estimates for the total integrated bicoherences are compared with the poloidal flow and the flow shear.

Details of the data analyses are as follows: For the cross-bicoherence in

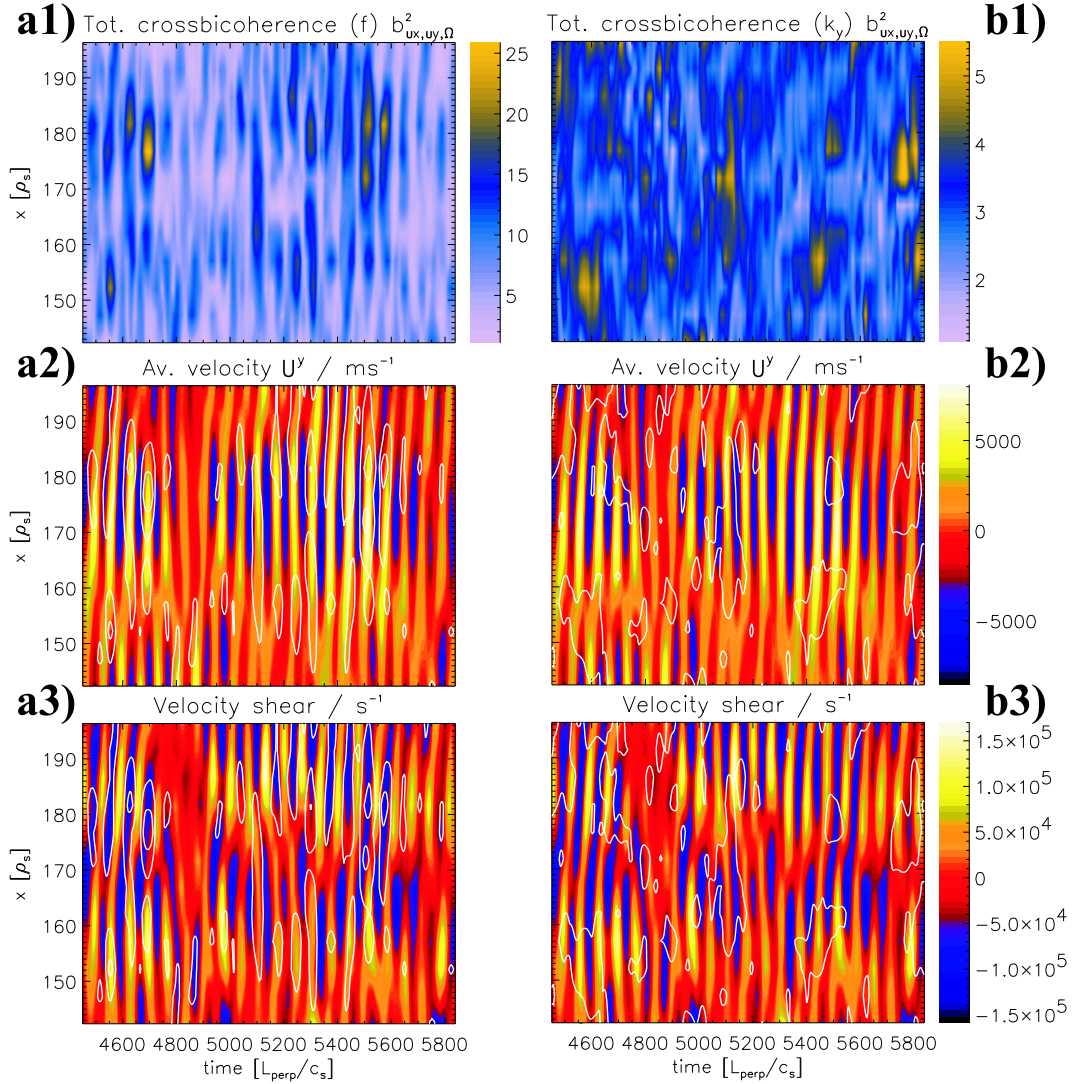


FIG. 6.4: (t, x) -profiles of total integrated cross-bicoherences in comparison with the average poloidal flow and the flow shear. The left column refers to $b_{u,f}$ (a1) and the right column to $b_{u,k}$ (b1). Contours from both quantities are overlaid on the flow U^y (a2, b2) and the flow shear $\partial_x U^y$ (a3, b3) profile. High values $b_{u,f}$ are located at high values of the flow shear.

6. Natural shear flows in TJ-K

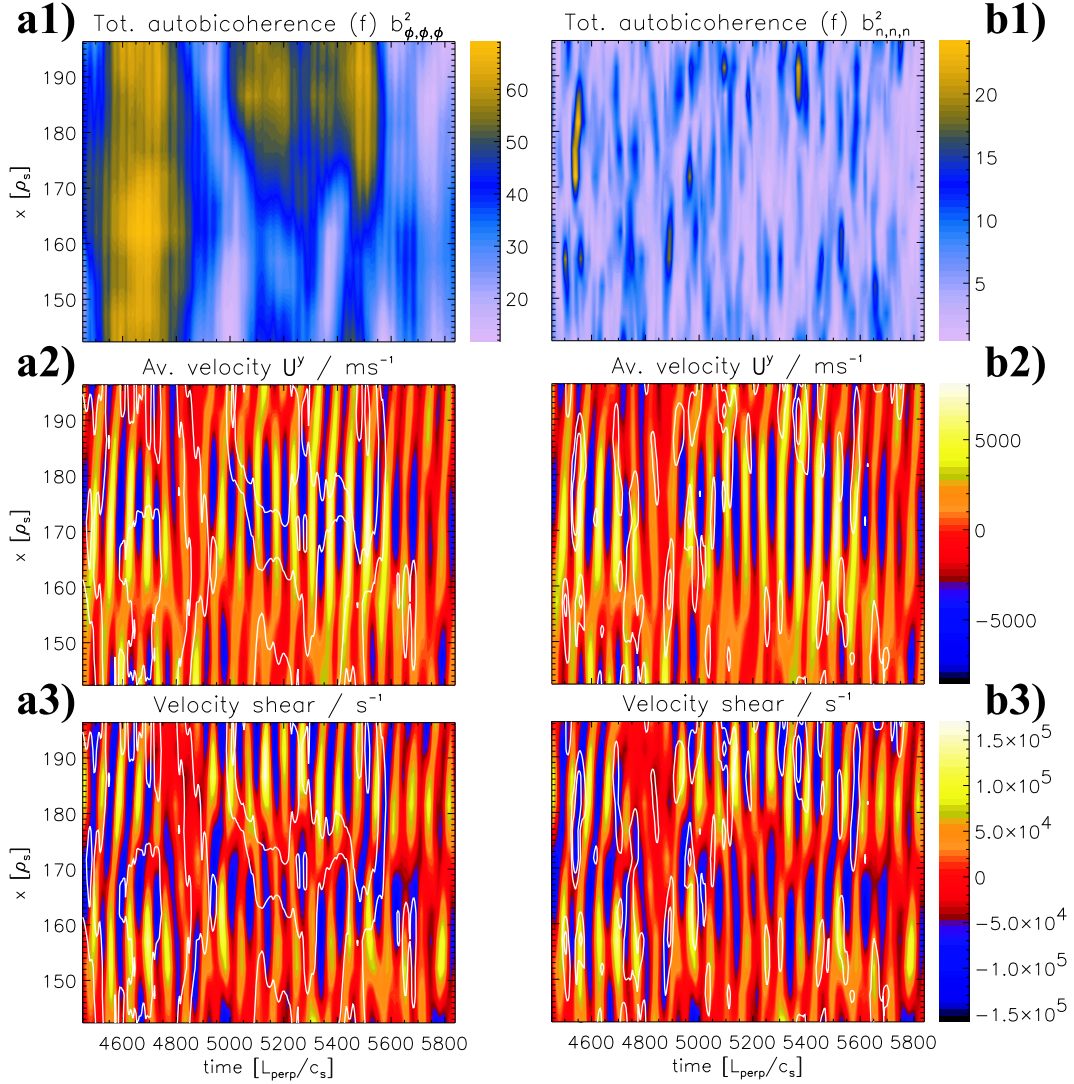


FIG. 6.5: (t, x) -profiles of total integrated auto-bicoherences in comparison with the average poloidal flow and the flow shear in the same representation as in Fig. 6.4. The left column refers to b_{ϕ} (a1) and the right column to the b_n (b1), both calculated in frequency space. A correlation with the flow or the flow shear is not observable in the case of b_{ϕ} . The bicoherence related to density fluctuations reveals an irregular conformance with the flow shear.

wavenumber space the quantities \tilde{u}^x , \tilde{u}^y and $\langle\Omega\rangle_{y,s}$ are calculated on a grid of 128 points in y direction. Note that $\langle\Omega\rangle_{y,s}$ represents the value of the Fourier spectrum at $k_y = 0$. For averaging, 24 realisations are taken from a time window of the size $T = 70 L_\perp/c_s$. This corresponds to one GAM period. The resulting total integrated bicoherence $b_{u,k}$ is assigned to a point in time at the centre of the window, from which the realisations are taken. Similarly the cross-bicoherence in frequency space is calculated: Frequency spectra are calculated on time windows of size $T = 70 L_\perp/c_s$ and 128 samples are averaged along the y coordinate. I.e. from 128 realisations the total integrated bicoherence $b_{u,f}$ is calculated and assigned to one point in time determined by the centre of the time window. The integrated bicoherence is calculated in a small range around $\omega = 0$. A sliding window is used for temporal resolution. With the same method the total integrated auto-bicoherences of potential and density fluctuations b_ϕ and b_n are calculated: Time windows with a length of $T = 70 L_\perp/c_s$ are applied to time series, averaging is performed along the y direction resulting in an average over 128 realisations.

The results shown in Figs. 6.4 and 6.5 are from the area indicated by the horizontal box in Fig. 6.1. The profiles of the total integrated cross- and auto-bicoherences are shown in the top row, where magnitudes are depicted in units of the respective noise level. In the middle row, the profiles of the average poloidal flow are overlaid with contour lines of the bicoherence profiles from the top. The bottom row shows the overlay of the flow shear profiles with these contour lines. Fig. 6.4 refers to the cross-bicoherences $b_{u,f}$ (left column) and $b_{u,k}$ (right column) and Fig. 6.5 refers to the auto-bicoherences b_ϕ (left column) and b_n (right column).

The overlay of the flow and the vorticity (flow shear) profiles with contours of $b_{u,f}$ in Fig. 6.4 clearly shows that high values of this bispectral quantity exist in the vicinity of high flow values and coincide in rather good agreement with high values of the flow shear. $b_{u,f}$ is in phase with the flow shear on the high-pressure side (small x) and out of phase on the low-pressure side. This is due to the fact that the bicoherence is positive by definition while the flow shear changes its sign. In wavenumber space the correlation of $b_{u,k}$ with the flow or the flow shear is not as clear as in frequency space.

The auto-bicoherence b_ϕ in Fig. 6.5 (left) does not show any correlation with the flow or the flow shear. The bicoherence b_n related to density fluctuations (Fig. 6.5, right), on the other hand, has regions with a high amount of three-mode interactions, which irregularly overlap with regions of high flow shear. This might be related to the fact that the GAM appears as pressure perturbation in the poloidal direction.

For a quantitative analysis, cross-correlations between the bicoherences and the absolute amplitude of the flow shear were calculated according to equation (6.1), where x and t have to be interchanged. The results for the spatially averaged cross-correlation $\langle C_{u,v} \rangle_x$ are shown in Fig. 6.6. The qualitative results

6. Natural shear flows in TJ-K

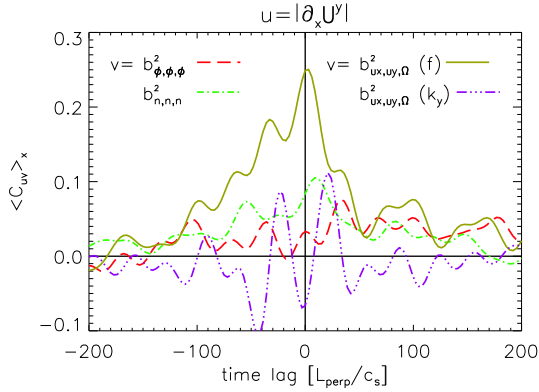


FIG. 6.6: Spatially averaged cross-correlations $\langle C_{u,v} \rangle_x$ of respective bicoherences with absolute flow shear $u = |\partial_x U^y|$. A reasonable correlation of 25% is found between the flow shear and the cross-bicoherence $b_{u,f}$ at $\Delta t = 0$.

from Figs. 6.4 and 6.5 are confirmed. The only quantity with a reasonable correlation of 25% is the full bicoherence calculated in frequency space. A time lag, which would be an indication of RS drive of the flows, is not observed. However, the width of the correlation function is larger than the GAM period and asymmetric. This might point to some correlation of RS-drive with the zero frequency component of the ZF, which always has some amplitude in the system. The correlation of the flow shear with the bicoherence calculated in k space is less than 15%. The cross-correlations between the bicoherences and the flow itself are below 10%.

6.2 Shear flows in TJ-K

In the previous study, it turned out that the auto-bicoherences, which would be accessible in the experiment, do not adequately reflect the ZF drive. They would have been a perfect indicator of ZFs. Nevertheless, there is another rough indicator for the existence of ZFs in toroidal experiments, namely the GAM. For the investigation of the influence of shear flows on turbulent structures in TJ-K, the existence of GAMs and the natural shear layer are discussed.

6.2.1 Zonal flows in TJ-K

In toroidal geometry, GAMs come together with ZFs as a sink of ZF energy. They can dominate the average poloidal flow. Since turbulent structures in the plasma density are advected by the background flow, an oscillation of the background flow could be reflected in the power spectrum of density fluctuations. In this case, especially the c_s dependence should be a signature for the observation to be a GAM. In Fig. 6.7, the calculated GAM frequency for five gases from hydrogen to argon in the range up to $T_e = 25$ eV is shown. The frequencies have been calculated according to the exact expression for tokamak geometry given in Ref. [67]. In TJ-K the helical magnetic field ripple with a toroidal symmetry of 6 dominates the toroidal field ripple, which causes the GAM in simple tokamak geometry. Hence, one could assume that

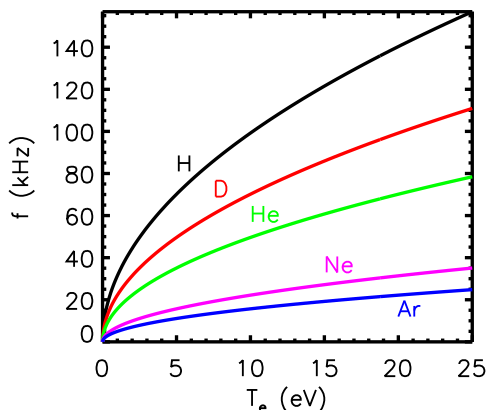


FIG. 6.7: GAM frequency for the gases hydrogen, deuterium, helium, neon and argon as calculated from the exact expression given in Ref. [67] for typical parameters in TJ-K.

the GAM frequency is six times larger. Theoretical predictions do not exist. Therefore, for typical parameters of TJ-K, the GAM frequency is given by $f_{\text{GAM}} = 6 \times 0.32 \times c_s / R_0$. The magnetic ripple would modify the poloidal pressure asymmetry associated with an asymmetric poloidal $E \times B$ rotation and thus the GAM frequency in TJ-K (see Sec. 2.5.4). As shown in Fig. 3.5, the electron temperature approximately ranges from 5 eV to 10 eV in the region, where density structures have been detected. For this temperature range, the GAM frequencies are summarised in Tab. 6.1. The spectra of density fluctua-

	Ar	Ne	He	D	H
$f_{\text{GAM}}/\text{kHz}$	11–16	16–22	35–50	50–70	70–99

TABLE 6.1: Calculated GAM frequencies in the range $T_e = 5\text{--}10\text{ eV}$.

tions shown in Fig. 5.2 do neither show signs of prominent peaks in the range of the GAM prediction nor show a scaling behaviour of the present peaks with c_s , i.e., essentially with the ion mass. It could be argued that GAMs might be better reflected in the spectra of floating potential fluctuations. For a large number of discharges in all gases, density and potential spectra were available and have been checked for typical GAM characteristics at first instance. The search for GAMs was not successful. One possible reason might be the complex topology of the magnetic field. The observation of GAMs has been reported, e.g., in Ref. [66], in tokamaks, which possess a less complicated magnetic field geometry compared to stellarators.

6.2.2 Natural shear layer

In Fig. 3.5, radial profiles of the floating potential show a pronounced minimum at the separatrix indicating a localised shear layer. The higher the ion mass is the stiffer the gradients get. Hence, for higher ion masses, the radial electric

6. Natural shear flows in TJ-K

field and thus the local shear would be expected to be larger. On the basis of the shear decorrelation mechanism, a stronger effect of flow shear on dominant large structures rather than on smaller ones would be expected. It must be stressed that the profiles of the plasma potential measured with emissive probes are much smoother than that of the floating potential [89]. Radial electric fields evaluated from the profiles of the floating potential – and thus the values of the deduced shear – might generally be overestimated. An exact quantitative analysis is not sensible until detailed information on particular electric fields and growth rates are available. Nevertheless, the profiles of ϕ_f reflect the local increase of radial electric fields and the corresponding shear with increasing ion mass. In this context, the decorrelation of density structures should be reflected in a drop of the radial correlation length in a narrow region of the separatrix, especially for argon.

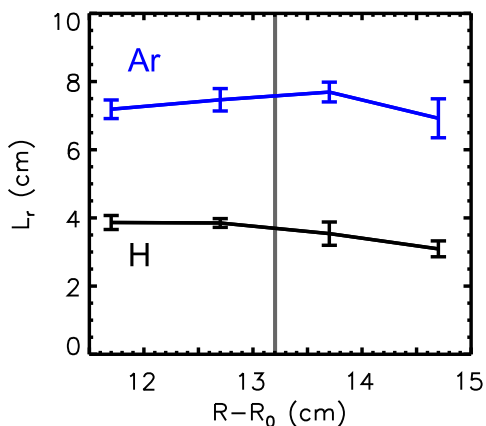


FIG. 6.8: Radial dependence of the radial correlation length in a narrow region of the separatrix (vertical line). L_r is shown for an hydrogen (#2543) and an argon (#2544) discharge. A drop of L_r due to the shear at the separatrix is not observed.

Fig. 6.8 shows the radial correlation lengths for an hydrogen and an argon discharge at the separatrix. For the evaluation of L_r , the 8×8 probe array was centred on the separatrix. Regarding the error bars, no obvious signs of an influence on turbulent structures via the shear decorrelation mechanism are found in this region of TJ-K plasmas. In particular, no strongly asymmetric behaviour around the separatrix is found. Similar observations have already been made in the ASDEX tokamak [107] by measuring wavenumber spectra with a poloidal multi-probe array. Although Fig. 6.8 might indicate a slight trend towards smaller L_r outside the separatrix, it must be stressed that this could also be an effect of a change in the dynamics. Outside the separatrix, the magnetic field lines end on the vacuum vessel, which points to a breakdown of the three-dimensional dynamics of drift-waves in this region. This issue is currently under investigation.

The spatial correlation between transport and $E \times B$ shear shown on the left-hand side of Fig. 6.3 might suggest that shear flows affect the turbulence characteristics spatially prior to the shear or at least in the range of several ρ_s . In this case, the impact of shear flows on turbulent structures could be regarded as a rather global effect, since in TJ-K ρ_s is rather large. In particular, the impact would not be reflected in the narrow region of the shear layer only.

The decorrelation of large-scale structures would still be a possible explanation for the observation that those in argon as measured inside the separatrix tend to be smaller than in neon. This is not confirmed in the next chapter. It will turn out that in the presence of externally induced shear flows, which – according to the stabilisation criterion (2.27) – should be strong enough, turbulent structures do not show a decrease in radial correlation lengths.

6.3 Summary and conclusions

Data obtained from the drift Alfvén turbulence simulation code DALF3 were analysed for the existence of zonal flows (ZF). It was found that ZFs come in two types, a low frequency zonal flow ($\omega = 0, k_y = 0$), which was originally considered for turbulence decorrelation, and flows at the geodesic acoustic mode (GAM) frequency ($\omega \neq 0, k_y = 0$), which scales with c_s/R_0 . Both types make the major contribution to the auto-power spectrum of the flux surface averaged poloidal flow. The mean poloidal flow is clearly dominated by the GAM oscillations. It was demonstrated that the flow shear due to the GAMs, which can be considered as damping mechanism of low frequency ZFs, also contributes to a reduction in radial transport. The maximum in shear flow was found to occur prior to a reduction in transport.

In the simulation, the drive of ZFs is due to Reynolds stress (RS). The drive of the GAM by RS should actually be stronger than that of the low frequency ZF. Bispectral methods have been suggested to be an appropriate tool to experimentally study this mechanism. The total integrated cross-bicoherence of $E \times B$ velocity fluctuations \tilde{u}^x, \tilde{u}^y and the zonally averaged vorticity $\langle \Omega \rangle_{y,s}$ is a measure of the correlation between the mean poloidal flow and the RS. In order to investigate the efficiency of this technique, different bispectral analyses were carried out on the simulated data.

The strongest correlation was found when the analysis was carried out in frequency space. The spatial and temporal evolution of flow shear coincides with an increased amount of three-mode interactions indicated by the total integrated cross-bicoherence. The cross-correlation between the bicoherence and the flow shear is about 25% when averaged over the radial coordinate. The correlation function is broader than the GAM period and asymmetric. This could be a hint to RS drive of the low frequency ZF. The analysis in k space did not show any clear relation between flow and bicoherence.

In experimental investigations, the use of the auto-bispectrum would be much more appropriate. However, no clear correlation of the mean poloidal flow and the total integrated auto-bicoherence of plasma potential or density fluctuations was found. In the case of the auto-bicoherence of density fluctuations some relation with the flow shear was found, which might be related to the pressure perturbation of the GAM.

6. Natural shear flows in TJ-K

The occurrence of shear flows in TJ-K was discussed with respect to the shear decorrelation mechanism. The existence of ZFs/GAMs should be indicated by peaks in the spectra of potential or density fluctuations, whose frequency scales with c_s/R_0 . Such a scaling behaviour was not found in TJ-K. Another candidate for the shear decorrelation is the natural shear layer localised at the separatrix. A radial decorrelation of turbulent structures was not observed in this region.

In summary, the GAM was found to be the dominant poloidal flow in the simulation data with a similar effect on radial transport as the low frequency ZF. A correlation between RS and ZF/GAM could only be detected in the cross-bicoherence taken in frequency space. The auto-bicoherences do not appear as a useful quantity to study the interaction of RS and ZF/GAM. RS has not been observed as a clear precursor of strong ZF or GAM amplitudes. It rather appears simultaneously in the region of radial ZF and GAM gradients. Although the RS is the only mechanism in the code driving large-scale ZFs, in the bispectral analysis the RS could not be detected as such. In TJ-K plasmas, no obvious signs for the existence of ZFs or GAMs were found. Local $E \times B$ shear at the separatrix did not turn out to have a local influence on radial correlation lengths.

Plasma biasing

In a simple picture of the shear decorrelation mechanism, turbulent structures are stretched in the flow direction until they are disrupted. Therefore, the destruction of the structure in the presence of a $E \times B$ shear flow should be observable in a decrease of the radial correlation length. In order to investigate this mechanism, shear flows are needed first. In the previous section, it was shown that neither zonal flows nor the natural shear layer are suitable for the investigation of the shear decorrelation mechanism. As introduced in Sec. 2.5.5, $E \times B$ shear flows can be induced externally by plasma biasing. In the following, different schemes are tested for the applicability of plasma biasing in TJ-K. The influence of externally induced $E \times B$ shear flows on turbulent structures is investigated.

7.1 Applied biasing schemes

In all biasing schemes, the electrode material was stainless steel and they have been inserted from the top port (T1). The electrodes were positively biased with respect to the grounded vacuum vessel. Negatively biased electrodes did not turn out to have an significant effect on the plasma conditions.

7.1.1 The standard biasing scheme

The first experiments have been carried out applying the standard biasing scheme as depicted in Fig. 2.10, where a small electrode is inserted. Electrodes of different shapes (spherical and disk-like) have been inserted into the plasma on various radial positions and biased up to 200 V. The currents drawn from the plasma were less than 2 A. Using this schemes, the effects on line averaged densities and radial profiles of, e.g., the density and the floating potential were found to be marginal. In order to get an impression of the influence within the full poloidal cross-section, floating-potential measurements have been carried out by means of a 2D-movable Langmuir probe. In Fig. 7.1, the difference in floating potential between a biased and an unbiased hydrogen discharge is shown at $B = 89 \text{ mT}$, $P_{\text{ECRH}} = 1.8 \text{ kW}$ and $p = 5 \times 10^{-5} \text{ mbar}$. In general, the grounded electrode will be referred to as unbiased. A spherical electrode with

7. Plasma biasing

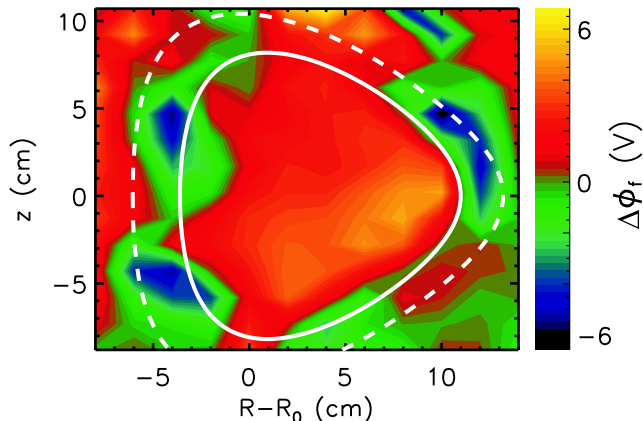


FIG. 7.1: Profile in the poloidal cross-section of the difference in floating potential between a biased and an unbiased hydrogen discharge (#2235, #2236). The spherical electrode was biased with $U_b = 150$ V. The electrode touches the flux surface marked by the solid curve. The dashed curve indicates the separatrix. In the poloidal direction, irregular perturbations are observed.

a diameter of 1 cm was used and biased with $U_b = 150$ V. Fig. 7.1 shows that the floating potential is perturbed only by a fraction of 4% of the bias voltage. It can be seen that the potential perturbation due to a small probe is rather irregular, but stays on the biased flux surface. This poloidal inhomogeneity points to perturbations of the potential being induced on a flux tube of finite length rather than on the whole flux surface, which might also implicate the inefficiency of this biasing scheme and explain, why the influence on radial profiles is rather marginal.

7.1.2 Extended biasing probes

In following experiments, a ring-like electrode aligned to a flux surface was used. Although this shape is more likely to guarantee a uniform perturbation of the plasma potential on the flux surface, it suffers from the lack of flexibility. For further investigations, two variations have been used: (A) A wire of 3 mm diameter in the form of the separatrix and (B) a plate with an extent of 3 mm in radial and 15 mm in toroidal direction, which was aligned on a flux surface in the vicinity of maximum density gradients and fluctuation levels.

In Fig. 7.2, a typical scenario with the biased ring-probe is shown. The bias voltage was ramped up and down within a cycle of a duration of approximately 20 s. The dependence of the current drawn with the ring-probe, the line averaged density and the reflected heating power on the bias voltage is shown for an argon discharge at $B = 82$ mT, $P_{\text{ECRH}} = 1.8$ kW and $p = 4 \times 10^{-5}$ mbar. When the increasing voltage passes 68 V, a sudden drop in current and density as well as an increase in reflected heating power indicates a transition in the plasma state. In Ref. [19], a sudden drop of the electrode current marked the transi-

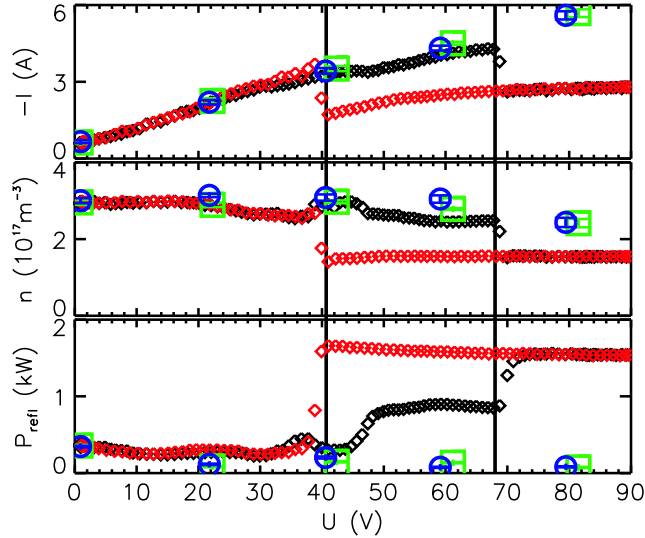


FIG. 7.2: Scenario of plasma biasing in an argon discharge (#2997) at $B = 82$ mT, $P_{\text{ECRH}} = 1.8$ kW and $p = 4 \times 10^{-5}$ mbar. The current drawn with the electrode (top), the line averaged density (middle) and the reflected heating power (bottom) are depicted as functions of the bias voltage, which was ramped up (black diamonds) and down (red diamonds) in a cycle. Sudden transitions at $U_b \approx 70$ V and $U_b \approx 40$ V as marked by vertical lines indicate a hysteresis. The transitions and the hysteresis are not apparent, when the microwave is rematched in order to maintain constant heating power as shown for certain voltages in the ramped-up (squares) and the ramped-down phase (circles).

tion into a better confinement regime in the form of a bifurcation in plasma rotation accompanied by an increase of radial resistivity (see Sec. 2.5.5). In the present case, the sudden drop in density might be related to the heating mechanism. The plasma densities are above ECRH cutoff. The working hypothesis is that there exists a standing wave between the cutoff surface and the wall with a fraction of the wave tunnelling to the core plasma by the O-X-B mode conversion process. Changes in density gradient lead to a change in the boundary condition for the wave as indicated by a sudden increase in reflected power and therefore a possible improvement in confinement is nullified due to the reduced heating power. A further increase of the bias voltage leads to a slight increase of the electrode current. The other parameters remain rather constant. Decreasing the voltage again leads to a transition back to the original plasma condition at a voltage of about 40 V and one finds a hysteresis in all signals.

In order to compensate the drop in ECRH power, the wave can be rematched. If this is done for each voltage, the hysteresis vanishes as indicated by squares and circles in Fig. 7.2. In this case, higher currents can be drawn than in the unmatched case, which suggests increasing plasma rotation. In this region, the line averaged density slightly decreases at increasing voltage. It must be stressed that the line average density does not give information

7. Plasma biasing

on the profile shape of the density. Although the average density decreases, higher local densities with steeper gradients are measured as will be shown in the following sections. As a prominent feature lowest reflected powers have been achieved during biasing.

Without rematching, the threshold voltage of the transition depends on the discharge parameters. In particular, the width and the position of the hysteresis depends on the neutral gas pressure, the magnetic field strength, on the working gas and on the matching of the microwave injection itself. The latter interferes with a systematic analysis, since the matching is rather intuitive and does not allow for a systematic variation. Wave field measurements, which are currently in progress, might reveal detailed insight into the process of plasma production. In comparative studies for typical discharge parameters in TJ-K it turned out, that as rule of thumb, the transitions occur at a bias voltage in a range between 10 and 100 V. Without rematching the electrode current is between 1 and 5 A without rematching. With rematching, currents of up to 10 A can be drawn.

For a detailed investigation of the influence of plasma biasing on equilibrium profiles and fluctuations, the working point was chosen at a few Volts beyond the first transition and the microwave injection was rematched. In the following, the phenomenology of plasma biasing is presented in more detail. A grounded electrode will be referred to as unbiased. Measurements with a grounded and floating electrode showed no differences in the profiles. However, the profiles may differ from those shown in Fig. 3.5, since the electrode has a perturbing effect on the plasma.

7.2 Ring biasing at the separatrix

To bias directly at the separatrix has been reported to induce localised shear layers most efficiently [73]. First result from separatrix biasing have been published in Ref. [108].

7.2.1 Influence on the equilibrium profiles

In the following, the results are shown for an argon discharge at $B = 89$ mT, $P_{\text{ECRH}} = 1.8$ kW and $p = 5 \times 10^{-5}$ mbar. In Fig. 7.3, radial equilibrium profiles of an unbiased (dots) and a biased (circles) discharge are compared. The bias voltage was 56 V and the current drawn by the electrode was about 4 A. As shown on the left-hand side of Fig. 7.3, the floating potential is increased by about 40 V in the plasma centre and by about 20 V near the separatrix, which points to an increase in the radial electric field near the separatrix during biasing. The potential fluctuation amplitudes indicated by the error bars are reduced. In the middle of Fig. 7.3, the shear in the poloidal $E \times B$ velocity

7.2 Ring biasing at the separatrix

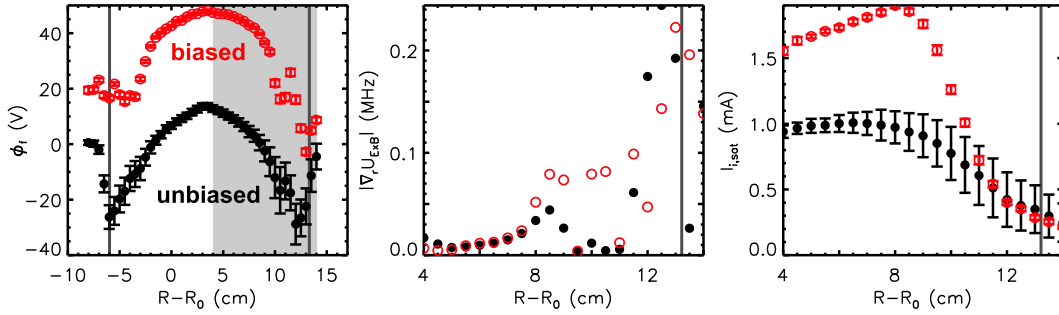


FIG. 7.3: Effect of separatrix biasing on the equilibrium of an argon discharge (#2249, #2250). The floating potential (left) is increased across the entire cross-section. The separatrix is depicted by vertical lines. In the shaded region, the absolute value of the shear in the poloidal $E \times B$ flow as estimated from ϕ_f (middle) is increased in a range $R - R_0 = 8-12$ cm during biasing. The profile of the ion-saturation current (right) indicates an increased density gradient. The bars indicate the rms fluctuation.

as calculated from ϕ_f and the local magnetic field strength is shown at the outboard midplane, where generally the largest transport levels are observed. The radial electric field has been calculated from the floating potential and corrected by a factor of 0.1 as was done in Sec. 3.3.2. This bases on observations that radial electric fields calculated from the plasma potential are an order of magnitude smaller than those from the floating potential [30]. An increase of the flow shear in the range $R - R_0 = 8-12$ cm inside the separatrix is found. As introduced in Sec. 2.5.2, a suppression of turbulence is achieved when the flow shear exceeds the maximum linear growth rate of unstable drift-modes $\gamma_{\max} \approx c_s/R_0$. For argon, γ_{\max} is in the range 6–8 kHz. In the region of increased shear, the flow shear is an order of magnitude higher than γ_{\max} . Also the fluctuation amplitudes of the ion-saturation current are decreased (see Fig. 7.3, right). The shape of the profile shows a gradient, which is steepened by a factor of 3.

7.2.2 Influence on the poloidal flow

In Fig. 7.3, the steepened density gradient at about $R - R_0 = 10$ cm indicates an increase in the poloidal electron-diamagnetic-drift velocity $U_{dia,e}$. Due to the high floating potential in the biased phase, swept Langmuir probes failed at measuring profiles of n_e and T_e , which are necessary for the evaluation of $U_{dia,e}$. In a region at $R - R_0 = 10$ cm, Fig. 7.3 (right) indicates that in the biased case $U_{dia,e}$ is increased by a maximum factor of 3, which might be overestimated compared to the actual pressure gradient. In this region, typical values are 1–2 km/s as can be seen in Fig. 3.6 for the unbiased case. Fig. 7.4 shows the poloidal $E \times B$ velocity $U_{E \times B}$ as calculated from the floating potential and the local magnetic field strength. The same correction has been made as for the flow shear. In the region at $R - R_0 = 10$ cm, $U_{E \times B}$ is about

7. Plasma biasing

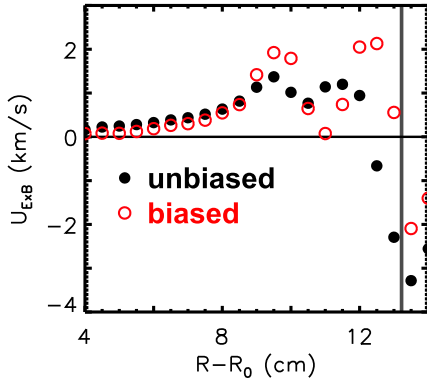


FIG. 7.4: Radial profile of the poloidal $E \times B$ velocity in the same representation as the flow shear in Fig. 7.3.

1 km/s in the unbiased case and about 2 km/s in the biased case. Hence, the propagation velocity of density structures would change from up to 1 km/s to 1–4 km/s during biasing. The direction would still be that of the electron-diamagnetic drift. However, it must be stressed that these estimates are not accurate. Furthermore, it could be assumed that the change $\Delta\phi_f = \phi_f^b - \phi_f$ in the floating potential due to biasing is the same for the plasma potential, i.e., $\Delta\phi_p = \Delta\phi_f$. Then the induced radial electric field can be decomposed into the original part and an induced part according to

$$\begin{aligned} E_r^b &= -\nabla_r \phi_p^b = -\nabla_r (\phi_p + \Delta\phi_p) = -\nabla_r \phi_p - \nabla_r (\phi_f^b - \phi_f) \\ &\approx -\nabla_r (\phi_f^b - \phi_f), \end{aligned} \quad (7.1)$$

where the original part can be neglected in the case of efficient biasing. The resulting $E \times B$ flow and its shear can be recovered in the presented as the difference between the biased and the unbiased case but an order of magnitude larger. Hence, the $E \times B$ velocity could reach values of about 10 km/s in the region at $R - R_0 = 10$ cm. The dominance of the poloidal $E \times B$ flow should be reflected in a change of the propagation direction of the structures.

Another important aspect is the Doppler shift in frequency spectra arising from changes in the propagation velocity of the structures. A poloidally propagating structure with a certain poloidal wavenumber k_θ and a velocity of U_θ would be reflected in the power-spectrum at $\omega = k_\theta U_\theta$ [109]. Assuming that the turbulence drive is dominated by drift-waves and the $E \times B$ velocity is negligible, it is $\omega \approx k_\theta U_{\text{dia,e}}$. In the case of efficient plasma biasing, $U_{E \times B}$ should become dominant, which yields $\omega^b \approx k_\theta U_{E \times B}^b$. Under the assumption that k_θ does not change during biasing a simple relation between both frequencies can be deduced:

$$\omega^b \approx \omega U_{E \times B}^b / U_{\text{dia,e}}. \quad (7.2)$$

This relation depends on the ratio of the $E \times B$ velocity in the biased case to the electron-diamagnetic-drift velocity in the unbiased case. It must be stressed that a decorrelation of structures as could be expected in the presence of strong flow shear would lead to higher frequencies ω^b . The influence of

plasma biasing on spectra and turbulent structures will be addressed in the following.

7.2.3 Influence on the fluctuations

In order to examine the effect of biasing on the fluctuations, radial measurements with the transport probe (see Sec. 3.2.2) have been carried out. On the

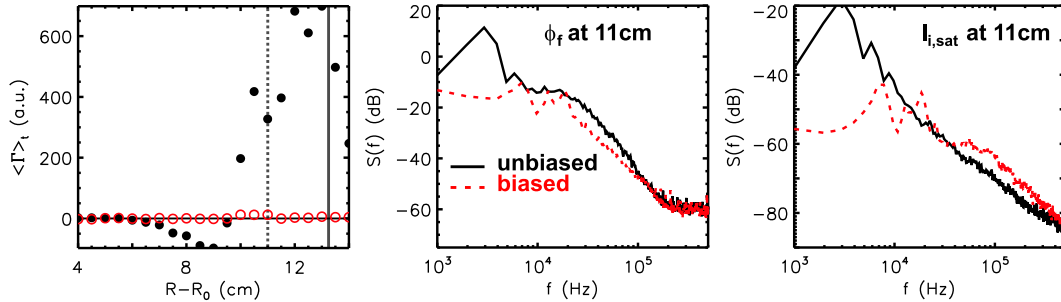


FIG. 7.5: Local turbulent transport (left) in the same representation as the $E \times B$ flow in Fig. 7.3 and from the same data. The transport is dramatically reduced during biasing (circles). The dotted vertical line marks the position, at which the auto-power spectra of fluctuations in the floating potential (middle) and ion-saturation current (right) are compared for the biased (dashed line) and unbiased (solid line) case. Fluctuation amplitudes are reduced and a dominant mode at 3 kHz is damped.

left-hand side of Fig. 7.5, the local turbulent transport calculated according to Eq. (2.19) with the zonal average replaced by the temporal one is shown. The maximum outward transport is found near the separatrix when the electrode is unbiased. Also an inward transport can be observed for $R - R_0 < 10$ cm reflecting the findings of Sec. 5.3 for the cross-phase in argon discharges. In the biased phase, the radial transport is reduced drastically. For one position in the range of maximum density gradients and fluctuations levels at $R - R_0 = 11$ cm, the auto-power spectra of fluctuations in floating potential and ion-saturation current are shown in the middle and on the right-hand side of Fig. 7.5, respectively. For ensemble averaging, the time series were subdivided into 32 realisations of 2048 values. In the fluctuations of both quantities, a mode at 3 kHz is dominant. During biasing this mode is damped. Modes at 7 kHz and in the range 10–20 kHz show up instead. Floating potential fluctuations are reduced in a broad range up to 100 kHz. For the ion-saturation current, the fluctuations are damped in a smaller range up to 10 kHz. Beyond 10 kHz the power is even somewhat larger. This could point to a Doppler shift. In the biased case the spectrum appears shifted, i.e., from 100 kHz to 160 kHz. According to Eq. (7.2), this would indicate that $U_{E \times B}^b$ is 1.6 times larger in the biased case than $U_{\text{dia},e}$ in the unbiased case. However, Fig. 7.3 pointed to $U_{\text{dia},e}^b$ being enlarged by a factor of 3. This violates the assumptions made for deriving Eq. (7.2). Furthermore, this also implies that for argon the induction of $E \times B$ flows by separatrix biasing is not efficient. The use of Eq. (7.1) for

7. Plasma biasing

the radial electric field is not justified. Nevertheless, the flows estimated from the profiles shown in Figs. 7.3 and 7.4 might suggest a small contribution of a Doppler shift. In the analysis of the structures (Sec. 7.2.4), it will be shown that the peak at 7 kHz is not due to a Doppler shift. However, biasing does produce a change in the profile of the flow, which causes sufficient shear to influence fluctuations and transport.

The transport reduction at the position $R - R_0 = 11$ cm is documented in more detail in Fig. 7.6. Here, the cross-amplitude spectrum and the spectral cross-coherence and cross-phase between poloidal electric field and density fluctuations are shown. The cross-amplitude spectrum essentially reflects the

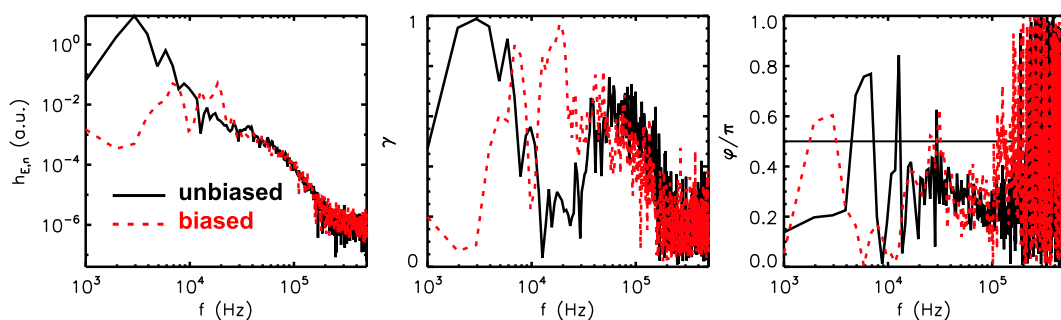


FIG. 7.6: Cross-amplitude spectrum (left), cross-coherence (middle) and cross-phase (right) between poloidal electric field and density fluctuations calculated from the same data as in Fig. 7.5.

combined features of the auto-power spectra shown in Fig. 7.5. For the unbiased case, this figure shows that the largest contribution to the turbulent transport is due to modes in electric field and density fluctuations at 3 kHz with a coherent phase relation and phases of about $\pi/5$ leading to outward transport. In the biased phase, the contribution to transport in the range below 7 kHz is strongly decreased, since in this region, phases of about $\pi/2$ without a significant coherence are found. The major contribution to transport is now due to modes at 7 kHz and modes in the range of 10–20 kHz. Here, a high degree of coherence with phases near zero is found. Nevertheless, the cross-amplitude in these regions is three orders of magnitude lower than the maximum in the unbiased case. No substantial changes are observed in the range beyond 20 kHz.

In Ref. [25] it has been confirmed that the dynamics in TJ-K is governed by drift-wave turbulence. The spectral cross-phases shown here would indicate, however, a dominant interchange-like mode at 3 kHz in the unbiased case. Actually, the cross-phase at dominant modes with high phase coherence depends on the radial position. This is demonstrated in Fig. 7.7, in which the radial profile of the average cross-phase calculated from Eq. (4.15) is depicted. For the unbiased case, cross-phases near $\pi/2$ at $R - R_0 \leq 10$ cm indicate the dominance of drift-wave turbulence. This is in reasonable agreement with results from previous studies [25, 89]. Near the separatrix, the cross-phases point to

7.2 Ring biasing at the separatrix

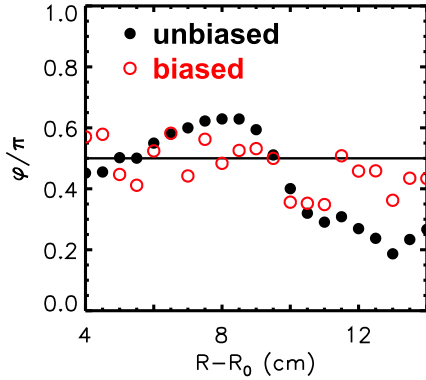


FIG. 7.7: Average cross-phase between poloidal electric field and density fluctuations. Drift-wave turbulence is indicated by phase values near $\pi/2$ for $R - R_0 \leq 10$ cm. For larger radii approaching the separatrix, φ shows a larger deviation from $\pi/2$. During biasing, the average cross-phase resides near $\pi/2$ in the entire radial range.

an increasing contribution of the interchange instability. In the biased phase, the phases are shifted closer to $\pi/2$ in the entire radial range.

It must be stressed that the frequency spectra calculated at one point in space need not necessarily reveal the dominant mechanism driving the turbulence. A fairly good statistic is required. Wavenumber spectra, for which a good statistic can be obtained from multi-probe measurements, should be used instead (see Sec. 4.2.2). In a previous study, measurements with a poloidal probe array have been carried out on a flux surface corresponding to $R - R_0 \approx 9$ cm inside the separatrix [25]. Drift-wave-like cross-phase signatures have been found in wavenumber space. Present results confirm these findings. Deviations from these results are found near the separatrix. Outside the separatrix, the parallel dynamics of drift-waves could be suppressed and interchange instabilities could become dominant due to the fact that the field lines end on the vacuum vessel. The average cross-phase presented here might indicate a transition to interchange instabilities dominating the turbulence drive outside the separatrix. In the unbiased phase, this effect might also be intensified by open field lines ending on the ring-probe.

7.2.4 Influence on propagating density structures

While fluctuations on large time-scales including a dominant mode at 3 kHz are damped during biasing, modes at 7 kHz and in the range 10–20 kHz emerge clearly as seen in Fig. 7.5. This might be a hint to shear decorrelation of large scales. Alternatively an increase in poloidal plasma rotation could shift the modes. In order to study the relation of turbulent structures to the peaks in the power spectrum, density fluctuations have been measured with the 8×8 probe array in the unbiased and the biased phase. Quasi-coherent structures have been detected by means of the cross-correlation analysis technique as described in Sec. 4.3.

In Fig. 7.8, the spatio-temporal evolution of turbulent density structures is compared for the unbiased and biased case. The unbiased case shows the usual situation as demonstrated in Fig. 5.4 for an helium discharge. Quasi-coherent

7. Plasma biasing

structures propagate in the direction of the electron-diamagnetic drift. For negative time lags Δt , the structure grows until it reaches the maximum extension at $\Delta t = 0$. For positive Δt , the structure decays again. In a duration of $40 \mu\text{s}$, the structure moves about 5 cm. The resulting velocity of 1.3 km/s is in reasonable agreement with the estimates made from the flow profiles. In

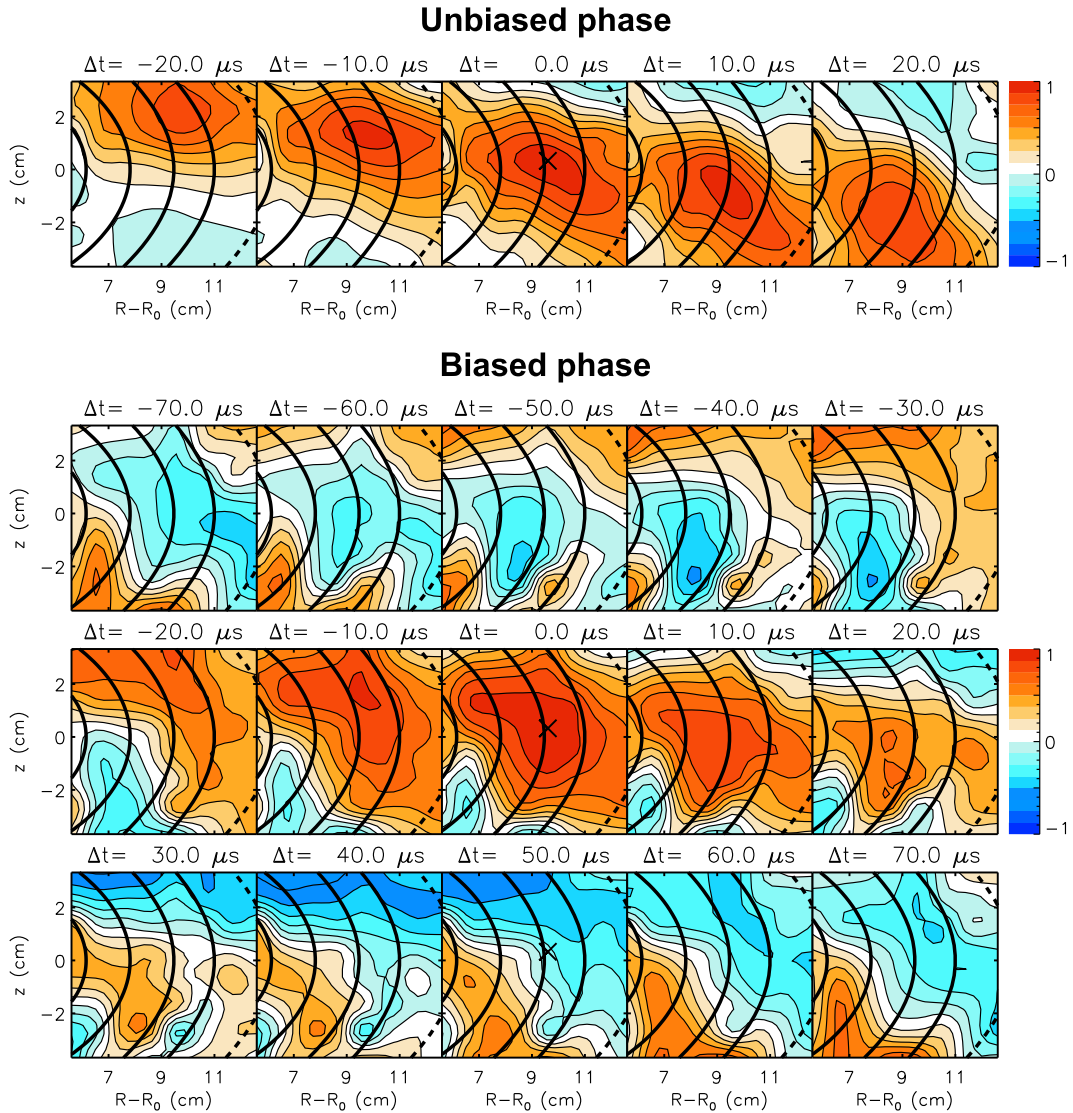


FIG. 7.8: Spatio-temporal evolution of turbulent density structures in an argon discharge for the unbiased (top) and the biased (bottom) case (#2430). The separatrix is depicted as dashed curve. The reference probe is marked by a cross.

the biased phase, the structure is clearly distorted. In the radial region, where Fig. 7.3 indicates a steepened density gradient at $R - R_0 \approx 10 \text{ cm}$, the structure is poloidally more elongated. In the same region, Fig. 7.3 also shows a layer of increased $E \times B$ flow shear. The contours are less smooth and elliptic. The structure appears distorted as one would expect from shear flow acting on it. At $\Delta t = 20 \mu\text{s}$, the structure is decayed into smaller structures. At $\Delta t = 0$,

7.2 Ring biasing at the separatrix

however, a radial decorrelation, i.e., a break up into smaller structures, is not observed. The decorrelation rather shows up in the temporal evolution of the structure. At $\Delta t = -20 \mu\text{s}$, the blob enters the matrix from the top. On its path to the bottom, the blob is first distorted. At $\Delta t = 20 \mu\text{s}$, the blob is destroyed and only smaller shreds of medium or low correlation values are left, while in the unbiased case the shape of the blob is still unchanged. Here, the correlation lengths appear shortened. As a consequence of the decreased correlation values, the lifetime of the blob appears shortened. At decreased transport levels and increased density gradients a decrease of the diffusivity would be expected. However, the diffusivity $D \approx L_c^2/\tau_c$ (Eq. (2.25) in Sec. 2.4.2) would be increased, since L_c evaluated at $\Delta t = 0$ is not decreased and τ_c is increased instead. Hence, the diffusivity (2.25) based on simple mixing-length estimates does not turn out to be an adequate quantity in the case of turbulence being affected by shear flows. Moreover, it is reasonable to assume that transport is reduced, when the lifetime of turbulent structures is decreased, i.e., when particles are not able to perform a full step L_c before the structure is destroyed. Hence, a shortening of the structures lifetime could be reinterpreted as a shortening of the radial step size of diffusive random walk processes leading to decreased transport levels.

A remarkable change in the propagation speed is not observed. Diamagnetic as well as $E \times B$ velocities are increased balancing to a propagation speed, which is rather unchanged compared to the unbiased case. In Sec. 7.3, it will be shown that an efficient induction of radial electric fields drastically affects the propagation speed and lead to a Doppler shift of prominent modes in the spectrum, which in the following is not confirmed for the present case.

The auto-correlation function (ACF) evaluated at the reference probe allows to make a link between the observed structures and the peaks in the power spectra. In Fig. 7.9, the ACF shows a period of $T \approx 250 \mu\text{s}$ for the

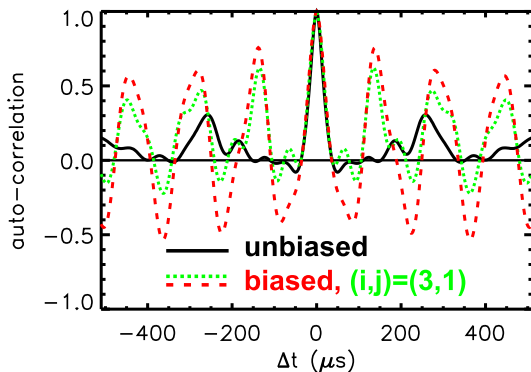


FIG. 7.9: Auto-correlation function (ACF) at the reference $(i, j) = (4, 4)$ of Fig. 7.8. The ACF shows a periodicity of $250 \mu\text{s}$ in the unbiased phase (solid line) and $150 \mu\text{s}$ in the biased phase (dashed). For comparison, the ACF at $(i, j) = (3, 1)$ in the region of strong temporal decorrelation is shown (dotted).

unbiased phase. Taking into account the frequency resolution of $\Delta f \approx 1 \text{ kHz}$, this is in reasonable agreement with the peak at 3 kHz in the power spectra of Fig. 7.5. In the biased phase, the period is reduced to $T \approx 150 \mu\text{s}$, which corresponds to the peak at 7 kHz . Contributions in the range $10\text{--}20 \text{ kHz}$ show

7. Plasma biasing

up as a modulation in the range $50\text{--}100\ \mu\text{s}$. Especially in the region of strong temporal decorrelation as represented by the probe tip at $(i, j) = (3, 1)$ (i.e. at $R - R_0 = 8.5\ \text{cm}$ and $z = -2.5\ \text{cm}$), this modulation, which might correspond to structures of smaller spatial scales, is prominent in the ACF. Nevertheless, fluctuations on larger scales – in particular fluctuations at $7\ \text{kHz}$ – are found to be dominant in the whole area. A squeezing of the ACF around $\Delta t = 0$, which would be a hint to a Doppler shift, is not observed. The shape of the ACF between -50 and $50\ \mu\text{s}$ is rather unchanged. The structure principally propagates in the poloidal direction. This might suggest that the peak at $7\ \text{kHz}$ is due to an increase in the poloidal wavenumber. Therefore, a spatial decorrelation would be observed rather in the poloidal than in the radial direction.

7.2.5 Experiments with small ion masses

Separatrix biasing has been performed also in hydrogen discharges. The results presented next are for a discharge at $B = 72\ \text{mT}$, $P_{\text{ECRH}} = 1.8\ \text{kW}$ and $p = 3 \times 10^{-5}\ \text{mbar}$. The electrode was biased with $U_b = 60\ \text{V}$ and a current of $3.5\ \text{A}$ was drawn. The plasma reacts to separatrix biasing similarly as in the case of argon, but the change in the confinement quality is different. The influence on the equilibrium is depicted in Fig. 7.10. In the biased phase, the floating potential is enhanced by about $40\ \text{V}$ in the whole region inside the separatrix. An increase in the shear of the poloidal $E \times B$ flow is observed only at the separatrix. For argon, separatrix biasing led to an increase of the flow shear inside the separatrix in a region of maximum density gradients (see Fig. 7.3). The shear estimated from the floating potential was found to be rather large compared to the maximum linear growth rate γ_{max} of unstable drift-modes. The layer, in which the accurate values of the shear might exceed γ_{max} could be assumed to be broadened. For hydrogen, γ_{max} is between 35 and $50\ \text{kHz}$ and Fig. 7.10 suggests that the shear stabilisation criterion (2.27) is fulfilled only at the separatrix during biasing in a layer, which is smaller than for argon.

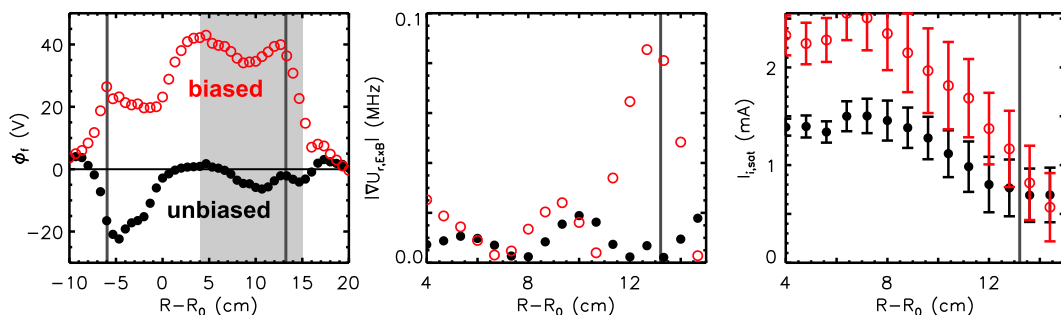


FIG. 7.10: Effect of separatrix biasing on the equilibrium of an hydrogen discharge (#3005), in the same representation as in Fig. 7.3. For the floating potential, standard deviations are comparable to the symbol size. The separatrix is indicated by vertical lines.

7.2 Ring biasing at the separatrix

This might point to a ρ_s dependence of the width of the shear layer. The profile of the ion-saturation current on the right-hand side of Fig. 7.10 shows an increase. For $R - R_0 < 12$ cm, the gradient scale length L_\perp stays constant. A decrease of L_\perp is found for $R - R_0 \geq 12$ cm in the region of increased flow shear. Furthermore, relative fluctuation levels \tilde{n}/n are magnified in this region.

As depicted in Fig. 7.11, an increase in the transport level is found, which in this case can mainly be attributed to the higher fluctuation levels. Power spectra of fluctuations in the floating potential and ion-saturation current show an increase on all scales. In both spectra, a small peak shows up at approximately

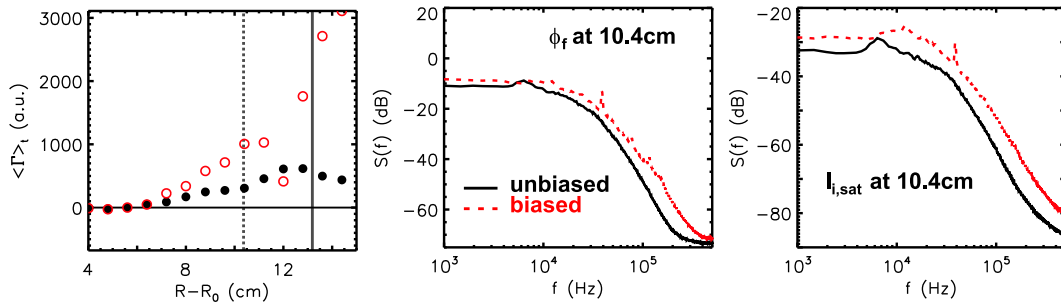


FIG. 7.11: Local turbulent transport (left) and power spectra of fluctuations in the floating potential (middle) and ion-saturation current (right) of a hydrogen discharge in the same representation as in Fig. 7.5 (argon).

40 kHz. Note that the spectral decomposition of the transport in general is more complicated and transport levels strongly depend on cross-phases and coherences. Compared to argon, the situation is different. In hydrogen, peaks do not show up as prominent as in argon. In general, cross-phases and coherences are strongly sensitive to plasma biasing. A clear systematic dependence of the turbulence characteristics in frequency space on induced shear flows was not found. However, one general trend is reflected in the average cross-phases as shown in Fig. 7.12. For $R - R_0 \geq 10.4$ cm the average cross-phase determines the radial dependence of the turbulent transport. For smaller radii, the phases are closer to $\pi/2$, but the transport is larger than in the unbiased case. According to Eq. (4.15), this points to an increased fluctuation amplitude being responsible for the increase in the transport.

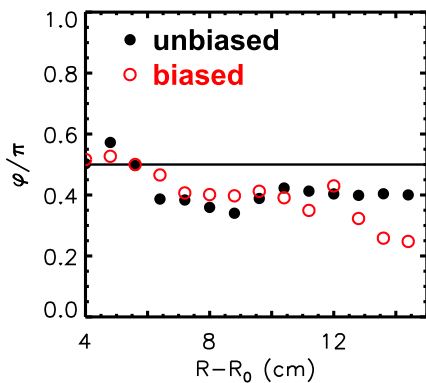


FIG. 7.12: Average cross-phase between poloidal electric field and density fluctuations (#3005). In comparison with the turbulent transport shown on the left-hand side of Fig. 7.11, the transport is governed by increased fluctuation amplitudes for $R - R_0 \leq 10.4$ cm.

7. Plasma biasing

In argon discharges, several criteria for an improved plasma confinement are fulfilled during separatrix biasing. In particular, the density gradient is steepened and fluctuation as well as transport levels are decreased. For smaller ion masses than argon – as presented here for an hydrogen discharge – separatrix biasing leads to an amplification of fluctuation and transport levels. The argon data showed an increase of $E \times B$ flow shear in the region of maximum density gradients within the confinement area (see Fig. 7.3). For hydrogen, the induction of strong $E \times B$ shear is restricted to the edge region. The difference in the radial width of $E \times B$ shear might be due to effects related to different ion Larmor radii. It might be reasonable to assume that confinement improvement would be most efficient if the shear layer is placed directly in the region, where turbulence can tap free energy as explained in Sec. 2.3, namely in the region of maximum density gradients. This is supported by the findings in argon discharges as can be seen in Fig. 7.3. For hydrogen, this is investigated in the next section.

7.3 Ring biasing inside the separatrix

Separatrix biasing has shown that an improved confinement can be achieved in argon discharges, whereas in hydrogen the situation is more complicated. In hydrogen, the induction of the shear layer is restricted to the edge region. Fluctuation and transport levels are raised, the improved confinement is obscured. In this section it will be studied whether the confinement can also be improved in hydrogen discharges and if so under which conditions. For this purpose a ring-like electrode is aligned on a flux surface inside the separatrix.

7.3.1 Comparison with separatrix biasing

With the unbiased electrode inserted, the plasma inside the confinement region is altered. For an hydrogen discharge at the same parameters as in Fig. 7.10, the effect of plasma biasing inside the separatrix is illustrated in Fig. 7.13. At a bias voltage of $U_b = 50$ and 100 V, currents of 3 and 3.5 A could be drawn. Biasing leads to a drastic raise of the floating potential inside the biased ring leading to increased radial electric fields between ring and separatrix. At a bias voltage of 50 V the profile of the $E \times B$ shear inside the separatrix is similar to that in case of separatrix biasing. A further increase of the bias voltage leads to stronger shear and to a shift of the shear maximum towards the electrode. Density gradients are steepened in both cases. The location of the maximum density gradients coincides with the region of maximum change in flow shear. With $\gamma_{\max} = 35\text{--}50$ kHz, the shear stabilisation criterion (2.27) is rather fulfilled for $U_b = 100$ V.

On the right-hand side of Fig. 7.13, the profiles of the ion-saturation current indicate a steepening of the density gradient by a factor of about 2.5 and 5

7.3 Ring biasing inside the separatrix

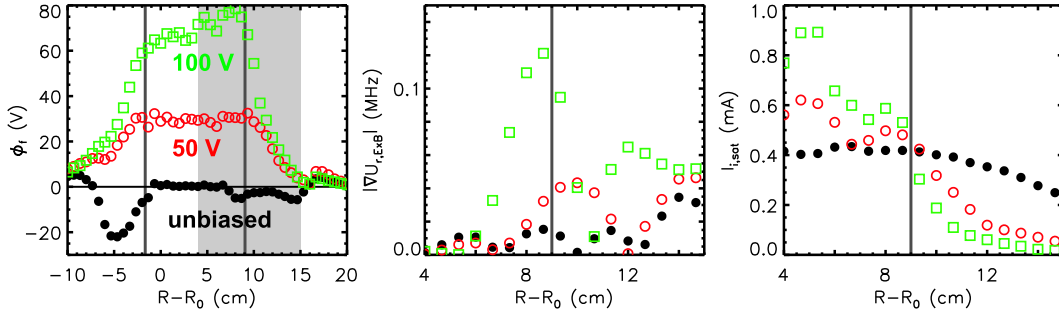


FIG. 7.13: Effect of biasing inside the separatrix on the equilibrium of an hydrogen discharge (#3026) at the same discharge parameters and in a similar representation as in Fig. 7.10. Vertical lines mark the position of the electrode.

for a bias voltage of 50 and 100 V, respectively. With $U_{\text{dia},e} \approx 500$ m/s, this would lead to maximum diamagnetic-drift velocities of 1250 and 2500 m/s in the biased cases. The radial profiles of the $E \times B$ velocity shown in Fig. 7.14 indicate that $E \times B$ flows are efficiently produced inside the confinement region. Compared to the estimates for the electron-diamagnetic drift, the maximum values for the $E \times B$ drift are larger during biasing with $U_{E \times B} \approx 1.5$ and 3.5 km/s for $U_b = 50$ and 100 V, respectively. Hence, structures are expected to drift into the opposite direction. In Sec. 7.2, it was argued that radial electric

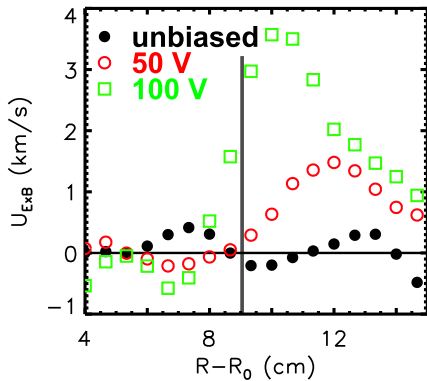


FIG. 7.14: Radial profile of the poloidal $E \times B$ velocity in the same representation as in Fig. 7.4.

fields could be underestimated by an order of magnitude in case of efficient biasing and the relation (7.1) should be used instead of a simple approximation to the results from the actual plasma potential. This will be considered in the analysis of turbulent structures in the next section.

As shown in Fig. 7.15, the effect on turbulent transport and average cross-phase at $U_b = 50$ V is similar to that in separatrix biasing. In the present case, the transport is slightly enhanced and the deviation of the average cross-phase between poloidal electric field and density fluctuations from $\varphi = \pi/2$ is increased outside the electrode. At a bias voltage of 100 V, transport is reduced and the phase is shifted to $\pi/2$. Both quantities together with the steepened density gradient indicate an improvement of plasma confinement rather for higher bias voltages. In the previous section, it was suggested that confinement improvement could be most efficient if the shear is increased in the

7. Plasma biasing

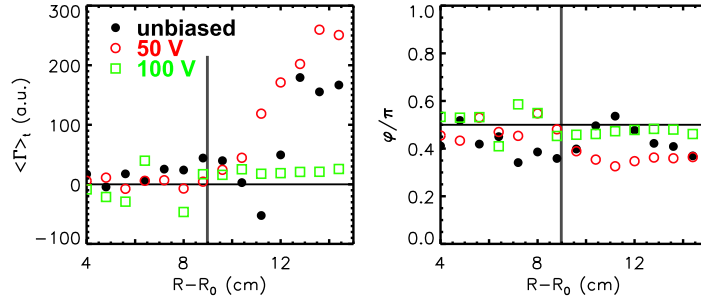


FIG. 7.15: Local turbulent transport (left) and average cross-phase (right) for different bias voltages.

region of maximum density gradients. The present results point to a correlation between induced shear and location of the maximum density gradient (see Fig. 7.13). In addition, the shear must exceed a threshold theoretically given by the stabilisation criterion (2.27) in order to improve the confinement. The profile of the flow shear in the middle of Fig. 7.13 indicates that this criterion is fulfilled for $U_b = 100$ V. It must be stressed, however, that the absolute values of the shear estimated from the floating potential should be interpreted with caution.

7.3.2 Influence on turbulent structures

In Fig. 7.16 it is shown that the influence of the ring-probe leads to opposite drifts of turbulent density structures for unbiased and biased cases at both bias voltages of $U_b = 50$ and 100 V. It must be stressed that in the present data single channels, which had data acquisition problems, have been interpolated or omitted. In the unbiased phase, structures of small spatial scales propagate in the direction of the electron-diamagnetic drift with $U_\theta \approx 800$ m/s. For a bias voltage of 50 V, the structure propagates poloidally in the opposite direction, i.e., in the direction of the poloidal $E \times B$ drift. The propagation velocity is about five times larger, i.e., $U_\theta \approx 4$ km/s. At a bias voltage of 100 V, a further increase in the propagation velocity by a factor of about three is observed. Therefore, $U_\theta \approx 12$ km/s. The poloidal drift velocities are larger than estimated previously. If the $E \times B$ velocity is assumed to be negligible in the unbiased case and the steepening of the density gradient from Fig. 7.13 is taken into account, the $E \times B$ velocities ought to be 6 and 16 km/s in the biased cases. This is roughly a factor of 4 larger than the velocities shown in Fig. 7.14 and closer to the estimates according to Eq. 7.1, which would be a factor of 2.5 higher. Hence, it is reasonable to assume that in the biased cases also the shear is a factor of 4 higher than that shown in Fig. 7.13. As in case of separatrix biasing in argon, the values of the shear would be an order of magnitude higher than γ_{\max} .

During separatrix biasing in argon discharges, the structure showed a faster decay yielding smaller correlation times (see Fig. 7.8). In hydrogen discharges,

7.3 Ring biasing inside the separatrix

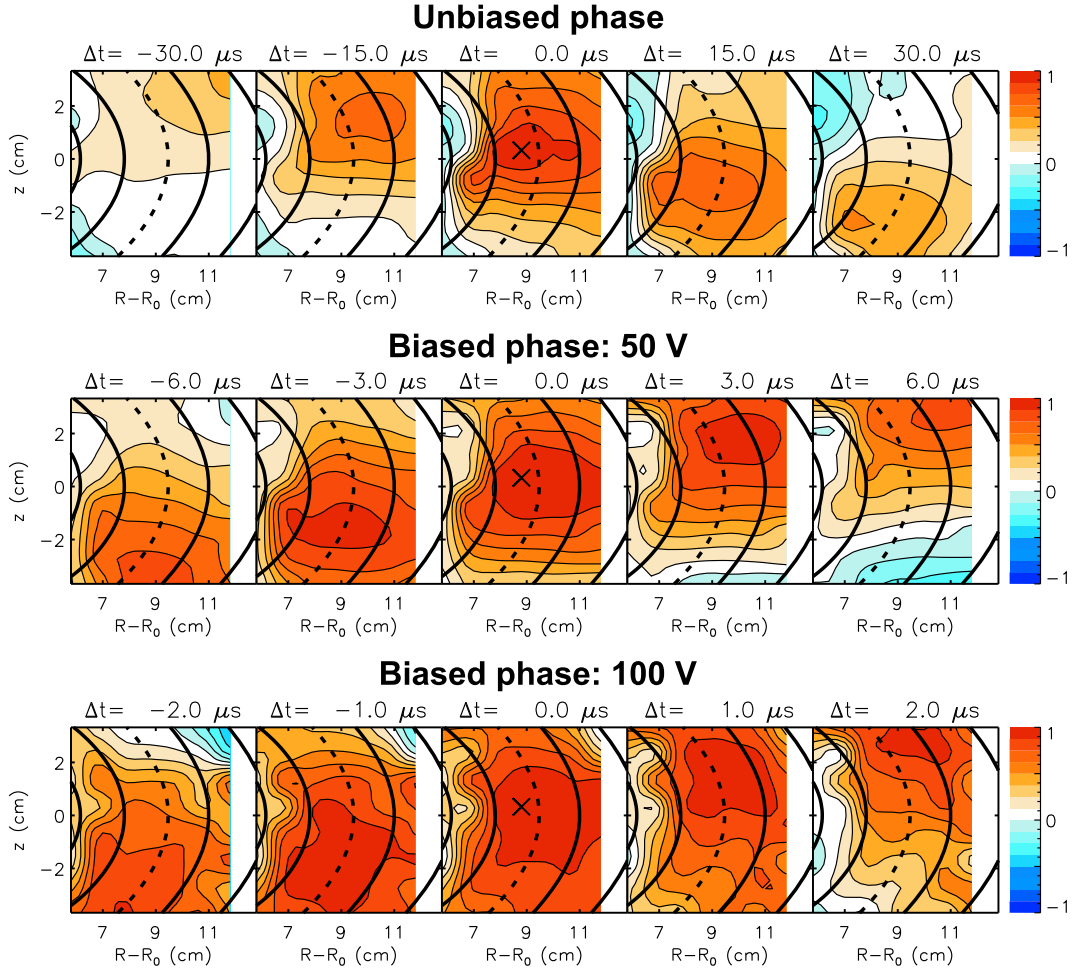


FIG. 7.16: Spatio-temporal evolution of a turbulent density structure for the unbiased (top) and the biased cases with $U_b = 50$ V (middle) and $U_b = 100$ V (bottom) (#3026). Flux surfaces are shown up to the separatrix. The electrode is depicted as dashed curve. The reference probe is marked by a cross. Note the change in time windows from 60 to $4\mu\text{s}$.

the structure shows high correlation values while passing the probe array. The shortened time windows in Fig. 7.16 might suggest that also in hydrogen the correlation times are decreased during biasing. For $U_b = 50$ V, the spatial extents at $\Delta t = 0$ appear increased. The shape of the structure, however, stays smooth. For $U_b = 100$ V, the extents are further increased and the structure appears strongly distorted as in case of separatrix biasing in argon discharges. A radial decorrelation is not observed.

For unbiased and biased cases, the auto-power spectra of fluctuations in the ion-saturation current calculated from the probe at $(i, j) = (3, 4)$ are compared on the left-hand side of Fig. 7.17. They show a similar behaviour as for separatrix biasing. In the unbiased case, the maximum power is found at about 3 kHz. In the state of increased transport levels at $U_b = 50$ V, the fluctuation amplitudes are amplified on all temporal scales. The major contribution

7. Plasma biasing

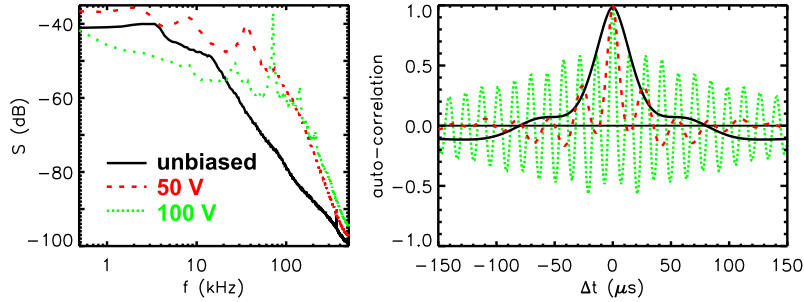


FIG. 7.17: Auto-power spectra from fluctuations in the ion-saturation current at probe $(i, j) = (3, 4)$ of the matrix (left) and auto-correlation functions (right) at the same position. The unbiased case (solid line) is compared with the biased case for $U_b = 50$ V (dashed) and $U_b = 100$ V (dotted).

appears to be due to a Doppler shift, i.e., from 30 kHz to 140 kHz, which according to Eq. 7.2 yields $U_{E \times B}^b / U_{\text{dia}} \approx 5$. This is in rather good agreement with the ratio of the propagation speeds shown in Fig. 7.16. For $f > 140$ kHz, the shifted spectrum shows a higher spectral index. For $U_b = 100$ V, fluctuations below 140 kHz are strongly damped except for a prominent mode emerging at about 70 kHz. Higher harmonics show up for $f \geq 140$ kHz. Otherwise, the shape of the spectrum is not changed in this region.

On the right-hand side of Fig. 7.17, the auto-correlation functions (ACF) measured at $(i, j) = (3, 4)$ are shown. In the unbiased case, the period of approximately $T = 300 \mu\text{s}$ is related to the frequency at which the power spectrum has its maximum. For $U_b = 50$ and 100 V, the peaks in the spectra can be identified in the ACF by periods of $T \approx 28$ and $14 \mu\text{s}$, respectively. With increasing bias voltage the ACF is squeezed, which points to a Doppler shift due to higher $E \times B$ rotation in the confinement area. For $U_b = 50$ V, the full width at the half maximum (FWHM) of the ACF is a factor of 3.5 smaller than in the unbiased phase. This width is further halved at thrice the propagation speed. From Fig. 7.16 it can be seen that the poloidal extent of the structure at a bias voltage of 50 V is about 2/3 smaller than at 100 V. Therefore, the peak at 70 kHz results from the peak at 35 kHz through the Doppler shift and the decrease in poloidal wavenumber by a factor of 2/3. From the unbiased case to $U_b = 50$ V, Fig. 7.16 shows an increase in poloidal extent by a factor of about 3/2 and in propagation speed by a factor of 5. Hence, the mode at 35 kHz originates from a mode at about 10 kHz, which is indicated in the ACF by a modulation in the unbiased case. This way, also the peak at 70 kHz can be reduced to 10 kHz. With the same method, the peak at 3 kHz in the unbiased case can be recovered in the spectrum for $U_b = 100$ V as damped and shifted to about 20 kHz.

As in the case of separatrix biasing in argon discharges, the ACF and the power-spectra indicate the damping of a large-scale quasi-coherent mode. Another mode at a higher frequency becomes dominant. The coherence of this mode increases with increasing $E \times B$ flow shear as indicated by the broadening

of the envelope of the ACF. While in argon discharges the poloidal wavenumber is increased, a decrease was found for hydrogen. In both cases, however, the poloidal mode structure is affected. For a detailed analysis, measurements with a poloidal multi-probe array are required.

7.4 Summary

Different schemes have been applied in order to test the applicability of plasma biasing in TJ-K for the investigation of the influence of $E \times B$ shear flows on turbulent transport. The objective was to investigate the reduction in radial turbulent transport associated with turbulent structures via the shear decorrelation mechanism. From a simple point of view, strong poloidal $E \times B$ shear flows reduce the radial correlation length of these structures leading to a decrease in the radial step size of diffusive random walk processes and, thus, radial particle transport.

The first challenge was to induce poloidal $E \times B$ shear flows adequately. Common biasing schemes as applied in tokamaks (see, e.g., [72]) failed in TJ-K. In the ideal case, a simple biased electrode would induce a potential perturbation on the whole flux surface. In TJ-K, the induced potential perturbation turned out to be toroidally limited to a few turns and not able of sufficiently influencing the plasma condition. This might be a consequence of relatively high collisionality or of the complex geometry of the magnetic field. In TJ-K, the confinement time is rather low, so that a local perturbation in the space charge might be lost after a few toroidal turns.

This problem can be bypassed by a ring-like electrode aligned on a certain flux surface. This way a homogeneous perturbation is achieved. A sudden drop in the line averaged density, the current drawn by the electrode and the effective heating power at a certain bias voltage indicated a transition in the plasma conditions. A back-transition happened at different bias voltages, hence a hysteresis is present. In tokamak experiments, especially the drop in the current drawn by the electrode marked the bifurcation of the plasma rotation and indicated a transition into a regime of improved confinement [19, 21]. The concomitant drop in the line averaged density observed in TJ-K seems to be opposite to the expected effect. In the present experiment, however, a possible improvement in confinement is nullified due to a sudden reduction in absorbed heating power. This could be related to the plasma production process by ECRH in an over-dense plasma. The drop in the parameters can be compensated by rematching the microwave. In the rematched state, higher electrode currents can be drawn pointing to a faster plasma rotation.

Comparative studies in argon and hydrogen discharges have been carried out. Therefore, the separatrix biasing scheme, which was reported to be rather efficient in the induction of $E \times B$ shear in the CASTOR tokamak [73], was transferred to the ring-like biasing electrode. Basic differences between both

7. Plasma biasing

gases lie in the ion Larmor radii and – according to the ρ_s scaling of correlation lengths – in the structure sizes. Large-scale structures in argon are expected to be affected more easily by flow shear than small-scale structures as in hydrogen. Although increased shear is expected near the electrode at the separatrix, in argon discharges, an increased shear was observed relatively deep inside the confinement area in the region of maximum density gradients. In hydrogen, the region of flow shear remained close to the electrode. This might point to a relation between the width of the shear layer and ρ_s . Improved confinement was indicated by reduced fluctuation and transport levels as well as steepened density gradients. In hydrogen, the induction of strong shear was restricted to the edge region near the separatrix and the fluctuation and transport levels increased. Biasing inside the separatrix places the induced shear layer closer to the density gradient, where the turbulence is driven. That way an improved confinement could be achieved also in hydrogen discharges. This suggests that not only the magnitude of the flow shear is important for improving the confinement, but also the position of the shear layer. The flow shear was measured to be an order of magnitude larger than intrinsically required for fulfilling the stabilisation criterion.

Reduced transport appeared together with cross-phases shifted to $\pi/2$ indicating a trend towards enhanced stability. In general, during biasing, distinctive modes at higher frequencies emerge in the power spectra of potential and density fluctuations and strong $E \times B$ rotation lead to a Doppler shift of the frequencies. Both effects are reflected in the auto-correlation function. The drastic broadening of its envelope at a state of improved confinement points to an increase in the coherence of quasi-coherent modes.

The influence of $E \times B$ shear flows on turbulent density structures was studied by means of an 8×8 probe array. Cross-correlation analyses were carried out in order to resolve the spatio-temporal evolution of turbulent density structures during biasing. Evidence of the radial decorrelation of these structures at the presence of strong $E \times B$ shear was not found. The structures appear distorted and rather raised in size. Biasing experiments in argon indicated a decrease of their lifetime. In hydrogen, a statement on the lifetimes was not possible, since high poloidal $E \times B$ drift velocities carried the structures out of the matrix too quickly. In terms of diffusive random walk processes, the diffusivity would be increased at an increased radial step size and reduced temporal scales, although density gradients are steepened and transport levels are decreased. The cross-phase between poloidal electric field and density fluctuations, however, indicated more stable modes on the average. This demonstrates that the cross-phase plays a key role in the reduction of turbulent transport.

The structures were observed to propagate mainly poloidally in a direction, which depends on whether the contribution of the $E \times B$ or the diamagnetic drift is dominant. Moreover, the broadening of the envelope of the auto-correlation function and the change in periodicity might indicate a change in

the poloidal mode structure rather than a radial decorrelation.

In summary, the equilibrium and the fluctuations in TJ-K were successfully modified by a biased flux-surface-aligned electrode. Pronounced $E \times B$ shear layers were induced. Improved confinement was indicated by steepened density gradients and reduced fluctuation as well as transport levels. This situation is accompanied by cross-phases, which indicate more stable modes on the average. Modes at higher frequencies featuring an increased coherence appear in the power spectra. These modes might be related to a change in the poloidal mode structure. Although the measured flow shear indicated the compliance with the shear stabilisation criterion, a radial decorrelation of turbulent structures due to $E \times B$ shear flows was not observed. In conclusion, radial turbulent transport can be reduced by induced $E \times B$ flow shear in TJ-K. This reduction did not prove to be related to a radial decorrelation of turbulent structures. It is rather a consequence of enhanced stability reflected in the average cross-phase between poloidal electric field and density fluctuations.

7. Plasma biasing

Summary and Conclusions

The structure of turbulent fluctuations and their interaction with global plasma flows have been studied on the toroidal low-temperature plasma in TJ-K. The focus was on two aspects, which both are relevant for fusion plasmas, too: the scaling of the characteristic structure size with $\rho_s = \sqrt{M_i T_e} / (eB)$ and the mechanism, how sheared plasma flows suppress turbulent transport. The first aspect is an important issue in fusion research, since a fusion reactor is operated at higher magnetic fields and, therefore, smaller ρ_s than present-day devices. Hence, an extrapolation to small ρ_s is needed for predicting the confinement quality in ITER. It has been demonstrated that the way this extrapolation is usually done can be misleading. The latter aspect addresses the fundamental question, how shear flows can suppress turbulence as it is observed in transport barriers of fusion devices.

Usually, scaling studies are carried out on global energy confinement times or deduced diffusivities. On the basis of diffusive random walk processes of particles, a turbulent diffusivity $D = L_r^2 / \tau_c$ can be constructed out of radial correlation lengths (L_r) and correlation times (τ_c) of characteristic turbulent structures. Here, the scaling has been investigated directly on the microscopic turbulence properties. These properties were gained from measurements with an 8×8 Langmuir probe array capturing the spatio-temporal evolution of propagating turbulent density structures. In five different gases from hydrogen to argon, ρ_s has been varied by a factor of 10. Structures were found with correlation lengths ranging from 2 to 8 cm and correlation times ranging from 10 to 100 μs yielding large values for D in the range 20–200 m^2/s . The correlation lengths and times increase with ion mass and ρ_s .

Different scalings of the structure size for different regions of ρ_s were found. For smaller ion masses, represented by hydrogen and deuterium, close to linear scalings of the radial correlation length L_r with ρ_s and the correlation time τ_c with a/c_s were found as it is consistent with drift-wave turbulence theory. Including larger ion masses in the scaling analysis successively lowers the scalings. This might reflect the global nature of the turbulence in discharges, where the structure sizes become comparable to the system size given by the minor plasma radius.

8. Summary and Conclusions

The prediction for the normalised diffusivity $D^* = D/(\rho_s c_s)$ to be scaling gyro-Bohm-like (i.e., $D^* \sim \rho_s$) is based on the prediction of linear scalings of L_r and τ_c with ρ_s and $1/c_s$, respectively. It was shown that, even in the case, where L_r and τ_c scale similar as predicted, the D^* scaling turns out to be very different. Hence, one should be very careful when comparing the scaling of D^* with theoretical predictions, as done in many fusion experiments.

In addition, the cross-phase should also be taken into account in the mixing length estimate, which was found to further alter the scaling. In all gases, the average cross-phase between poloidal electric field and density fluctuations is close to $\pi/2$ as it is characteristic for drift-wave turbulence¹. However, it is not constant as assumed for the estimate of the turbulent diffusivity. For small ion masses, cross-phases smaller than $\pi/2$ were found indicating radial outward transport. For neon, the cross-phase was approximately $\pi/2$. This points to the dominant mode found in neon discharges being a linear stable drift-mode. For argon, the phases were slightly larger than $\pi/2$ pointing to a stabilisation of dominant drift-modes. The cross-phase substantially modifies the diffusivity and its scaling. It reduces the value of the diffusivity ($D_\varphi = D \cos(\varphi)$) by a factor of 10. If this value is rescaled to fusion plasma parameters values for D_φ in the range 0.2–2 m²/s are found.

A further important aspect in nuclear fusion research is the influence of poloidal shear flows on turbulence. They can trigger transitions into transport barriers, which improve confinement. The improvement of the confinement is assumed to be due to a decorrelation of turbulent structures reducing L_r . A detailed knowledge of this shear decorrelation mechanism opens a path to control turbulence and, hence, to optimise the confinement quality in future fusion reactors. A threshold for turbulence being suppressed is given by the condition that the shearing rate exceeds the maximum growth rate of all unstable modes.

In this work, the effect of three kinds of sheared poloidal plasma flows on turbulence was studied: zonal flows, the natural shear layer at the separatrix and externally induced ones. Spontaneously excited shear flows were investigated on data obtained from the turbulence simulation code DALF3. The analyses showed that spontaneously excited zonal flows (ZF) occur in two types: the original long lived ZF and a flow oscillating at the geodesic-acoustic-mode (GAM) frequency. It was shown, that also this time-dependent oscillating flow, which was dominant in the simulated data, can contribute to the reduction of turbulent transport.

Cross-bispectral analyses measure the Reynolds stress (RS) drive of ZFs in terms of a non-linear coupling between small-scale drift-waves and the large-scale ZF. Different bispectral quantities – the cross-bicoherence as a measure of the amount of coherent three-mode coupling and simplified versions, which

¹Note that here the phase between \tilde{E}_θ and \tilde{n} is discussed, while other publications refer to that between $\tilde{\phi}$ and \tilde{n} , which is smaller by $\pi/2$.

are experimentally more accessible – were compared and studied. The simplified versions did not turn out to be useful for studying the coupling. A reasonable correlation between drive and ZF or GAM was detected in the cross-bicoherence evaluated in frequency space. The RS did not appear as a clear precursor of ZF or GAM amplitudes, but rather simultaneously in the region of radial ZF/GAM gradients, which points rather to the decay than the driving process. GAMs should appear together with density perturbations induced by the poloidal asymmetry in $E \times B$ flows due to the radial magnetic field gradient. A signature of the existence of ZFs in toroidal experiments would be the appearance of GAMs with the simple frequency-scaling property $\omega_{\text{GAM}} \sim c_s/R_0$. However, this signature was not observed in experiments on TJ-K. The lack is attributed to the magnetic configuration, which is more complex in TJ-K than in tokamaks as used in DALF3 simulations.

A second kind of flow shear is located at the separatrix. In TJ-K, the potential in the core is higher than at the edge. This might be due to direct losses of electrons leading to positive electric fields inside the confinement region. The potential is minimum at the last closed flux surface (separatrix). Outside the separatrix the potential increases again due to parallel losses of electrons to the wall. The change in the direction of the radial electric field forms a layer of sheared $E \times B$ flow at the separatrix. Although the measured values of the shear in this region fulfilled the criterion for stabilising turbulence, a local effect on turbulent structures was not found.

The third kind of shear is externally induced by plasma biasing. Different biasing schemes were tested to create sufficiently strong shear flows to have an impact on turbulent structures and radial transport. A clear effect was achieved with ring-like electrodes aligned on a flux surface. The $E \times B$ shear layers could be induced in different radial regions by positioning the electrode on different flux surfaces. The plasma conditions and the fluctuations could strongly be influenced. Transitions into improved confinement were obtained, which was indicated by steepened density gradients and reduced fluctuation and transport levels. The average cross-phase between poloidal electric field and density fluctuations point to an enhanced stability of drift-waves. Improved confinement was achieved when the shear was increased inside the confinement region at high density gradients, where turbulence is driven. In the biased phase, prominent peaks at higher frequencies emerge in the power spectra of potential and density fluctuations. In the state of improved confinement these modes drastically gain in coherence pointing to a change in the poloidal mode structure.

The influence of shear flows on turbulent structures was analysed. The direction of the poloidal propagation of these structures changed from the electron-diamagnetic to the $E \times B$ -drift direction when strong radial electric fields were induced inside the confinement area. It was shown that in the presence of $E \times B$ shear flows the structures are generally distorted, but a decrease of the radial correlation length was not observed. Transport reduction can be

8. Summary and Conclusions

traced to enhanced stability reflected in the cross-phase and also shortened lifetimes.

The results obtained in the present work show that diffusivities based on simple mixing length estimates have to be interpreted with caution. For small ion masses, the scaling of microscopic turbulence properties is consistent with the prediction for drift-wave turbulence. Biasing in TJ-K leads to strong shear flows, which have an impact on turbulence and transport. That way confinement can be improved. The radial decorrelation of turbulent structures could not be confirmed. In contrast, the cross-phase is found to play the key role in the reduction of turbulent transport due to sheared plasma flows.

In the future, poloidal multi-probe arrays should be used to investigate the influence of induced flow shear on the mode structure. In order to simultaneously cover the radial dynamics, a setup of multi-probe arrays covering different flux surfaces at the same toroidal position is suggested.

References

- [1] H. Tasso, B. J. Green, and H. P. Zehrfeld, *Phys. Fluids* **12**, 2444 (1969).
- [2] U. Frisch, *Turbulence* (Cambridge University Press, Cambridge, 1995).
- [3] A. Kolmogorov, *Dokl. Akad. Nauk. SSSR* **32**, 16 (1941), reprinted in *Proc. R. Soc. Lond. A* 434 (1991).
- [4] S. J. Zweben and R. W. Gould, *Nucl. Fusion* **25**, 171 (1985).
- [5] O. Grulke, F. Greiner, T. Klinger, and A. Piel, *Plasma Phys. Controll. Fusion* **43**, 525 (2001).
- [6] J. Bleuel *et al.*, *New J. Phys.* **4**, 38.1 (2002).
- [7] B. B. Kadomtsev, *Sov. J. Plasma Phys.* **1**, 295 (1975).
- [8] J. W. Connor and J. B. Taylor, *Nucl. Fusion* **17**, 1047 (1977).
- [9] R. E. Waltz, J. C. DeBoo, and M. N. Rosenbluth, *Phys. Rev. Lett.* **65**, 2390 (1990).
- [10] U. Stroth *et al.*, *Phys. Rev. Lett.* **70**, 936 (1993).
- [11] C. C. Petty *et al.*, *Phys. Plasmas* **2**, 2342 (1995).
- [12] F. Wagner *et al.*, *Phys. Rev. Lett.* **49**, 1408 (1982).
- [13] F. Wagner *et al.*, *Phys. Rev. Lett.* **53**, 1453 (1984).
- [14] H. Biglari, P. H. Diamond, and P. W. Terry, *Phys. Fluids, B* **2**, 1 (1990).
- [15] P. H. Diamond *et al.*, *Fusion Energy (Proc. 17th Int. Conf., Yokohama, Japan, 1998)* (IAEA, Vienna, 1998), No. TH3/1.
- [16] P. H. Diamond and Y. B. Kim, *Phys. Fluids, B* **3**, 1626 (1991).
- [17] P. H. Diamond *et al.*, *Phys. Rev. Lett.* **84**, 4842 (2000).
- [18] G. R. Tynan, R. A. Moyer, M. J. Burin, and C. Holland, *Phys. Plasmas* **8**, 2691 (2001).

References

- [19] R. J. Taylor *et al.*, Phys. Rev. Lett. **63**, 2365 (1989).
- [20] G. R. Tynan *et al.*, Phys. Rev. Lett. **68**, 3032 (1992).
- [21] R. R. Weynants, S. Jachmich, and G. Van Oost, Plasma Phys. Controll. Fusion **40**, 635 (1998).
- [22] R. R. Weynants, *J. Plasma Fusion Res. SERIES (Proc. 11th Toki Conf. on Pl. Phys. Contr. Nucl. Fus., Toki-city, Japan, 2000)* (The Japan Society of Plasma Science and Nuclear Fusion Research, Nagoya, 2001), Vol. 4, pp. 3–12.
- [23] S. Jachmich, M. Van Schnoor, and R. Weynants, *Proc. of the 29th EPS Conference on Plasma Phys. and Contr. Fusion, Montreux* (The European Physical Society, Amsterdam, 2002), Vol. 26B, pp. 1–4.
- [24] S. Niedner, B. D. Scott, and U. Stroth, Plasma Phys. Controll. Fusion **44**, 397 (2002).
- [25] C. Lechte, *Microscopic Structure of Plasma Turbulence in the Torsatron TJ-K*, Ph.D. thesis (Christian-Albrechts-Universität, Kiel, 2003).
- [26] B. Scott, Plasma Phys. Controll. Fusion **39**, 1635 (1997).
- [27] J. Wesson, *Tokamaks* (Clarendon Press, Oxford, 1987).
- [28] C. Gourdon, *Programme optimise de calculs numerique dans les configurations magnetique toroidales* (CEN, Fontenay aux Roses, 1970).
- [29] L. Spitzer, in *Interscience tracts on physics and astronomy*, edited by R. E. Marshak (Interscience Publishers, Inc., New York, 1956).
- [30] K. Rahbarnia, *Neoklassischer Transport und radiale elektrische Felder in einem Niedertemperaturplasma*, Master's thesis (Christian-Albrechts-Universität, Kiel, 2003).
- [31] U. Stroth, *Einführung in die Plasmaphysik (Vorlesungsskript)* (Christian-Albrechts-Universität, Kiel, 2002).
- [32] C. Lechte, S. Niedner, and U. Stroth, New J. Phys. **4**, 34.1 (2002).
- [33] S. Niedner, *Numerical Studies of Plasma Turbulence for Comparison with Measurements at TJ-K*, Ph.D. thesis (Christian-Albrechts-Universität, Kiel, 2002).
- [34] N. Mahdizadeh *et al.*, Phys. Plasmas **11**, 3932 (2004).
- [35] S. I. Braginskii, in *Reviews of Plasma Physics*, edited by M. A. Leontovich (Consultants Bureau, New York, 1965), p. 205.
- [36] B. Scott, Phys. Plasmas **5**, 2334 (1998).

-
- [37] B. Scott, Phys. Plasmas **8**, 447 (2001).
- [38] R. H. Kraichnan, Phys. Fluids **10**, 1417 (1967).
- [39] D. L. Jassby, Phys. Fluids **15**, 1590 (1972).
- [40] A. J. Wootton *et al.*, Phys. Fluids, B **2**, 2879 (1990).
- [41] U. Stroth, Plasma Phys. Controll. Fusion **40**, 9 (1998).
- [42] U. Stroth *et al.*, Nucl. Fusion **36**, 1063 (1996).
- [43] C. C. Petty *et al.*, Phys. Rev. Lett. **74**, 1763 (1995).
- [44] J. W. Connor and H. R. Wilson, Plasma Phys. Controll. Fusion **42**, R1 (2000).
- [45] B. A. Carreras *et al.*, Phys. Plasmas **3**, 2664 (1996).
- [46] G. R. McKee *et al.*, Nucl. Fusion **41**, 1235 (2001).
- [47] S.-I. Itoh and K. Itoh, Phys. Rev. Lett. **60**, 2276 (1988).
- [48] K. C. Shaing and E. C. Crume, Phys. Rev. Lett. **63**, 2369 (1989).
- [49] K. Itoh, Plasma Phys. Controll. Fusion **36**, A307 (1994).
- [50] K. H. Burrell, Phys. Plasmas **4**, 1499 (1997).
- [51] P. W. Terry, Rev. Mod. Phys. **72**, 109 (2000).
- [52] A. B. Hassam, Comments Plasma Phys. Controll. Fusion **14**, 275 (1991).
- [53] T. S. Hahm, Phys. Plasmas **4**, 4074 (1997).
- [54] A. Kendl and H. Wobig, Phys. Plasmas **6**, 4714 (1999).
- [55] T. S. Hahm *et al.*, Phys. Plasmas **6**, 922 (1999).
- [56] A. S. Ware, P. W. Terry, P. H. Diamond, and B. A. Carreras, Plasma Phys. Controll. Fusion **38**, 1343 (1996).
- [57] P. W. Terry, D. E. Newman, and A. S. Ware, Phys. Rev. Lett. **87**, 185001 (2001).
- [58] J. A. Boedo *et al.*, Nucl. Fusion **42**, 117 (2002).
- [59] C. F. Figarella *et al.*, Phys. Rev. Lett. **90**, 015002 (2003).
- [60] P. H. Diamond, Y. M. Liang, B. A. Carreras, and P. W. Terry, Phys. Rev. Lett. **72**, 2565 (1994).
- [61] A. Hasegawa and M. Wakatani, Phys. Rev. Lett. **59**, 1581 (1987).
-

References

- [62] R. A. Moyer, G. R. Tynan, C. Holland, and M. J. Burin, *Phys. Rev. Lett.* **87**, 135001(4) (2001).
- [63] A. Hasegawa and M. Wakatani, *Phys. Rev. Lett.* **50**, 682 (1983).
- [64] K. Hallatschek and D. Biskamp, *Phys. Rev. Lett.* **86**, 1223 (2001).
- [65] T. S. Hahm *et al.*, *Plasma Phys. Controll. Fusion* **42**, A205 (2000).
- [66] G. R. McKee *et al.*, *Phys. Plasmas* **10**, 1712 (2003).
- [67] N. Winsor, J. L. Johnson, and J. M. Dawson, *Phys. Fluids* **11**, 2448 (1968).
- [68] B. Scott, *Phys. Lett. A* **320**, 53 (2003).
- [69] R. R. Weynants *et al.*, *17th EPS Conference on Controlled Fusion and Plasma Heating, Amsterdam. Europhysics Conference Abstracts* (EPS, Amsterdam, 1990), Vol. 14B, Part I, pp. 287 – 290.
- [70] K. Ida, *Plasma Phys. Controll. Fusion* **40**, 1429 (1998).
- [71] C. P. Ritz, H. Lin, T. L. Rhodes, and A. J. Wootton, *Phys. Rev. Lett.* **65**, 2543 (1990).
- [72] G. Van Oost *et al.*, *Plasma Phys. Controll. Fusion* **45**, 621 (2003).
- [73] G. Van Oost *et al.*, *J. Plasma Fusion Res. SERIES (Proc. 11th Toki Conf. on Pl. Phys. Contr. Nucl. Fus., Toki-city, Japan, 2000)* (The Japan Society of Plasma Science and Nuclear Fusion Research, Nagoya, 2001), Vol. 4, pp. 29–35.
- [74] E. Ascasibar *et al.*, *Plasma Physics and Controlled Fusion Research (Proc. 16th Int. Conf., Montreal, 1996)* (IAEA, Vienna, 1996), p. 183.
- [75] N. Krause *et al.*, *Rev. Sci. Instrum.* **73**, 3474 (2002).
- [76] R. Westphal, *Vermessung der magnetische Flussflächen in TJ-K*, Master's thesis (Christian-Albrechts-Universität, Kiel, 2001).
- [77] N. Krause, *Untersuchung von Helikonwellen zur Plasmaheizung im Torsatron TJ-K*, Ph.D. thesis (Christian-Albrechts-Universität, Kiel, 2003).
- [78] T. H. Stix, *Waves in Plasmas* (American Institute of Physics, New York, 1992).
- [79] R. A. Cairns, in *Plasma Physics: An Introductory Course*, edited by R. Dendy (Cambridge University Press, Cambridge, 1993), pp. 391 – 410.
- [80] M. Michel, *Elektronenzyklotronresonanzheizung am Torsatron TJ-K*, Master's thesis (Christian-Albrechts-Universität, Kiel, 2003).

- [81] H. P. Laqua *et al.*, Phys. Rev. Lett. **18**, 3467 (1997).
- [82] V. Senger, *Spektroskopische Bestimmung der Ionentemperatur im TJ-K*, Master's thesis (Christian-Albrechts-Universität, Kiel, 2003).
- [83] J. Stöber, *Aufbau eines Mikrowellen-Interferometers für das Torsatron TJ-K*, Master's thesis (Christian-Albrechts-Universität, Kiel, 2001).
- [84] F. F. Chen, in *Plasma Diagnostic Techniques*, edited by R. H. Huddlestone and S. L. Leonard (Academic Press, New York, 1965), pp. 113–200.
- [85] I. H. Hutchinson, *Principles of Plasma Diagnostics* (Cambridge University Press, Cambridge, 2002).
- [86] R. R. Arslanbekov, N. A. Khromov, and A. A. Kudryavtsev, Plasma Sources Sci. Technol. **3**, 528 (1994).
- [87] V. I. Demidov, S. V. Ratynskaia, R. J. Armstrong, and K. Rypdal, Phys. Plasmas **6**, 350 (1999).
- [88] V. I. Demidov, S. V. Ratynskaia, and K. Rypdal, Rev. Sci. Instrum. **73**, 3409 (2002).
- [89] N. Mahdizadeh *et al.*, Plasma Phys. Controll. Fusion **47**, 569 (2005).
- [90] G. M. Jenkins and D. G. Watts, *Spectral analysis and its applications* (Holden-Day, San Francisco, 1968).
- [91] H. L. Pécseli, *Fluctuations in Physical Systems* (Cambridge University Press, Cambridge, 2000).
- [92] M. J. Hinich and C. S. Clay, Rev. Geophysics **6**, 347 (1968).
- [93] D. E. Smith, E. J. Powers, and G. S. Caldwell, IEEE Trans. Plasma Sci. **PS-2**, 261 (1974).
- [94] W. H. Press, B. P. Flannery, S. A. Teukolsky, and W. T. Vetterling, *Numerical Recipes* (Cambridge University Press, Cambridge, 1992).
- [95] Y. C. Kim and E. J. Powers, Phys. Fluids **21**, 1452 (1978).
- [96] Y. C. Kim and E. J. Powers, IEEE Trans. Plasma Sci. **PS-7**, 120 (1979).
- [97] M. Ramisch, *Bispektralanalyse turbulenter Fluktuationen am Experiment TEDDI*, Master's thesis (Christian-Albrechts-Universität, Kiel, 2001).
- [98] H. Johnsen, H. L. Pécseli, and J. Trulsen, Phys. Fluids **30**, 2239 (1987).
- [99] A. V. Filippas *et al.*, Phys. Plasmas **2**, 839 (1995).

References

- [100] O. Grulke, *Investigation of large-scale spatiotemporal fluctuation structures in magnetized plasmas*, Ph.D. thesis (Christian-Albrechts-Universität, Kiel, 2001).
- [101] M. Ramisch *et al.*, *Proc. 12th Int. Congress on Plasma Physics, Nice (France), October 2004* (ICPP, Nice, 2004), No. 00001832, pp. 1–8.
- [102] M. Ramisch *et al.*, *Phys. Plasmas* **12**, 1 (2005), in print.
- [103] U. Stroth *et al.*, *Phys. Plasmas* **11**, 2558 (2004).
- [104] K. W. Gentle, O. Gehre, and K. Krieger, *Nucl. Fusion* **32**, 217 (1992).
- [105] J. P. T. Koponen *et al.*, *Nucl. Fusion* **40**, 365 (2000).
- [106] M. Ramisch, U. Stroth, S. Niedner, and B. Scott, *New J. Phys.* **5**, 12.1 (2003).
- [107] H. Niedermeyer *et al.*, *Proc. of the 18th EPS Conference on Plasma Phys. and Contr. Fusion, Berlin* (The European Physical Society, Berlin, 1991), Vol. 15 C, Part I, pp. 301–304.
- [108] M. Ramisch *et al.*, *Proc. 14th Int. Stellarator Workshop, Greifswald (Germany), September 2003* (IPP, Greifswald, 2003), No. 19, pp. 1–5.
- [109] B. A. Carreras *et al.*, *Phys. Plasmas* **6**, 4615 (1999).

Acknowledgement

Many people have contributed to the completion of this work. In particular, I thank Ulrich Stroth, who gave me the opportunity to work in his research group in the challenging field of plasma turbulence. He supported me with many fruitful discussions and his intense engagement for all means needed in the group. This work would not have been possible without this promotion.

I thank Franko Greiner for his support in physical and technical questions, for the things, I have learned from him during the diploma thesis, and last but not least, for the ability of entertaining and motivating all of us many times. I'm grateful to Volker Rohwer and Michael Poser for the development and the maintenance of technical equipment. Special thanks goes to my fellows Navid Mahdi-Zadeh and Kian Rahbarnia for their technical and amicable company. I also thank all other students for the assistance and the fun (not only) in the laboratory. I would like to stress that the people in the workshop are doing excellent work.

Bruce Scott provided me with helpful details on his great code DALF3 and the underlying physics. His support contributed greatly to this work. Carsten Lechte, Nils Krause and Sven Niedner introduced me into the experiment and answered patiently my questions. I thank Thomas Klinger for providing us with the 64 channel transient recorder. The TJ-K device is provided by CIEMAT, Madrid. Financial support by Max-Planck-Institut für Plasmaphysik, Garching is gratefully acknowledged.

This work is dedicated to my mother Ulla Ramisch and my deceased grandmother Marianne Köpke.

Curriculum Vitae

Personal data

name	Mirko Ramisch
date and place of birth	2.1.1975, Neustadt/Holstein, Germany
family status	unmarried
nationality	german

School education and civil service

1982–1986	elementary school: Rudolf-Tonner-Grundschule, Neumünster
1986–1995	secondary school: Immanuel-Kant-Gymnasium, Neumünster
May 1995	final exam (Abitur) with main courses mathematics and physics
1995–1996	civil service at Haus der Jugend, Neumünster

Scientific education

Sep 1996–Jan 2002	study of physics at Christian-Albrechts-Universität, Kiel
May 1998	intermediate examination with subsidiary subjects mathematics and information technology
Dec 2000–Dec 2001	preparation of the diploma thesis entitled “Bispectral Analysis of Turbulent Fluctuations in the Experiment TEDDI” in the group of Prof. Dr. A. Piel
Jan 2002	diploma in physics
since jan 2002	Ph. D. graduation with subject “Scaling and Manipulation of Turbulent Structures in the Torsatron TJ-K” at the university of Kiel in the group of Prof. Dr. U. Stroth

Eidesstattliche Erklärung

Hiermit erkläre ich an Eides statt, dass die vorliegende Dissertation – abgesehen von der Beratung durch meine wissenschaftlichen Lehrer und der Verwendung der angegebenen Hilfsmittel – nach Inhalt und Form meine eigene ist. Sie hat weder ganz noch zum Teil an einer anderen Stelle im Rahmen eines Prüfungsverfahrens vorgelegen.

Kiel, im März 2005

(Mirko Ramisch)